Computational Modelling Of Wind Turbine Wakes Using an Actuator Disc Coupled With Reynolds Averaged Navier-Stokes Models

A Thesis Submitted to the
College of Graduate and Postdoctoral Studies
In Partial Fulfillment of the Requirements
For the Degree of Master of Science
In the Department of Mechanical Engineering
University of Saskatchewan
Saskatoon

By

Ahmad Beqai

PERMISSION TO USE

In presenting this thesis in partial fulfillment of the requirements for a Postgraduate degree from the University of Saskatchewan, I agree that the Libraries of this University may make it freely available for inspection. I further agree that permission for copying of this thesis in any manner, in whole or in part, for scholarly purposes may be granted by the professor who supervised my thesis work or, in their absence, by the Head of the Department or the Dean of the College in which my thesis work was done. It is understood that any copying or publication or use of this thesis or parts thereof for financial gain shall not be allowed without my written permission. It is also understood that due recognition shall be given to me and to the University of Saskatchewan in any scholarly use which may be made of any material in my thesis.

DISCLAIMER

The use of ANSYS/FLUENT was exclusively made to meet the thesis requirements for the degree of Master of Science at the University of Saskatchewan. Reference in this thesis to any specific commercial products, process, or service by trade name, trademark, manufacturer, or otherwise, does not constitute or imply its endorsement, recommendation, or favoring by the University of Saskatchewan. The views and opinions of the author expressed herein do not state or reflect those of the University of Saskatchewan, and shall not be used for advertising or product endorsement purposes.

Requests for permission to copy or to make other uses of materials in this thesis/dissertation in whole or part should be addressed to:

Head of the Mechanical Engineering Department
57 Campus Drive
University of Saskatchewan
Saskatoon, Saskatchewan S7N 5A9 Canada

OR

Dean
College of Graduate and Postdoctoral Studies
University of Saskatchewan
116 Thorvaldson Building, 110 Science Place
Saskatoon, Saskatchewan S7N 5C9 Canada

ABSTRACT

Wind energy is one of the fastest growing sources of renewable energy. Because of the increasing growth of the wind energy sector, advanced computational modelling of wind turbine aerodynamics and wake interactions is required. Experiments on wind turbines can be costly and sometimes impractical. Often, a computational model can be an easier and less expensive solution. Computational fluid dynamics (CFD) uses numerical methods to solve complex flow models. For wind turbine applications, several models have been implemented in CFD. The actuator disc model (ADM) is considered the simplest model. It treats the rotor as an actuator disc with a small thickness. Other computational models are the actuator line model (ALM) and a fully resolved turbine geometry.

The main objectives of this thesis are to use CFD to study the wake of a wind turbine and the interaction between two turbines in tandem. This research uses the ADM coupled with the RANS equations and explores a series of turbulence models. The first study covers the wake analysis of a standalone wind turbine, where the $k - \omega$ SST with the corrections of Cao et al. (2018) is shown to be the best model. The second study covers the wake interaction between two in-line turbines. Finally, a study using neutral atmospheric boundary conditions was also performed.

The actuator disc Reynolds-Averaged Navier-Stokes (AD/RANS) method was not able to fully capture the wake profile downstream of a rotor, especially in the region nearest to the rotor. The model did not match the spread rate and decay of the experimental data. The model was able to reproduce the disc edge effects to some extent, but not the hub effects. The AD/RANS model results begin to agree better with the experimental data in the region farther downstream of the rotor.

All simulations in this thesis work were performed using four parallel processors, in contrast to the large supercomputer simulations reported in the literature. This was realized by assumptions that were meant to maintain the essential physics while reducing the problem’s complexity.

The AD/RANS study demonstrates the potential of simplified models for exploring wind farm simulations, in particular turbine wake interaction.

ACKNOWLEDGMENTS

Thank you to my supervisor, Prof. Donald Bergstrom, for providing guidance and feedback throughout this research.

Thanks also to my family: my mother Dr. Hanan Ghneim, my brother Mohamad Beqai, and my sisters Wafaa and Fatmeh Beqai.

Finally a special thanks to my father Dr. Tawfic Beqai! You are missed everyday.

TABLE OF CONTENTS

PERMISSION TO USE……………………………………………………………………………i
ABSTRACT……………………………………………………………………………………ii
ACKNOWLEDGEMENTS………………………………………………………………………iii
TABLE OF CONTENTS………………………………………………………………………iv
LIST OF TABLES……………………………………………………………………………vi
LIST OF FIGURES……………………………………………………………………………vii
NOMENCLATURE……………………………………………………………………………x
1. INTRODUCTION……………………………………………………………………………1
1.1 Background……………………………………………………………………………2
1.1.1 History of Wind Turbines…………………………………………………………2
1.1.2 Types of Wind Turbines……………………………………………………………3
1.1.3 Rotor Design………………………………………………………………………3
1.1.4 Aerodynamic Control………………………………………………………………4
1.1.5 Environemental Impact and Noise…………………………………………………5
1.2 Objectives……………………………………………………………………………5
1.3 Thesis Organization…………………………………………………………………7
2. LITERATURE REVIEW……………………………………………………………………8
2.1 1D-Momentum Theory………………………………………………………………8
2.2 Blade Element Momentum……………………………………………………………13
2.2.1 Theory………………………………………………………………………………13
2.2.2 Prandtl's Tip Loss Correction Factor ………………………………………………18
2.2.3 Glauert Correction for High Values of *a*……………………………………………19
2.3 Numerical Models……………………………………………………………………22
3. PARAMETRIC STUDY……………………………………………………………………31
3.1 Theory…………………………………………………………………………………31
3.2 Turbulence Closure Models……………………………………………………………35
3.2.1 Standard k-ε Model…………………………………………………………………35
3.2.2 k-ε RNG Model………………………………………………………………………36
3.2.3 El Kasmi and Masson (2008) ………………………………………………………37
3.2.4 k-ω Model……………………………………………………………………………38
3.2.5 k-ω SST and Cao Et Al. (2018) Observations………………………………………39
3.3 Model Description……………………………………………………………………41
3.4 Results…………………………………………………………………………………43
3.4.1 Wake Similarity ……………………………………………………………………46
3.4.2 Constant Inlet ………………………………………………………………………48
3.4.2.1 Standalone Wind Turbine …………………………………………………48
3.4.2.2 Two Wind Turbines in Tandem ……………………………………………57
3.4.3 Atmospheric Boundary Layer ………………………………………………………65
4. CONCLUSION………………………………………………………………………………69
4.1 Summary………………………………………………………………………………69

4.2 Key Results……………………..………….…………………………..…..…….70
4.3 Suggestions for Future Work ……………………………………..…..….…….70
REFERENCES……………………………………………………………………………72
APPENDIX A……………………………………………………………………..…….78
APPENDIX B……………………………………………………………………..…….81

LIST OF TABLES

Table 3.1. Summary of turbulence closure models... ……41

Table 3.2. Summary of experiments .... ……42

Table A.1. Grid independence study (2D)... …....79

Table A.2. Grid independence study (3D)... …....80

LIST OF FIGURES

Figure 1.1. Photograph of the wake expansion of Horns Rev wind farm (© Vattenfall, Horns Rev 1 owned by Vattenfall. Photographer Christian Steiness) (Emeis, 2010)……………………..……..6

Figure 2.1. Illustration of the 1D momentum theory (Hansen, 2008) …………………………....9

Figure 2.2. Circular CV around the flow field(Hansen, 2008) ……..……………………..………..10

Figure 2.3. The power and thrust coefficients as function of the axial induction factor………...13

Figure 2.4. Annular elements of the BEM (Hansen, 2008) ……….…………………………....14

Figure 2.5. Velocities at the rotor plane (Hansen, 2008) ………………………………………..15

Figure 2.6. The loads on a blade (Hansen, 2008) ……………………………………...………..16

Figure 2.7. BEM solution algorithm……………………………………………………………..21

Figure 2.8. Stream wise velocity profiles (m/s): wind tunnel measurements (◦), ADM-NR (dashed line), ADM-R (solid line), ALM (black dots) (Porté-Agel, et al., 2011)…….……..…..25

Figure 2.9. Schematic of (A) aligned layout, (B) laterally staggered layout, and (C) vertically staggered layout wind farms (Wu et al., 2020)…………………………………………………..27

Figure 2.10. Profiles of incoming atmospheric boundary layer (ABL) flows developed over flat surfaces with roughness lengths of 0.5, 0.1, 0.01, and 0.0001 m: (A) mean streamwise velocity u $(\mathrm{m/s})$, (B) normalised velocity versus vertical height in log scale, (C) overall turbulence stage, and (D) vertical momentum flux $\langle u'w' \rangle(\mathrm{m}^2/s^2)$(Wu et al., 2020)……………………....……..28

Figure 3.1. Computational domain ……………………………………….……………..44

Figure 3.2 Velocity vectors and streamlines for flow over AD ……………………..………..45

Figure 3.3. Velocity deficit of self-similar wake profiles ……………..………………………..47

Figure 3.4. Half-width of self-similar wake profiles ……………………..………………..…..47

Figure 3.5. Turbulence kinetic energy of self-similar wake profiles ………..…………………..48

Figure 3.6. Nibe experiment: Wake velocity profile for $V_o = 11.52\ ^{\mathrm{m}}/_{\mathrm{s}}$, $C_T = 0.67$ and $TI =$ 10.5% at: $x/D = 2.5$, $x/D = 6$, $x/D = 7.5$……………………...……………..………………..49

Figure 3.7. Nibe experiment: Wake velocity profile for $V_o = 9.56\ ^{\mathrm{m}}/_{\mathrm{s}}$, $C_T = 0.77$ and $TI =$ 11% at: $x/D = 2.5$, $x/D = 6$, $x/D = 7.5$…………………………………………….………..50

Figure 3.8. Nibe experiment: Wake velocity profile for $V_o = 8.5\ ^{\mathrm{m}}/_{\mathrm{s}}$, $C_T = 0.82$ and $IT = 11\%$ at: $x/D = 2.5$, $x/D = 6$, $x/D = 7.5$………...……………………………………...……..50

Figure 3.9. Nibe experiment: Decay of wake axial turbulence intensity decay for $V_o =$ $8.5\ ^{\mathrm{m}}/_{\mathrm{s}}$, $C_T = 0.82$ and $IT = 11\%$……………...……………………………………………..52

Figure 3.10 Nibe experiment: Wake distribution of turbulence intensity at $x = 2.5D$ for $V_o =$ $8.5\ ^{\mathrm{m}}/_{\mathrm{s}}$, $C_T = 0.82$ and $IT = 11\%$…………………………………………………...…..52

Figure 3.11. Danwin experiment: Wake velocity profile for several downstream locations for $V_o = 8\ ^{\mathrm{m}}/_{\mathrm{s}}$, $C_T = 0.82$ and $IT = 7\%$ at: $x/D = 1$, $x/D = 4.15$, $x/D = 9.4$……………..53

Figure 3.12. Sexbierum experiment: Wake velocity profile for $V_o = 8.5\ ^{\mathrm{m}}/_{\mathrm{s}}$, $C_T = 0.75$ and $IT = 10\%$ at: $x/D = 2.5$, $x/D = 5.5$, $x/D = 8$…………………………………....………..54

Figure 3.13. Sexbierum experiment: Wake turbulence intensity at $x = 2.5D$ for $V_o = 8.5\ ^{\mathrm{m}}/_{\mathrm{s}}$, $C_T = 0.75$ and $TI = 10\%$………………………………………………………………..55

Figure 3.14. Sexbierum experiment: Wake turbulence intensity at $x = 5.5D$ for $V_o = 8.5\ ^{\mathrm{m}}/_{\mathrm{s}}$, $C_T = 0.75$ and $TI = 10\%$……………………………………………………………….....56

Figure 3.15. Sexbierum experiment: Wake turbulence intensity at $x = 8D$ for $V_o = 8.5\ ^{\mathrm{m}}/_{\mathrm{s}}$, $C_T = 0.75$ and $TI = 10\%$………………………….………….………….………….……...…..56

Figure 3.16. Contour of the decay of turbulence kinetic energy.…………………………......57

Figure 3.17. Sketch of the two turbines in tandem and the wake measurements locations ……..57

Figure 3.18. Nibe experiment for two turbines in tandem: Wake profile of velocity for $V_o =$ $8.5\ ^{\mathrm{m}}/_{\mathrm{s}}$, $C_T = 0.82$ and $IT = 11\%$ at: $x/D = 6$, $x/D = 7.5$…………...………...………...….58

Figure 3.19. Sexbierum experiment for two turbines in tandem: Velocity contour for three different spacing s: $s/D = 5.5, 8$ and 15…………..……………………..…………...………59

Figure 3.20. Sexbierum experiment for two turbines in tandem: Wake velocity profile for $V_o = 8.5\ ^{m}/_{s}$, $C_T = 0.75$ and $TI = 10\%$ at $x/D = 8$ for three different turbine spacings s: $s/D = 5.5, 8\ and\ 15$……………………………………………………………………………60

Figure 3.21. Sexbierum experiment for two turbines in tandem: contours of turbulence kinetic energy for spacings of $s/D = 5.5, 8$ and 15………….………….……….……………..……..…62

Figure 3.22. Sexbierum experiment for two turbines in tandem: Wake profile of turbulence kinetic energy for $V_o = 8.5\ ^{m}/_{s}$, $C_T = 0.75$ and $TI = 10\%$ at $x/D = 8$ for spacings of $s/D = 5.5, 8$ and 15……….………..……….……….……….……….…….…….…….……63

Figure 3.23. Sexbierum experiment for two turbines in tandem: Pressure contours for spacings of $s/D = 5.5, 8$ and 15…………..…………..……….………….………….……...………..…..…64

Figure 3.24. 3D view of the domains set up for ABL analysis.…………….……………….………….…66

Figure 3.25. Sexbierum experiment: velocity profiles at three different locations downstream of the turbine comparted to a neutral ABL profile….……………………..………….……….…..…66

Figure 3.26. Sexbierum experiment: turbulence kinetic energy profiles at three different locations downstream of the turbine comparted to a neutral ABL profile……….….…………….……67

Figure 3.27. Sexbierum experiment: Reynold stresses at three different locations downstream of the turbine comparted to a neutral ABL profile……………….……………….…………...…68

Figure A.1. The 2D mesh used for the preliminary study……………………………..………...78

Figure A.2. The 3D mesh used for the results section……………………………..….………....79

Figure A.3. The mesh used for the ABL simulation ………….....……………………………...79

NOMENCLATURE

List of Abbreviations and Acronyms

ABL	Atmospheric Boundary Layer
AD	Actuator Disc
ADM	Actuator Disc Model
ALM	Actuator Line Model
BEM	Blade Element Momentum Method
CFD	Computational Fluid Dynamics
CPU	Central Processing Unit
CV	Control Volume
HAWT	Horizontal Axis Wind Turbine
LES	Large Eddy Simulations
RANS	Reynolds-Averaged Navier-Stokes
RNG	Renormalization Group
SST	Shear Stress Transport
TI	Turbulence Intensity
VAWT	Vertical Axis Wind Turbine

English Symbols

A	Surface Area
A_{CV}	Area of the Control Volume
$\vec{A}$	Surface Area Vector
A_1	Surface Area of the Far Wake
A_D	Surface Area of the Disc
a	Axial Induction Factor
a'	Tangential Induction Factor

a_k	Inverse Effective Prandtl Number for k
a_ε	Inverse Effective Prandtl Number for ε
B	Number of Blades
C_d	Drag Coefficient
C_l	Lift Coefficient
C_P	Power Coefficient
C_T	Thrust Coefficient
C_μ	Tuning Constant
C_θ	Azimuthal Component of Velocity
c	Chord Length or a Constant
c_n	Normalized Normal Force
c_t	Normalized Tangential Force
$cost_{\mathrm{t}}$	Turbine Cost
$cost_{\mathrm{land}}$	Land Acquisition Cost
$c_{1\varepsilon}$	Constant
$c_{2\varepsilon}$	Constant
$c_{3\varepsilon}$	Constant
$c_{4\varepsilon}$	Constant
D	Rotor Diameter or Drag Force
F	Force or a Blending Function
F_{axial}	Axial Force
F_{ext}	External Forces
F_{pres}	Forces due to the Pressure on the Lateral Boundary of the Control Volume
F_1	Blending Function
g_b	Kinetic Energy Production due to Buoyancy

g_k	Kinetic Energy Production due to the Mean Velocity Gradient
i, j	Index for the Tensor Notation
K	Corrected Resistance Coefficient or Von Karman's Constant
k	Turbulent Kinetic Energy or Resistance Coefficient
L	Lift Force
M	Torque
$\dot{m}$	Mass Flow Rate
$\dot{m}_{\mathrm{side}}$	Mass Flow Rate out the Side of the Control Volume
N	Number of Annular Elements
P	Shaft Power or Pressure
P_t	Production of Turbulent Kinetic Energy
ΔP	Pressure Difference
p_N	Normal Force
p_o	Pressure Upstream of the Rotor
p_T	Tangential Force
p_ε	A Term Representing the Energy Transfer Rate between Scales of Turbulence
R	Radius
R_ε	A Term that Improves the Responsiveness to Quickly Strained Flow
r	Radial Distance
$r_{1/2}$	Half-width
S	Spread
S_i	Source Term in Tensor Notation
S_k	User Defined Source Term
S_ε	User Defined Source Term
s	Separation Distance

T	Thrust
TI	Turbulence Intensity
t	Turbine
U_i, U_j	Velocity in Tensor Notation
$\overline{U}_i$	Average Velocity in Tensor Notation
U_∞	Wind Speed
u	Wind Speed
u_1	Wind Speed at the Rotor
$\bar{u}$	Mean Velocity
$\bar{u}_{\mathrm{hub}}$	Mean Velocity at Hub Height
$\tilde{u}_o$	Unperturbed Resolved Velocity of the Axial Incident Flow
u^*	Friction Velocity
u'	Friction Velocity
V_o	Upstream Wind Speed
V_{rel}	Relative Velocity
$\vec{V}$	Velocity Vector
v'	Fluctuating Velocity Component
w'	Fluctuating Velocity Component
x	Downstream Distance
y	Lateral Distance
y_m	The Contribution from the Fluctuating Dilatation in Compressible Turbulence to Overall Dissipation Rate
z	Height
z_0	Roughness Length

Greek Symbols

α	Angle of Attack or a Non-dimentionalised Design Constant
β	Constant or a Closure Coefficient
β^*	Closure Coefficient
δ	Boundary Layer Depth
ε, ε_0	Dissipation
ϕ	Angle between Relative Velocity and Plane of Rotation
γ	Tuning Constant
η	Strain Rate Factor
η_{o}	Strain Rate Factor Constant
μ	Viscosity
μ_{eff}	Effective Viscosity
θ	Local Pitch Angle
ρ	Density
σ	Solidity or Prandtl Number
σ_u^2	Velocity Variance Components in the Streamwise Direction
σ_v^2	Velocity Variance Components in the Spanwise Direction
σ_w^2	Velocity Variance Components in the Vertical Direction
τ_o	Surface Shear Stress
v_t	Turbulent or Eddy Viscosity
ω	Rotational Speed or Turbulent Dissipation Rate

Chapter 1. Introduction

The increase in the price of oil, as well as concerns about limited fossil fuel supplies in 1973, prompted the development of wind energy (Burton et al., 2011). The relatively low CO_2 emissions and the promise of wind energy to help mitigate climate change were the major drivers for using wind turbines to generate electrical power starting about 1990. Then, from 2006, the very high oil price and worries about energy security sparked a renewed interest in wind energy, and a multitude of legislative initiatives were implemented in a number of nations to stimulate its use. In Canada, installed wind energy capacity reached 13.413 GW in the year 2019, and the projected value for the year 2040 is around 20 GW (Government of Canada, 2021).

A wind turbine converts the kinetic energy of the air passing through the rotor into electrical energy. Wind turbine aerodynamics is concerned with the modelling and prediction of aerodynamic forces on a wind turbine's solid components, particularly the rotor blades (Sørensen, 2012). For the design, development, and optimization of wind turbines, an integrated aeroelastic model for forecasting performance and structural deflections is required.

As wind farms develop, the rotor diameter and height of wind turbines increase. Wind farm design and optimization requires an understanding of the flow dynamics imposed by the atmospheric boundary layer (ABL) and local turbine wake interactions. Turbine wakes not only reduce downstream mean velocity, resulting in lower power output, but they also cause structural fatigue by increasing fluctuations. The wakes in a cluster of wind turbines result in areas of lower wind velocity and often higher turbulence than the ambient undisturbed wind (Kalvig, Manger, & Hjertager, 2014). This will introduce two major issues: decreased power and increased dynamic loads on the blades. Atmospheric turbulence, wind shear from the ground effect, changing wind directions in time and space, and influences from surrounding wind turbines all affect wind turbine performance. These issues motivate a better understanding of the wake profile and turbine interactions.

This thesis will explore the role of computational fluid dynamics (CFD) as a tool for understanding wind turbine wake characteristics, using the actuator disc model implemented in a Reynolds Averaged Navier-Stokes (RANS) computational domain with different 2-equation turbulence closure models.

1.1 Background

1.1.1 History of Wind Energy

Wind energy has a rich history that goes back thousands of years. Wind energy was used to propel boats in old Egypt on the Nile River as early as 5000 BC; later, around 200 BC, windmills were used to grind grain in Persia and the Middle East, and to pump water in China (Fleischer, 2021). Horizontal axis windmills have been an element of the rural economy since the middle ages, and only fell out of favor with the arrival of inexpensive fossil-fueled stationary engines and subsequently the expansion of rural electricity (Musgrove, 2010).

The use of machines to generate electricity is traced back to the late nineteenth century work of Charles Brush in the USA and Poul la Cour in Denmark, and their 12 kW DC wind powered generator (Burton et al., 2011). Later, in 1941, a notable development was the Smith-Putnam 1250 kW generator in the USA. Although the machine failed catastrophically in 1945 (Putnam, 1948), it remained one of the largest ever built for almost 40 years (Burton et al., 2011).

In 1956, the 200 kW Gedser machine was developed in Denmark, and in 1963, Electricite de France tested a 1.1 MW 35 m diameter turbine called Golding. Professor Ulrich Hutter built a series of revolutionary, lightweight turbines in Germany throughout the 1950s and 1960s. Despite these technological advancements and the excitement generated by the Golding turbine at the Electrical Research Association in the United Kingdom, and elsewhere, there was little persistent interest in wind power until the price of oil soared substantially in 1973 (Burton et al., 2011).

After realizing the threat to fossil fuel supplies, European and North American countries started to research and develop renewable energy sources such as wind energy. Denmark for example, became a pioneer in creating commercial wind power in the 1970s, and Danish manufacturers and component suppliers now produce a large portion of the world's wind turbines (From oil crisis to energy revolution, 2019).

1.1.2 Types of Wind Turbines

Wind turbines are usually classified into two types: vertical axis wind turbines (VAWTs) and horizontal axis wind turbines (HAWTs).

VAWTs mainly utilize both the drag and lift forces. This type of wind turbine accepts wind from all directions, as the blades are arranged vertically around the tower. This removes the need for a yawing system to align the rotor with the wind direction. The drive train and generator for VAWTs is installed at the ground level, minimizing maintenance cost, risk, and the initial investment (Dvorak, 2014). VAWTs have the capacity to scale down while still being fairly efficient. This can be useful in urban areas or rooftops. Despite the benefits, there are several reasons why many people are doubtful of VAWTs' ability to be adopted in a wind farm. VAWTs are less efficient compared to HAWTs. They also have an up-scaling issue. A large VAWT must be secured by tension wires (Dvorak, 2014). For a large scale wind farm, VAWTs will require more material and land space, and the overall efficiency will be lower than a HAWT.

On the other hand, HAWTs use the lift force and are referred to as lift machines. The rotor is mounted horizontally on the tower, and a yawing system is usually installed at the rotor level, to orient it with the wind direction. HAWTs are more efficient than VAWTs on a large scale, and they require less space at ground level. The generator and the drive train are also installed at the level of the rotor. While HAWTs are more efficient, they have higher maintenance cost, and the additional cost of the yawing system (Gardiner, 2011). They also present higher risk to the maintenance technicians, and wildlife (Dvorak, 2014).

1.1.3 Rotor Design

The tip speed ratio (the ratio of blade tip velocity to wind velocity) is chosen to maximize the power coefficient. The value chosen has a significant influence on the turbine's overall design. First and foremost, the design tip speed ratio and the rotor's solidity (the area of the blades relative to the swept area of the rotor) are closely linked. A rotor with longer blades and a greater speed will have less blade area, or solidity, than a rotor with shorter blades and a lower speed. The chord and thickness of the blades will decrease when the solidity of the turbine is lower for a constant number of blades. There is a limit to how thin the blades can be due to structural constraints. As a result, the number of blades typically reduces as the solidity lowers.

Using greater tip speed ratios has multiple advantages. To begin with, lowering the number of blades or their weight lowers the price. Second, for a given power level, greater rotational speeds correspond to lower torques, resulting in less stress on the turbine's drive train and gearbox (McGowan et al., 2000). High tip speed ratios, on the other hand, have certain disadvantages. Higher-speed rotors for example are often noisier and they are more susceptible to leading edge corrosion.

The choice of the number of blades is dictated by design constraints and factors. Most of the available commercial size HAWT wind turbines uses a three-blade design. A two-blade wind turbine will experience elevated cyclic stresses, as the moment of inertia of the rotor will be lower when the blades are vertical, than when they are horizontal. This phenomenon will increase wear on the turbine (Burton et al., 2011). Also, the choice of four or more blade wind turbines will increase the cost, and add more stresses on the hub and the tower. So, the three-blade design is considered to be the best configuration for commercial size wind turbines.

1.1.4 Aerodynamic Controls

Elevated wind speeds can damage a wind turbine. Almost all modern wind turbines come with a control system to prevent such outcomes. Some methods used to control the rotation of a wind turbine are control, variable pitch control, and yaw control.

Stall control reduces the excess lift caused by elevated wind speeds, by changing the angle of attack of the blades. As the wind speed increases, the relative wind speed, which is a result of the incident flow and rotation, will change the angle of attack of the blade, causing stall (Apata & Oyedokun, 2020). This control system was used in the early years of wind energy, and is less common now. The reason for this is the increased vibrations and swirl because of the excessive turbulence.

Changing the angle of the blades along their long axis allows for variable pitch control. This reduces the amount of lift force available to turn the rotor, giving greater control than stall control. In order to provide the required mechanical control, variable pitch control necessitates a more complex hub assembly. Some designs have a partial span pitch control option as an alternative to complete blade pitch control (McGowan et al., 2000).

Another way to control the power output of a wind turbine is yaw control. This method requires a reliable yawing system to turn the rotor away from the wind, and to withstand gyroscopic wind loads (McGowan et al., 2000).

1.1.5 Environmental Impact and Noise

Wind energy development has positive and negative impacts on the environment. Being a clean energy, the environmental benefit of wind energy is usually calculated by the carbon emissions avoided by using it. Although the low carbon footprint of wind energy is enough to justify its use, some environmental aspects limit its expansion.

Wind turbines have been linked to bird and bat deaths. Moreover, large wind farms invade the natural habitat of some animals, and impact the migration routes for some birds.

Some early wind turbines built in the 1980s were extremely noisy, to the point that it was annoying to hear them from a mile away (Maine Government, 2000). Industry quickly responded to this problem, and wind farms have become quieter.

1.2 Objectives

Understanding turbine interactions is becoming increasingly important as the number of turbines in on- and off-shore wind farms grows. The turbulence intensity increases as flow passes a turbine, amplifying the fatigue stress on downstream turbines. Furthermore, because power is related to the cube of velocity, the velocity deficits in turbine wakes can have a significant impact on downstream power generation. When more than one turbine is involved, the complexity of the flow mechanics increases.

This research will explore the role of computational fluid dynamics (CFD) as a tool for investigating wind turbine wake characteristics. This is done using the actuator disc model (ADM). This method was first developed by Rankine in 1865 and later enhanced by Greenhill in 1888 and Froude in 1889 (Mikkelsen, 2004). The first part of this study will explore the wake characteristics of a standalone wind turbine, and the second part will explore the wake interactions between two turbines only in tandem. For both cases, only a single wind direction is considered.

Figure 1.1 shows the famous picture of Horns Rev wind farm, which demonstrates the wake expansion of wind turbines in a wind farm. Christiansen and Hasager (2006) found that the velocity deficit can be as high as 20% in the wake of a wind turbine. Velocity deficit and turbine interactions must be better understood and modelled in order to deal with wake effects on this scale. Wind farms can be constructed to better maximize power production and reduce fatigue damage with a better knowledge of wind turbine wake interactions using enhanced modelling approaches, thus lowering operating costs.

Figure 1.1. Photograph of the wake expansion of Horns Rev wind farm (© Vattenfall, Horns Rev 1 owned by Vattenfall. Photographer Christian Steiness) (Emeis, 2010) “Reproduced with Permission of the Publisher/Owner, See Appendix B”

The overall objective of this research is to perform a CFD study of a standalone wind turbine using an ADM and RANS formulation, as well as the wake interaction of two inline turbines located in tandem.

This will be accomplished in the following parts:

1. A parametric study of CFD for the different turbulence closure models;
2. A CFD study of the AD/RANS model for a standalone wind turbine under different inflow conditions, including a neutral ABL study;
3. A CFD study of the wake of a turbine located directly downstream of another turbine.

All parts of this research will be performed using the finite volume commercial CFD software ANSYS/Fluent (ANSYS, 2020). The purpose of part one is to determine the applicability of the commonly used turbulence closure models, and to compare them with the different recommendations from the literature. Part 2 will compare the prediction of a simple AD/RANS model with experimental results for the far wake. Finally part 3 will explore the velocity deficit for wind turbines in tandem.

1.3 Thesis Organization

This thesis consists of four chapters. Chapter 1 is the introduction, which gives a general overview of wind energy and presents the objectives of this research. Chapter 2 presents a literature review of different numerical methods used in the wind industry, and relevant scholarly publications. This will document the current methods used in analyzing wind turbines, and will demonstrate the role of CFD.

Chapter 3 will explore wake predictions using the AD/RANS model. This includes a technical review of different turbulence models, as well as a parametric study of the performance using CFD simulations. Chapter 4 summarizes the work done in this research, the results and findings, and notes possible future work. Finally, the appendices will present the meshes used in the simulations and the permissions to use figures.

Chapter 2. Literature Review

The purpose of this literature review is to summarize the different methods used for analyzing the wake of a stand-alone horizontal axis wind turbine, as well as for studying the wake interaction of several turbines in tandem. The chapter will first reviews one-dimensional momentum theory and classical blade element momentum theory. Next, it presents a brief literature review of the CFD studies using an actuator disc, actuator line, and fully resolved blade models.

2.1 One-dimensional Momentum Theory

A wind device in its most basic definition converts the translational kinetic energy of the wind into rotational kinetic energy that is available as shaft work. In this context, the rotor can be modeled as a permeable disc that impedes the flow just enough to create the same effects as the rotating rotor. The disc is assumed to be frictionless and static, and there is no rotational velocity component in the wake. The rotor disc works as a drag mechanism, reducing the wind speed from V_o upstream to u at the rotor plane and to u_1 in the far wake. As a result, the streamlines must diverge as shown in figure 2.1. A pressure decrease across the rotor will produce a drag force. There is a pressure rise from upstream p_o to p close to the rotor, before a discontinuous pressure decrease through the rotor. The pressure gradually returns to ambient conditions downstream of the rotor. With the Mach number being low, the air density remains constant, therefore the axial velocity must gradually drop from V_o to u_1. Figure 2.1 also idealizes the pressure and axial velocity behavior.

The flow here is assumed to be incompressible and frictionless, and the rotor is assumed to be stationary. Using these assumptions, a relation between the velocity components, thrust on the rotor, and the power produced can be derived. The thrust is the force in the streamwise direction, creating a pressure drop, and reducing the wind speed. It is given by

$$T = \Delta pA \quad (2.1)$$

where T is thrust, Δp is pressure difference and A is the surface area of the rotor.

Based on the previous assumptions about the flow, and the absence of any external forces on the flow, Bernoulli's equation can be used,

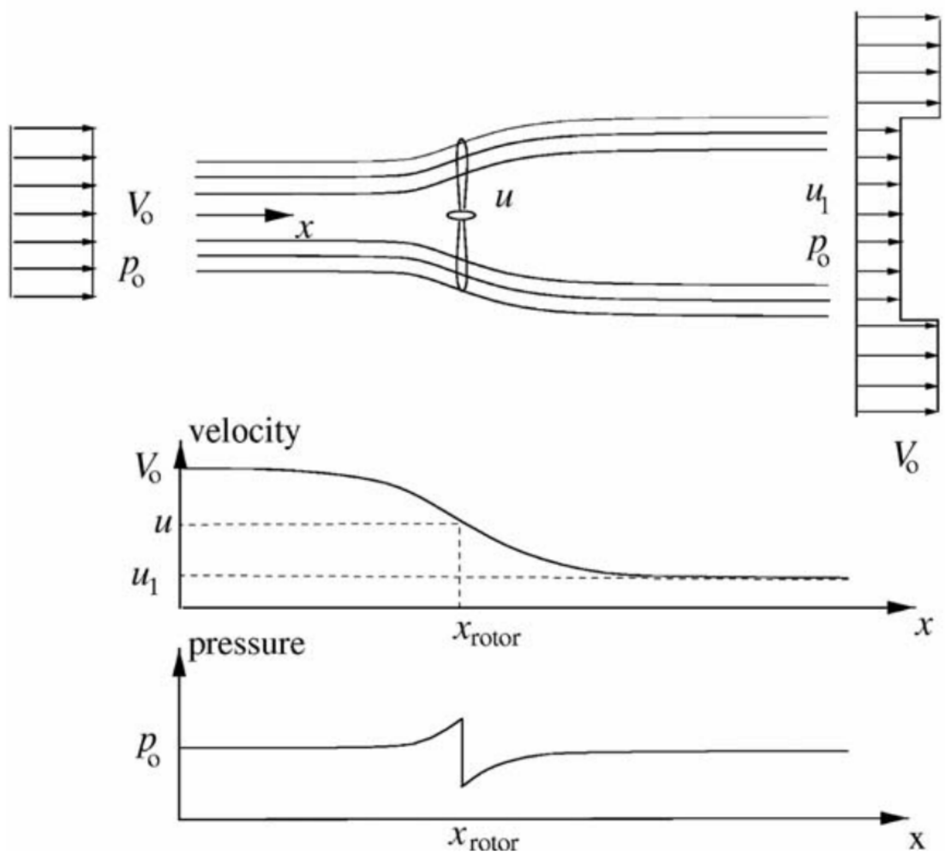

Figure 2.1. Illustration of the 1D momentum theory (Hansen, 2008) "Reproduced with Permission of the Publisher/Owner, See Appendix B"

$$p_o + \frac{1}{2}\rho V_o^2 = p + \frac{1}{2}\rho u^2 \quad (2.2)$$

and the pressure just downstream of the actuator disc becomes $p - \Delta p$. If the pressure drop across the actuator disc is defined as Δp, then the downstream Bernoulli's equation becomes

$$p - \Delta p + \frac{1}{2}\rho u^2 = p_o + \frac{1}{2}\rho {u_1}^2 \quad (2.3)$$

Combining equations (2.2) and (2.3) yields an expression for the pressure drop across the rotor

$$\Delta p = \frac{1}{2}\rho\left(V_o^2 - {u_1}^2\right) \quad (2.4)$$

For the circular control volume with sectional area A_{cv}, shown in figure 2.2, the axial momentum equation written in integral form is

$$\frac{\partial}{\partial t}\iiint_{cv} \rho u dx dy dz + \iint_{cs} u\rho \vec{V} \cdot d\vec{A} = F_{\mathrm{ext}} + F_{\mathrm{pres}} \quad (2.5)$$

where t is time, ρ is density, *CV* is control volume, V is velocity, A is area of the rotor, A_1 is the area of the wake, and $\dot{m}$ is the mass flow rate.

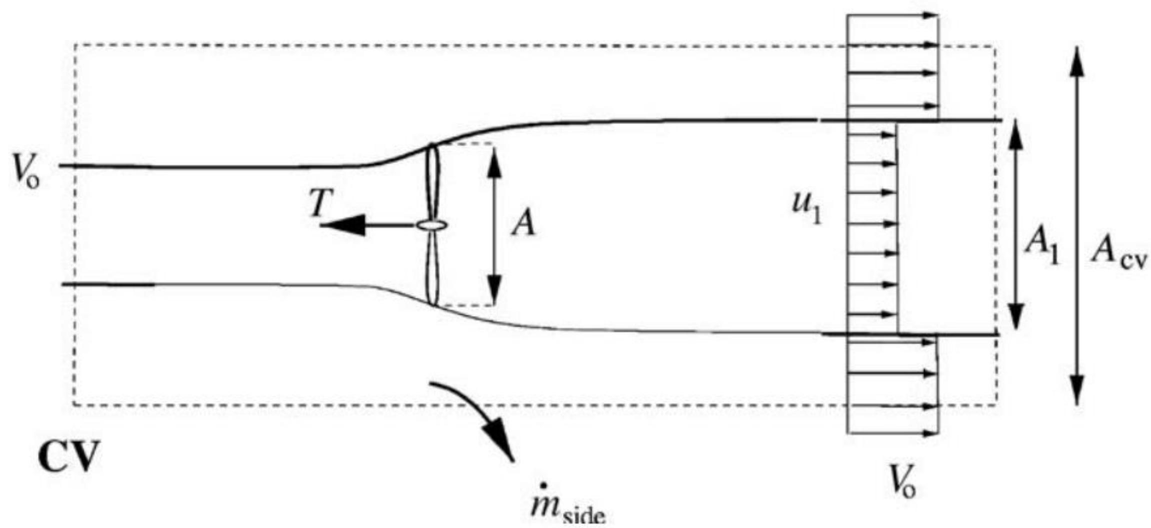

Figure 2.2. Circular CV representing the flow field (Hansen, 2008) "Reproduced with Permission of the Publisher/Owner, See Appendix B"

Because the flow is assumed to be steady, the first term on the LHS of equation (2.5) is zero. F_{ext} represents the external force acting on the control volume, while F_{pres} represents the axial pressure on the lateral boundary of the control volume. The previous assumptions imply that F_{ext} will be the thrust force and F_{pres} is zero. $d\vec{A}$ is a vector of infinitesimal length pointing outward in the normal direction of the control surface.

Evaluating the second term on the LHS gives

$$\rho {u_1}^2 A_1 + \rho {V_o}^2 (A_{cv} - A_1) + \dot{m}_{side} V_o - \rho {V_o}^2 A_{cv} = -T \quad (2.6)$$

Using conservation of mass

$$\rho A_1 u_1 + \rho (A_{cv} - A_1) V_o + \dot{m}_{side} = \rho A_{cv} V_o \quad (2.7)$$

and

$$\dot{m} = \rho A \, u = \rho A_1 u_1 \quad (2.8)$$

Then, the mass flow rate out the side becomes

$$\dot{m}_{\text{side}} = \rho A_1 (V_o - u_1) \quad (2.9)$$

Combining equations (2.6), (2.8) and (2.9)

$$T = \rho u A (V_o - u_1) = \dot{m} \, (V_o - u_1) \quad (2.10)$$

An interesting and useful observation from equations (2.1), (2.4) and (2.10) is the value of the velocity at the rotor

$$T = \rho u A (V_o - u_1) = \Delta p A = \frac{1}{2} \rho A \left(V_o^2 - {u_1}^2 \right) \quad (2.11)$$

$$u = \frac{1}{2} (V_o + u_1) \quad (2.12)$$

Equation (2.12) identifies that the velocity at the rotor is the average between the upstream wind speeds V_o and the velocity in the wake u_1.

The shaft power at the rotor can be related to the thrust created and the velocity at the rotor, i.e.

$$P = Tu \quad (2.13)$$

From equation (2.11), the shaft power is given as

$$P = \frac{1}{2} \rho u A \left(V_o^2 - {u_1}^2 \right) \quad (2.14)$$

The fractional decrease in wind velocity caused by the rotor is defined to be the axial induction factor, a,

$$a = \frac{V_o - u}{V_o} \quad (2.15)$$

Combining equations (2.12) and (2.15) gives

$$u_1 = (1 - 2a)V_o \quad (2.16)$$

This can then be used in equations (2.10) and (2.14) to gives expressions for the power and the torque created at the rotor in terms of a,

$$P = 2\rho V_o^3 a(1 - a)^2 A \quad (2.17)$$

$$T = 2\rho V_o^2 a(1 - a)\, A \quad (2.18)$$

The power and thrust are often non-dimensionalized with respect to the available value in the free wind, to create the following power and thrust coefficients:

$$C_p = \frac{P}{\frac{1}{2}\rho V_o^3 A} \quad (2.19)$$

$$C_T = \frac{T}{\frac{1}{2}\rho V_o^2 A} \quad (2.20)$$

Using equations (2.17) and (2.18), then

$$C_p = 4a(1 - a)^2 \quad (2.21)$$

$$C_T = 4a(1 - a) \quad (2.22)$$

Differentiating the power coefficient with respect to a gives

$$\frac{dC_p}{da} = 3a^2 - 4a + 1 \quad (2.23)$$

It is readily shown that the maximum power coefficient is ${}^{16}/{}_{27}$ for the value $a = {}^{1}/{}_{3}$. This value is the maximum theoretical power output of a wind turbine, referred to as the Betz limit, as shown in figure 2.3.

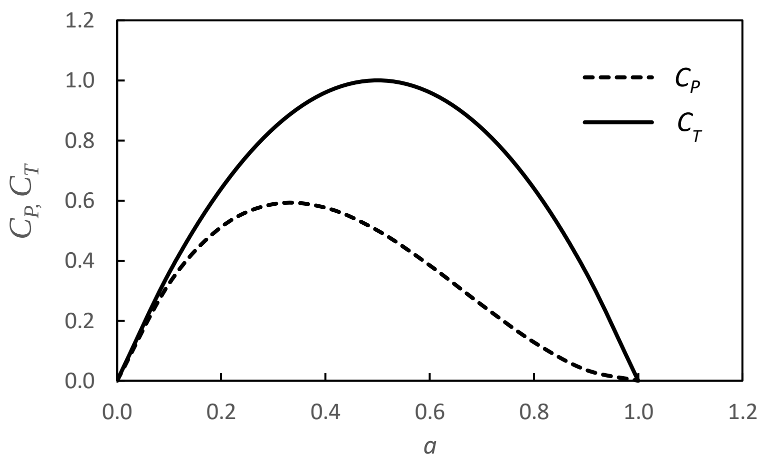

Figure 2.3. The power and thrust coefficients as a function of the axial induction factor

Experimental analysis (Eggleston & Stoddard, 1987) has shown that the momentum theory is valid for an axial induction factor of less than 0.4. If the value of a is larger than 0.5, equation (2.16) would give a negative value for u, which is unrealistic.

2.2 Blade Element Momentum

2.2.1 Theory

The blade element momentum theory (BEM) is the classical and the most widely used method for analyzing and calculating the local forces on open propellers and wind turbines. The method was developed by Glauert (1926, 1935), and it was based on momentum theory (Rankine, 1865 and Froude, 1889) and blade element theory (Froude, 1878). The BEM model's main contibution is to identify the best conditions for optimum energy conversion (Leishman, 2006). A steady, frictionless, and incompressible flow is assumed for the BEM technique. Angular momentum is incorporated in the blade element momentum theory, implying that when the fluid interacts with the rotor, it begins to rotate around the main stream axis.

In the framework of wind turbines, the blade is divided into elements, with each blade element approximated by a planar model. Multiple forces acting on the blade element as functions of flow characteristics and blade geometry are obtained. The two experimental coefficients (typically designated by C_l and C_d; lift and drag coefficients, respectively) that account for the forces in the cross-section as functions of the angle of attack, i.e. the relative angle between the spinning blade and flow, are the essential parameters of this model. To obtain global values, the findings at each section are then integrated along the blade. The BEM was adopted by Lanchester (1915), Betz (1920), and Joukowsky (1920) to create the Betz limit or the Betz-Joukowsky limit, which gives the maximum theoretical output power of a wind turbine.

In the BEM, the stream-tubes defined in the momentum theory are discretized into N annular elements with thickness dr as shown in figure 2.4, where r is the radial distance from the center, and R is the radius.

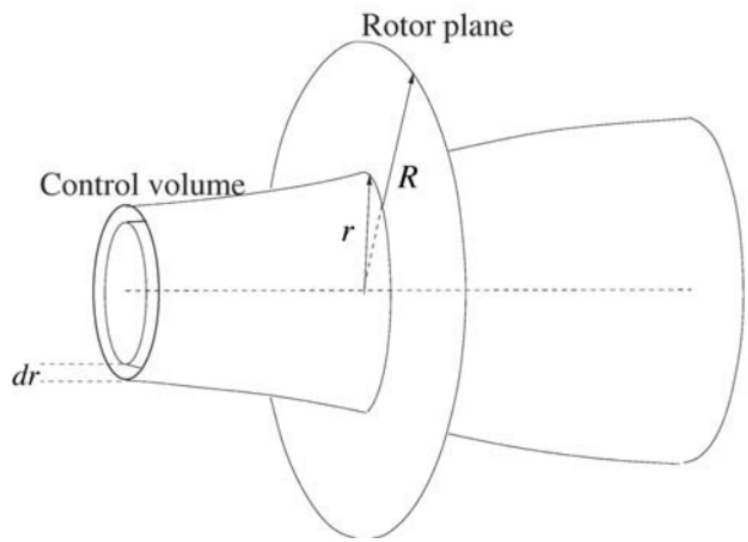

Figure 2.4. Annular elements of the BEM (Hansen, 2008) “Reproduced with Permission of the Publisher/Owner, See Appendix B”

The BEM assumes no radial dependency between the annuli, meaning that the elements are independent of the flow on adjacent elements. Also, the force created by the elements is constant through the flow over the rotor plane, implying an infinite number of blades. These assumptions seem to be non-physical, which necessitates some corrections to the behavior of this method, which will be discussed in the following sections.

Applying the results from equation (2.10), the elemental thrust force on each annulus is found to be

$$dT = (V_o - u_1)d\dot{m} \;= 2\pi r\rho u(V_o - u_1)dr \quad (2.24)$$

$$dT = 4\pi r\rho u V_o^2 a(1-a)dr \quad (2.25)$$

From momentum theory, an ideal turbine has no wake rotation, but this is not the case for an actual turbine with a constant number of blades. According to the blade element theory, flow past a particular section is 2D, and the effective inflow velocity can be determined as the vector sum of the incoming velocity and rotational speed. To include the rotational speed at each element, the tangential induction factor a' (Mikkelsen, 2004) was defined as

$$a' = \frac{C_\theta}{2\omega r} \qquad (2.26)$$

where C_θ is the azimuthal component of the velocity, and ω is the rotational speed of the rotor.

According to Euler's turbine equation (Euler, 1752), the relation between power output and torque is defined as

$$dP = \omega dM = \dot{m}\omega r C_\theta = 2\pi r^2 \rho u \omega C_\theta dr \qquad (2.27)$$

where M is the torque.

So, the equation for the torque on each element is conveniently given as

$$dM = 4\pi r^3 \rho V_o (1-a) a' dr \qquad (2.28)$$

Figure 2.5 shows a section of the blade with the velocity components shown, where V_{rel} is the relative velocity

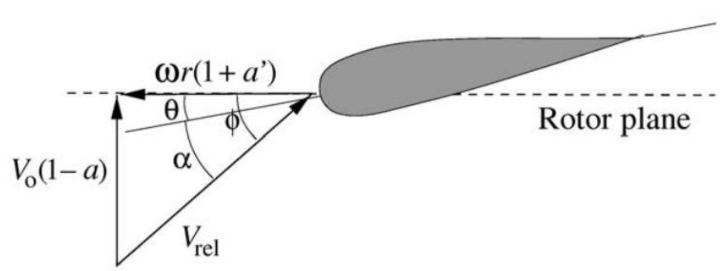

Figure 2.5. Velocities at the rotor plane (Hansen, 2008) "Reproduced with Permission of the Publisher/Owner, See Appendix B"

Here θ is the local pitch angle, which is a combination between the twist of the blade and the pitch angle, α is the local angle of attack, and ϕ is the angle between the relative velocity and the plane of rotation.

From figure 2.5

$$\alpha = \phi - \theta \quad (2.29)$$

$$\tan\phi = \frac{(1-a)V_o}{(1+a')\omega r} \quad (2.30)$$

By understanding that the velocity seen by the airfoil is V_{rel}, the lift and drag forces per unit span can be defined for each element

$$L = \frac{1}{2}\rho V_{rel}^2 c C_l \quad (2.31)$$

$$D = \frac{1}{2}\rho V_{rel}^2 c C_d \quad (2.32)$$

where C_l and C_d are the lift and drag coefficients, and c is the chord

The lift and drag forces per unit span will then be used to determine the normal and tangential forces per unit span (figure 2.6) for the BEM theory

$$p_N = L\cos\phi + D\sin\phi \quad (2.33)$$

$$p_T = L\sin\phi - D\cos\phi \quad (2.34)$$

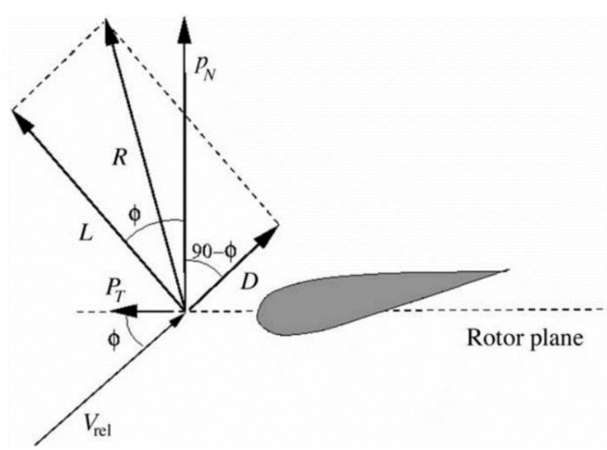

Figure 2.6. The loads on a blade (Hansen, 2008) "Reproduced with Permission of the Publisher/Owner, See Appendix B"

Equations (2.33) and (2.34) are then normalized with $\frac{1}{2}\rho V_{rel}^2 c$ to give

$$C_n = C_l \cos\phi + C_d \sin\phi \qquad (2.35)$$

$$C_t = C_l \sin\phi - C_d \cos\phi \qquad (2.36)$$

where

$$C_n = \frac{p_N}{\frac{1}{2}\rho V_{rel}^2 c} \qquad (2.37)$$

$$C_t = \frac{p_T}{\frac{1}{2}\rho V_{rel}^2 c} \qquad (2.38)$$

A solidity σ is defined as the fraction of the annular area that is covered by blades

$$\sigma(\mathrm{r}) = \frac{c(r)B}{2\pi r} \qquad (2.39)$$

where $c(r)$ is the chord at the radial distance r, and B is the number of blades.

From figure 2.5, it is readily seen that

$$V_{rel} = \frac{V_o(1-a)}{\sin\phi} \qquad (2.40)$$

and

$$V_{rel} = \frac{\omega r(1+a')}{\cos\phi} \qquad (2.41)$$

From the equations of elemental normal and tangential forces, the thrust and torque on the control element is defined as

$$dT = Bp_N dr \qquad (2.42)$$

$$dM = rBp_T dr \qquad (2.43)$$

Using equations (2.37), (2.38), (2.40) and (2.41); the thrust and torque equations become

$$dT = \frac{1}{2}\rho B \frac{V_o^2(1-a)^2}{\sin^2\phi} cC_n dr \qquad (2.44)$$

$$dM = \frac{1}{2}\rho B \frac{V_o(1-a)\,\omega\mathrm{r}(1+a')}{\sin\,\phi\cos\phi} cC_t r dr \quad (2.45)$$

If equations (2.25) and (2.44) are equated as well as equations (2.28) and (2.45), and the definition of solidity is implemented in them, new expressions for the axial and tangential induction factors will be

$$a = \frac{1}{\frac{4\sin^2\phi}{\sigma C_n} + 1} \quad (2.46)$$

$$a' = \frac{1}{\frac{4\sin\,\phi\cos\phi}{\sigma C_t} - 1} \quad (2.47)$$

Using the series of equations presented in this section, the BEM theory uses an iterative solution technique for determining the local loads on each blade element.

The tip vortical structure of the rotor necessitates another correction for the BEM algorithm. Also, the momentum theory, which is the basis of the BEM theory, is not valid for axial induction factors of more than approximately 0.4. To correct these two phenomena, Prandtl (Glauert, 1935) introduced a tip loss correction factor, and Glauert (1935) introduced an empirical relation between the thrust coefficient and the axial induction factor for a heavily loaded rotor, i.e. a is greater than 0.4.

2.2.2 Prandtl's Tip Loss Correction Factor

For a finite number of blades, Prandtl (Glauert, 1935) derived a correction factor F for the thrust and torque equations (2.25 and 2.28) as follows:

$$dT = 4\pi r\rho u V_o^2 a(1-a)F dr \quad (2.48)$$

$$dM = 4\pi r^3 \rho V_o(1-a)Fa' dr \quad (2.49)$$

where

$$F = \frac{2}{\pi}\cos^{-1}(e^{-f}) \quad (2.50)$$

and

$$f = \frac{B}{2}\frac{(R-r)}{r\sin\,\phi} \quad (2.51)$$

Using the same analysis as presented in the previous section, the axial and tangential induction factors become

$$a = \frac{1}{\frac{4\,F\sin^2\phi}{\sigma C_n} + 1} \quad (2.52)$$

$$a' = \frac{1}{\frac{4\,F\sin\,\phi\cos\phi}{\sigma C_t} - 1} \quad (2.53)$$

2.2.3 Glauert Correction for axial momentum factor

When the axial induction factor exceeds 0.4, the momentum theory fails. This was pointed out in several experimental studies (Eggleston and Stoddard, 1987). To correct this behavior, several empirical formulas were introduced between the thrust coefficient and the axial induction factor

$$C_T = \begin{cases} 4a(1-a)F, & a \leq \frac{1}{3} \quad (2.54) \\ 4a\left(1 - \frac{1}{4}(5-3a)a\right)F, & a > \frac{1}{3} \quad (2.55) \end{cases}$$

or

$$C_T = \begin{cases} 4a(1-a)F, & a \leq a_c \quad (2.56) \\ 4(a_c^2 + (1-2a_c)a)F, & a > a_c \quad (2.57) \end{cases}$$

The second expression is from Spera (1994).
The thrust coefficient by definition is

$$C_T = \frac{dT}{\frac{1}{2}\rho V_o^2 2\pi r dr} \quad (2.58)$$

If equation (2.44) is used for dT in equation (2.58), the thrust coefficient becomes

$$C_T = \frac{(1-a)^2\sigma C_n}{\sin^2\phi} \quad (2.59)$$

Then equation (2.59) is now equated to the empirical equations (2.56) and (2.57)

If $a \leq a_c$,

$$a = \frac{1}{\frac{4\,F \sin^2\phi}{\sigma C_n} + 1} \quad \text{.......} (2.60)$$

which is the same as equation (2.52).

If $a > a_c$,

$$a = \frac{1}{2}\left[2 + K(1 - 2a_c) - \sqrt{(K(1 - 2a_c) + 2)^2 + 4(Ka_c^2 - 1)}\right] \text{.......} (2.61)$$

where

$$K = \frac{4F \sin^2\phi}{\sigma C_n} \quad \text{.......} (2.62)$$

The Glauert correction is useful only for low wind speeds, when the axial induction factor is high.

The algorithm in figure 2.7 summarizes the BEM without the Glauert correction. To introduce this correction, the induction factors presented in equations (2.60) and (2.61) are introduced.

The BEM is the classical tool for analysis of loads on wind turbines. It is widely used in industrial applications for designing and assessing the efficiency of a wind machine. While this method is very useful, it is 2D and includes certain assumptions and empirical analysis. BEM theory alone cannot predict the wake of a wind turbine, nor the interaction between two turbines in tandem. For these features, numerical analysis using computational fluid dynamics can be used.

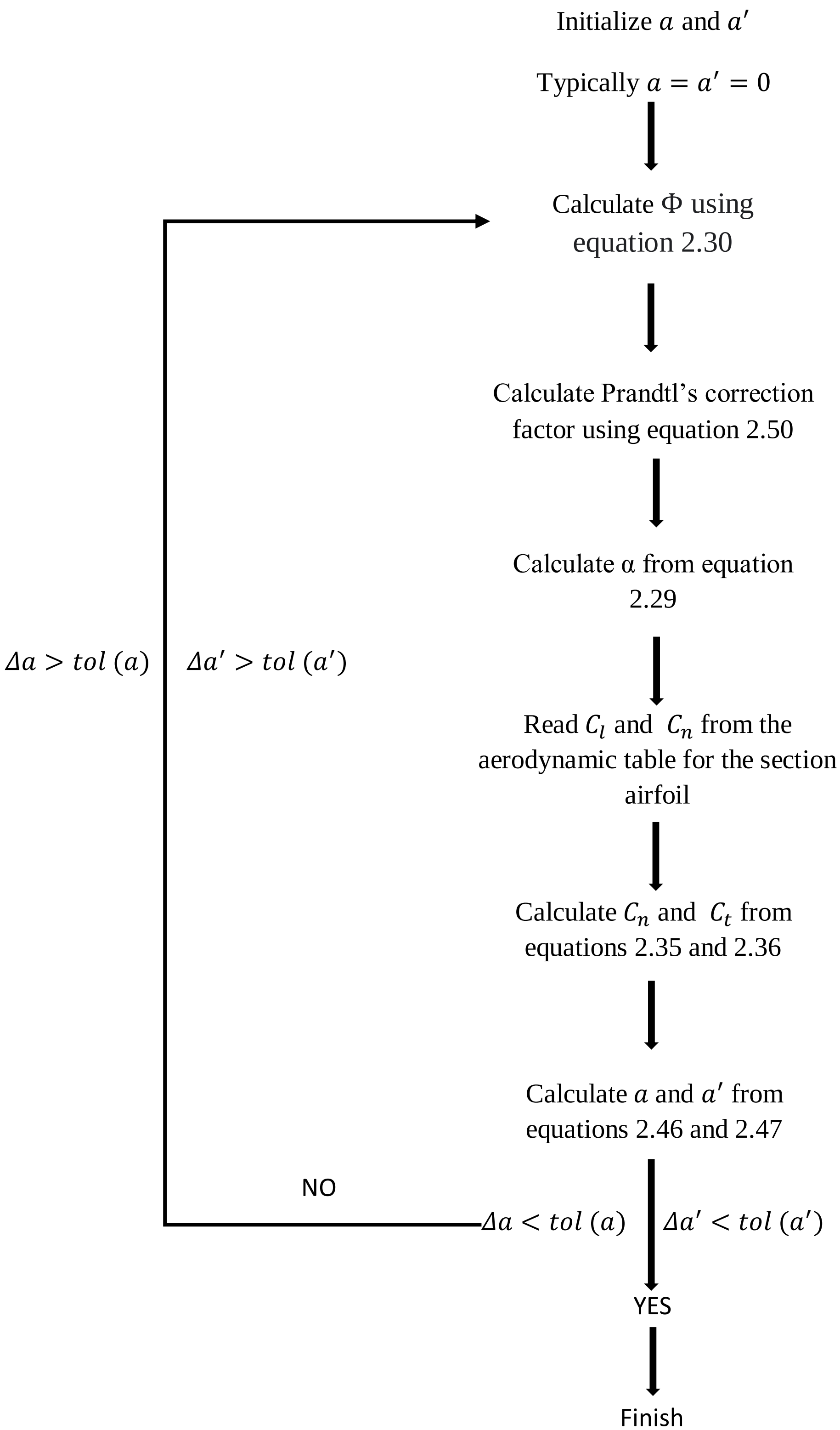

Figure 2.7. BEM solution algorithm

2.3 Numerical Models

Wind turbine aerodynamics can appear simple when compared to the aerodynamics of fixed-wing aircraft or helicopters. There are, however, a few additional complexities. Most notably, aerodynamic stall is often avoided in aircraft, whereas it is an inherent part of the operating envelope of wind turbines (Schaffarczyk, 2014). Estimating power generation, assessment of turbine loads, and wake modelling play a critical role in planning wind farm. Wind farm models must be relatively accurate – to reduce financial risk – while also being cost-effective, so that a large number of configurations may be evaluated in a reasonable amount of time (Aubrun et al., 2014). While many models have been presented in the literature, one that stands out is the Reynolds Averaged Navier-Stokes (RANS) equations with a two-equation turbulence closure and an actuator disc representation of the rotor. The actuator disc is a rotor performance analysis methodology. The rotor is represented by a porous disc that enables the flow to pass through it while still being subject to surface forces. The classical actuator disc model is based on mass, momentum, and energy conservation.

Empirical models, such as the BEM approach, have been critical in the growth of the wind energy sector. However, advanced CFD models will be necessary to fulfil demand and as the industry grows and farm locations become scarcer, resulting in higher density turbine deployment (Bazilevs, et al., 2010). Several research groups have been studying different challenges for the industry, including wind turbine wake interactions (Tachos, et al., 2010; PortéAgel, et al., 2011), atmospheric wind farm effects and turbine configurations (Calaf, et al., 2010; Wu et al. 2020), and turbine spacing (Meyers & Meneveau, 2011). These studies have employed different numerical approaches, such as RANS with turbulence closures (Hahm & Wußow, 2006; Tachos, et al., 2010), and large eddy simulation (LES) with different sub-grid scale (SGS) models (Calaf, et al., 2010; Meyers & Meneveau, 2011; PortéAgel, et al.; 2011 Wu et al. 2020).

Hahm and Wußow (2006) looked into the spacial organization of turbulence kinetic energy and compared their findings to empirical models. They utilized a $k-\varepsilon$ RANS model (k is the turbulence kinetic energy and ε is the dissipation) and a detached eddy simulation (DES) model to investigate the wake structure behind a 1 MW turbine. The turbulence intensity in the far wake was calculated using an empirical model that combines the upstream turbulence intensity with a bell-shaped turbulence intensity determined as a function of thrust coefficient and tip speed ratio.

Using a multiple reference frame model in FLUENT, the $k - \varepsilon$ RANS study simulated a previously investigated 55 kW turbine with a neutral atmospheric boundary layer (ABL). Although the results were somewhat able to simulate the downstream velocity profiles, the turbulence intensities along the edge of the wake were underestimated due to the averaging nature of RANS models (Hahm & Wußow, 2006).

Hahm and Wußow (2006) encountered troubles with the classic $k - \varepsilon$ RANS closure. Tachos et al. (2010) performed some studies using a RANS model with different turbulence closure models. The models used included Spalart-Allmaras, standard $k - \varepsilon$, $k - \varepsilon$ RNG, and the $k - \omega$ shear stress transport (SST) closure models (ω is the specific rate of dissipation). The simulation was run in a steady state using ANSYS-FLUENT.

The findings of Tachos et al. (2010) showed that the SST $k - \omega$ turbulence closure model gave the best approximation to the measured data. The other closure models which performed fairly well, except for the standard $k - \varepsilon$ model which performed quite poorly.

RANS simulations can produce accurate results, however they only compute the mean flow and parameterize the turbulence scales (Porté-Agel et al., 2011). LES simulations are necessary for more accurate and informative results. LES models employ a grid-based filter to resolve the flow when the mesh is fine enough, comparable to direct a numerical simulation (DNS), and an SGS model to represent the smallest scales where the mesh is too coarse. Typically the grid should be small enough to resolve 80% of the energy (Pope, 2000), which is a significant constraint for LES.

Porté-Agel et al. (2011) used a tuning-free Lagrangian dynamic SGS model previously developed for wind energy applications to represent single turbine wakes and wake interactions in an operational wind farm in an LES investigation. The time required to fully resolve a revolving wind turbine increases dramatically, as does the model complexity. An actuator disc model (ADM) can be used to function as a momentum sink with features similar to those of an actual wind turbine. This simplifies the model and reduces the computational cost.

Three different actuator disc models were investigated by Porté-Agel et al. (2011). The first was a model with a nonrotating actuator disc (ADM-NR). The Rankine-Fronde actuator disc model was chosen for this model because of its well-known ability to work with coarse grids. Because this model assumes that forces only operate in the axial direction, it is unable to represent rotation. For this model, the axial force is represented as

$$F_{axial} = \frac{1}{2}\rho\tilde{u}_o^2 A C_T \quad \text{.......} \quad (2.63)$$

where $\tilde{u}_o$ is the unperturbed resolved velocity of the axial incident flow acting on the center of the disk, A is the swept area of the rotor, and C_T is the thrust coefficient.

A rotational actuator disc model was employed as the second model (ADM-R). To compute the 2-D forces, this model employs the BEM technique outlined previously, which is integrated across the rotor disc. The ADM-R can model rotation as a result of this modification. It is unable to show the tip vortices, however, because they are integrated throughout the entire disc surface. The actuator line model (Sorensen and Shen, 2002) was the final model investigated. This model calculates turbine induced lift and drag forces using the BEM technique and distributes them uniformly throughout the actuator lines. The ALM can capture tip vortices and needs considerably fewer cells than resolving the real turbine blades since it employs lines rather than a disc. The major benefit of using actuator models is that the mesh size is decreased compared modelling the exact geometry of the wind turbine, resulting in lower computing expenses.

The actuator models were tested in a wind tunnel with a 0.15 m diameter wind turbine model and a log-law incident neutral ABL by Porté-Agel et al. (2011). Figure 2.8 shows how the ADM-R and ALM models closely match the measurements in the near and far wake areas. In the near-wake area, the ADM-NR model underestimates the velocity loss, but agrees well in the far wake region. The turbulence intensity findings were not as close. The ADM-R and ALM models were close to each other, but different from the wind tunnel data. The ADM-NR, on the other hand, consistently underestimated the turbulence intensity. In figure 2.8, x/D is the normalized distance in the wake, and z/D is the normalized distance from the ground.

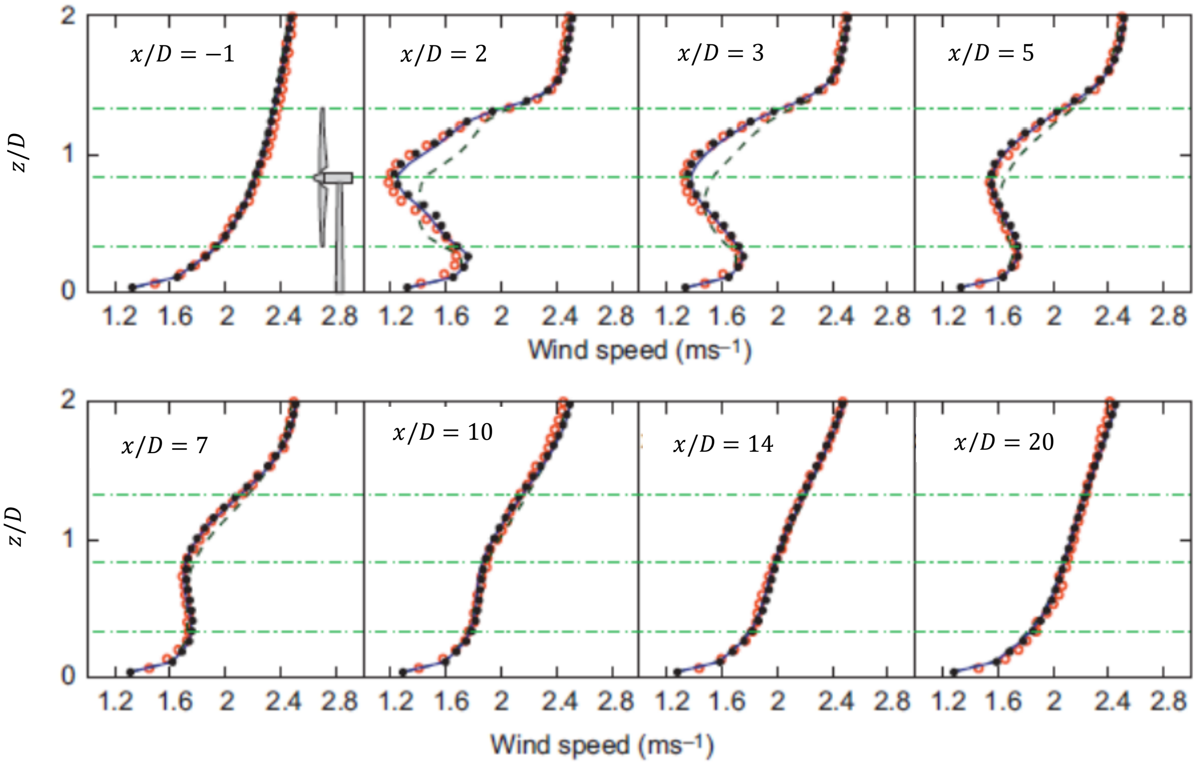

Figure 2.8. Stream wise velocity profiles (m/s): wind tunnel measurements (◦), ADM-NR (dashed line), ADM-R (solid line), ALM (black dots) (Porté-Agel, et al., 2011) "Reproduced with Permission of the Publisher/Owner, See Appendix B"

As wind turbines are getting larger, wind farms continue to grow in size. For this reason, understanding the wind farm effects on the ABL is important. Calaf et al. (2010) pointed out that wind farms might not have much effect on the large ABL, but they can affect the performance of the downstream wind turbines, lowering the performance of the wind farm as a whole.

According to Calaf et al. (2010), wind farm arrays larger than 10-20 km approach the infinite wind farm asymptotic limit, causing the boundary layer flow to be nearly fully developed. Calaf et al. (2010) used a LES model with a Smagorinsky SGS closure method to produce a parametric analysis of wind farms for their research. They created models of entire farms, changing the number of turbines and their spacing. The turbines were modelled as non-rotating actuator discs and a pressure driven neutral ABL was adopted (Calaf, et al., 2010).

When streamwise spacings of 7.85*D* and greater were employed in wind tunnel studies by Frandsen et al. (2006), considerable velocity recovery occurred prior to the succeeding turbine.

This was also reflected in the findings of Calaf et al. (2010)'s CFD study. Modelling single turbines has shown that the energy originates from the difference in kinetic energy flux across the turbine. Kinetic energy must be entrained from above for an array of turbines. This is due to the fact that the vertical kinetic energy fluxes are on the same scale as the power extracted (Frandsen et al., 2006). Turbine spacing only contributed around 10% increase in the overall power generation.

Wu et al. (2020) ran 20 wind farm simulation scenarios, with five different wind farm layouts and four different incoming ABL flow conditions. An aligned configuration, two lateral staggered arrangements, and two vertical staggered arrangements were considered, as shown in figure 2.9. Each wind farm had 120 turbines, which were arranged in 30 rows in the streamwise direction and four rows in the spanwise direction. The turbine hub heights in the AL and LS wind farms were 100 m, while those in the vertically staggered wind farms were 60 and 140 m.

To generate the incoming flow used later in the wind farm simulations, precursor simulations were ran for the ABL flow. The mean velocity ($\bar{u}$), streamwise turbulence intensity, and Reynolds stress ($u'w'$) profiles obtained from the precursor simulations are shown in figure 2.10. The log-law and the nondimensional velocity profiles align well. The turbulence strength was calculated as follows:

$$I = \frac{\sqrt{\frac{\sigma_u^2 + \sigma_v^2 + \sigma_w^2}{3}}}{\bar{u}_{hub}} \qquad (2.64)$$

where $\bar{u}_{hub}$= 9 m/s denotes the incoming mean velocity at the hub height, and $(\sigma_u^2, \sigma_v^2, \sigma_w^2)$ respectively, denote the velocity variance components in the streamwise, spanwise, and vertical directions, respectively.

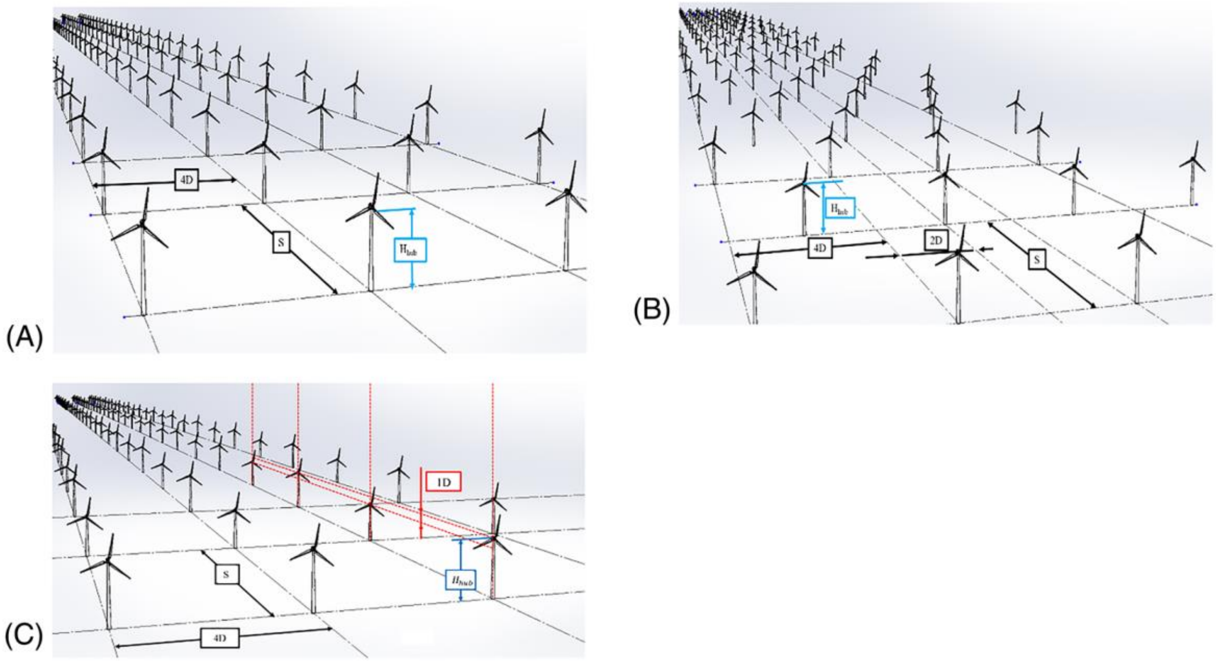

Figure 2.9. Schematic of (A) aligned layout, (B) laterally staggered layout, and (C) vertically staggered wind farm layouts; s is the separation distance (Wu et al., 2020) “Reproduced with Permission of the Publisher/Owner, See Appendix B”

The hub height velocity of 9 $^{m}/_{s}$ was chosen to systematically examine the impact of various incoming flow conditions and wind farm layouts on overall farm power output performance. For surface roughness heights of 0.5, 0.1, 0.01, and 0.0001 m, respectively, the corresponding friction velocity values were 0.60, 0.49, 0.37, and 0.26 $^{m}/_{s}$. The chosen four roughness lengths, $z_0 = 0.5$ m for bushes, $z_0 = 0.1$ m for farmland, $z_0 = 0.01$ m for grassland, and $z_0 = 0.0001$ m for snow-covered flats, are indicative of different surface types. A constant pressure-gradient was used to control the formation of the boundary layer flow with a depth of $\delta = 1000$ m.

Increases in surface roughness contribute to increases in the pressure gradient (used to drive the flow) and turbulence level for the four incoming flow conditions. This effect illustrates that a rougher surface dissipates more kinetic energy (due to higher surface friction) and allows greater entrainment to transfer more energy from above in order to maintain the hub height velocity $\bar{u}_{hub}$= 9 $^{m}/_{s}$, causing the momentum flux to be negative with larger magnitude for a rougher surface. These four inflow conditions were referred to as ABL11, ABL09, ABL07, and ABL05, based on the hub height turbulence levels of 11.1 %, 8.9 %, 6.8 %, and 4.9 % for roughness lengths of 0.5, 0.1, 0.01, and 0.0001 m, respectively. In addition, the vertically staggered configuration has two turbine hub heights of 140 and 60 m. At the high and low hub heights, the mean inflow streamwise velocities for ABL11 were 9.51 and 8.08 $^{m}/_{s}$, 9.40 and 8.28 $^{m}/_{s}$ for ABL09, 9.33 and 8.42 $^{m}/_{s}$ for ABL07, and 9.20 and 8.63 $^{m}/_{s}$ for ABL05.

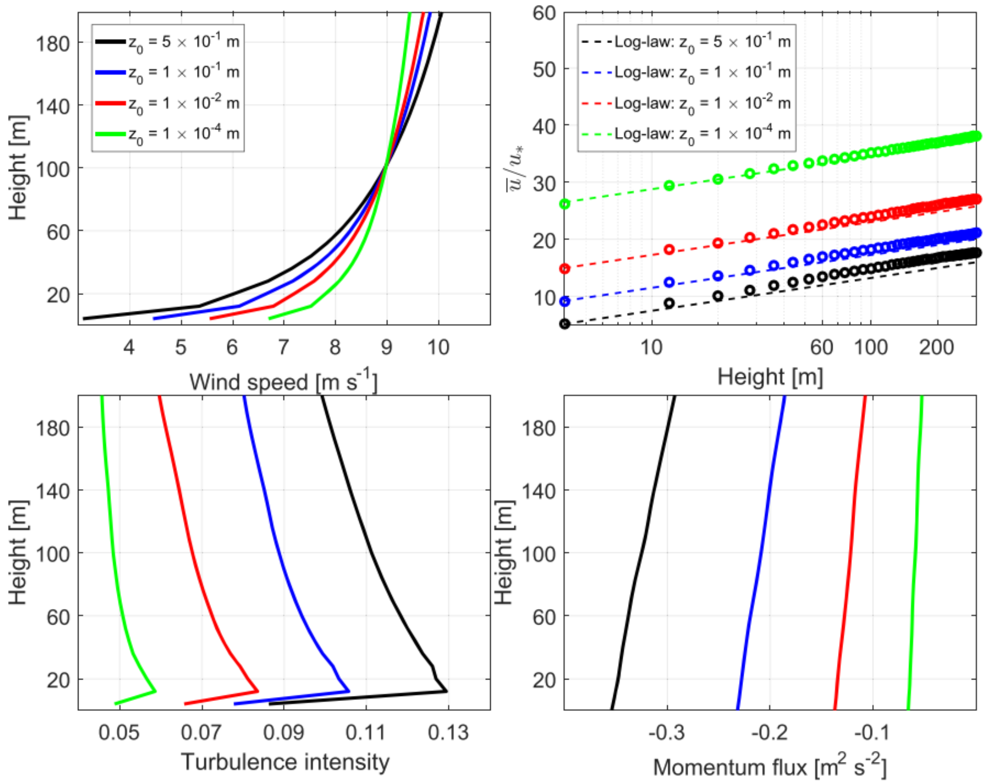

Figure 2.10. Profiles of incoming atmospheric boundary layer (ABL) flows developed over flat surfaces with roughness lengths of 0.5, 0.1, 0.01, and 0.0001 m: (A) mean streamwise velocity u ($^{m}/_{s}$), (B) normalised velocity versus vertical height in log scale, (C) overall turbulence stage, and (D) vertical momentum flux $\langle u'w' \rangle$($^{m^2}/_{s^2}$) (Wu et al., 2020) “Reproduced with Permission of the Publisher/Owner, See Appendix B”

Wu et al. (2020) results show that increasing the inflow turbulence level, rather than adjusting the turbine arrangement, will increase the overall power generation performance of wind farms. Based on the power outputs for the AL1 and LS1 wind farm layouts, an improvement in turbine configuration will only boost power generation performance on the turbines positioned in the first 10-turbine rows while increasing total farm power generation by approximately 9–13 %. Increased inflow turbulence, on the other hand, will effectively facilitate turbine wake recovery, minimize turbine-induced turbulence strength enhancement, and improve the power generation performance of downstream turbines exposed to upstream turbine wakes. The overall difference in average wind farm power output for the AL1, LS1, LS2, VS1, and VS2 layouts for the ABL11 and ABL05 inflow conditions was approximately 18.9%, 16.4%, 15.6 %, 12.7%, and 11.9%, respectively.

Meyers & Meneveau (2011) developed a formula for optimal turbine spacing based on the work of Calaf et al. (2010). Calaf's research predicted power production; the turbine cost ($cost_{\mathrm{t}}$), and land acquisition cost ($cost_{\mathrm{land}}$), were all taken into account in the analysis. The formula is defined as

$$\alpha = \frac{cost_{\mathrm{t}}/A}{cost_{\mathrm{land}}} \quad \ldots\ldots (2.65)$$

where α is the non-dimentionalised design constant, and A is the swept area of the rotor. It was found that for $\alpha = 1$, the optimal spacing is $4D$. However, for higher values of α (in the order of 10^4), where the land acquisition price is low, the optimum turbine spacing is $15D$.

The following chapter will focus on the ADM. Instead of modelling the rotor's exact geometry, since approximating it as a disc has significant computational advantages. Mesh resolution at the blade surface must be sufficient to capture the boundary layer and separation, as well as the development of the wake up to 30 turbine diameters (D) downstream, in order to create a complete model of the rotor. This requires a huge number of mesh elements and, as a result, a tremendous amount of computational work. With limited resources, extending this mesh to many devices in arrays of 10 or more turbines is not practical. Also, the actuator disc approximation can be used to solve a steady-state simulation. Modelling a rotating turbine needs the simulation to be unsteady and the blades to change position with each time step. The actuator disc approach is beneficial where large-scale flow effects, such as those seen in the installation of multi-turbine arrays, are of interest due to its limits and efficiency.

With such advantages of the ADM also comes some disadvantages. A wind turbine will extract energy from the flow, by reducing momentum. However, an experimental ADM will generate a small scale turbulence that will dissipate rapidly after the disc. This phenomenon is an artefact of the porous disc approach. This approximation will not replicate the vortices shed from a rotating turbine, neither in experiment nor a RANS simulation.

The assumption of the actuator disc will not generate any swirl in the flow. This is based on the idea that the flow will have similar structure after the near wake region, as the swirls and vortices would have dissipated. Wind turbine wakes are divided into two categories: near wake and far wake. The near wake region is concerned with a single turbine extracting energy from the wind, whereas the far wake is more concerned with the impact on downstream turbines and the environment (Marmidis et al., 2008). Near wake length has been debated, although it is generally thought to be between 1 and 5 rotor diameters ($1D$ to $5D$) downstream from the rotor disc, with far wake areas depending on terrain and environmental factors (Vermeer et al., 2003).

The steady AD/RANS methodology, does not account for the transient characteristics of the flow. It provides an understanding of the mean flow characteristics and the isotropic turbulence. If the object of interest is the vortices shed in the wake, a LES which fully resolves the geometry would be a better option.

Chapter 3. Numerical Study of Wind Turbine Wakes

This research will explore the velocity deficit and the turbulence quantities created by a wind turbine wake, through a suite of actuator disc Reynolds Averaged Navier-Stokes models. The simulations will be performed using ANSYS/FLUENT for a single turbine and two inline turbines under a uniform flow inlet conditions, and neutral atmospheric boundary conditions.

The objective of this study is to understand the effect of a wind turbine wake on subsequent turbines, and to test the effects of different turbulence closure models. All models were run on a four parallel processor system (Intel(R) Xeon(R) CPU E3-1230 V2, 3.30 GHz) with 32 GB of installed memory, to demonstrate the capabilities of AD/RANS models on modest computer systems.

The following section will present a theoretical overview of the numerical methods and models extracted from the literature review.

3.1 Theory

As mentioned earlier, the actuator disc model has the same circumference as a turbine rotor and approximates the forces it imparts on the surrounding flow. Modeling wind turbines has long relied on the actuator disc momentum principle (Burton, Jenkins, Sharpe, & Bossanyi, 2011). This model approximates the thrust force in one dimension and does not account for the rotation of the flow created by the blades (Tossas & Leonardi, 2013). There are significant computational savings to modelling the turbine as a disc rather than trying to resolve its complete geometry in a RANS simulation. A full rotor model would require sufficient mesh resolution at the blade surface to capture the boundary layer and any separation, as well as resolve the evolution of the wake up to twenty turbine diameters downstream. This would necessitate a huge number of grid points and, as a result, an enormous computational effort (Mason-Jones et al., 2008). With finite resources, it is not possible to extend this meshing to arrays of ten or more turbines. Furthermore, modelling a rotating turbine necessitates an unsteady model in which the blades change position with each time step, whereas the actuator disc approximation represents a steady-state simulation. In general, the actuator disc model is beneficial when large-scale flow effects, such as those seen during the installation of multi-turbine arrays, are of interest.

The three-dimensional, Reynolds-averaged equations for conservation of mass and momentum are solved for the whole domain, with a special treatment in the disc region (Harrison, Batten, Myers, & Bahaj, 2010). To implement the ADM, a mathematical formulation of the thrust force is needed. The thrust force was defined by equation (2.1) as the pressure difference multiplied by the disc area; the thrust coefficient becomes

$$C_T = \frac{T}{\frac{1}{2}\rho U_\infty^2 A_D} = \frac{\Delta P}{\frac{1}{2}\rho U_\infty^2} \quad (3.1)$$

where A_D is the surface area of the disc.

This implies the following expression for the pressure difference based on the thrust coefficient, velocity, and density:

$$\Delta P = \frac{1}{2}\rho U_\infty^2 C_T \quad (3.2)$$

The thrust coefficient presented in equation (3.2) is that of the rotating turbine. To implement the thrust in the momentum equation, the pressure difference is expressed as a difference in pressure across a disc of finite thickness Δx, where the thrust coefficient is defined per unit thickness,

$$\frac{\Delta P}{\Delta x} = \frac{1}{2}\rho U_\infty^2 \frac{C_T}{\Delta x} \quad (3.3)$$

In this model the inputs are the disc thickness and the thrust coefficient, which is sometimes referred to as the drag coefficient in the wind turbine literature (Helvig et al., 2021).

The thrust coefficient in equation (3.3) is that of the rotating wind turbine which will be matched to the actuator disc. A solid disc with the same diameter as the rotor would have a higher drag coefficient (approximately 1.1 for thin discs over a wide range of Reynolds number (Engineering ToolBox, 2004)).

After Betz (1920) determined the maximum output of a wind turbine using a representation of the rotor as a perfect disc (actuator disc), there was an increased interest in the aerodynamics of circular and perforated plates. Taylor (1963) introduced a theoretical relation (3.4) between the drag of a thin solid plate and a porous plate with the same dimensions and offering enough resistance to slow the wind passing through it. He then verified his theoretical results by measuring the drag coefficients of flat circular sheets of porous material dropped as parachutes in air and water (Taylor, 1963). Equation (3.4) presents a relation between the thrust (drag) coefficient and what is called the resistance coefficient (k), which is essentially the drag (thrust) coefficient of a porous plate analogous to the actuator disc. Taylor (1963) also introduced a relation (3.5) for the open area ratio θ (a measure of porosity) and the resistance coefficient.

$$C_T = \frac{k}{(1 + bk)^2} \quad (3.4)$$

$$\theta^2 = \frac{k}{1 + k} \quad (3.5)$$

In the equations above, $b = 0.25$ for wind/tidal turbine applications, and θ is the porosity of the plate. Whelan et al. (2007) investigated these relations by comparison to experiments and found that they produce reasonable results.

Usually in experiments involving an ADM, the disc is represented by a perforated circular disc (Medici, 2005; Sforza et al., 1981). While this can be done in CFD modelling, the mesh density near the disc can be problematic. To overcome this problem and in alignment with the previously mentioned formulation (equation 3.3), the disc region can be represented by a source term in the momentum equation that is only implemented for the grid points within the disc domain; the source term is given by

$$S_i = \frac{1}{2}\rho U_i^2 K \quad (3.6)$$

$$K = \frac{C_{T\,corrected}}{\Delta x} = \frac{k}{\Delta x} \quad (3.7)$$

where U_i is the velocity in the disc proximity, K is the corrected resistance coefficient, and $i = 0$ everywhere except in the streamwise direction ($i = 1$, for x only, no source term for y and z).

The regular RANS equations will be solved over the whole domain, except on the disc grid point, where the new source term will be added (3.9). So the mass and momentum equations in tensor notation will be as follows

Mass conservation

$$\frac{\partial U_i}{\partial x_i} = 0 \quad (3.8)$$

Momentum conservation

$$\frac{\partial(\rho U_i)}{\partial t_i} + \frac{\partial \rho(U_i U_j)}{\partial x_i} = -\frac{\partial P}{\partial x_i} + \rho g_i + \frac{\partial}{\partial x_j}\left[\mu\left(\frac{\partial U_i}{\partial x_j} + \frac{\partial U_j}{\partial x_i}\right)\right] - \frac{\partial}{\partial x_j}\left(\overline{\rho u_i' u_j'}\right) + S_i \quad (3.9)$$

where g_i is the gravitational force, μ is viscosity, S_i is the new source term added to the momentum equation, ρ is the density, and $\overline{u_i' u_j'}$ is the turbulent stresses.

Unlike the fully resolved unsteady modelling, the AD/RANS provides an inexpensive computational model for wind turbines wake analysis. It requires knowledge of the thrust and the diameter of the rotor. The fully resolved model requires many inputs, including the airfoil profiles, twist angle, angle of attack, pitch angle and rotational speed. For many commercial wind turbines, such information may not available from the manufacturer. So, the AD model provides a robust method for analyzing wind turbine wake structure.

While the above source term approach has been used in multiple studies (Johnson et al. 2014, Harrison et. al., 2010), presenting the external forces on an interface of zero thickness will remove the uncertainty with the definition of the disc thickness. This was employed by several other research papers (El Kasmi & Masson, 2008; Cao et. al., 2018).

In their approach the source term is defined as

$$S_i = \frac{1}{2}\rho U_i^2 k \quad (3.10)$$

Also, the resistance coefficient is that of the perforated plate in an experimental analysis. However, for numerical analysis, the resistance coefficient will overestimate the velocity deficit. So the final form of the source term used in a numerical domain is as follows

$$S_i = \frac{1}{2}\rho U_i^2 C_T \quad (3.11)$$

Given the nature of RANS, the Reynolds stresses represent additional unknowns creating a closure problem. For this reason, a progression of turbulence closures was considered, as described in the following section.

3.2 Turbulence Closure Models

3.2.1 Standard $k-\varepsilon$ Model

The $k-\varepsilon$ model (Launder and Spalding, 1974) is a two-equation turbulence closure model that solves for the turbulent kinetic energy k and the turbulent dissipation rate ε. It is one of the most popular models for general application. The model uses an isotropic eddy viscosity model (EVM) for the Reynolds stress tensor (equation 3.12)

$$-\langle u_i u_j \rangle = v_t \left(\frac{\partial U_i}{\partial x_j} + \frac{\partial U_j}{\partial x_i}\right) - \frac{2}{3}\delta_{ij}k \quad (3.12)$$

where v_t is the eddy viscosity, and δ_{ij} is the Kronecker delta.

The two transport equations as represented in ANSYS/FLUENT are:

$$\frac{\partial}{\partial t}(k) + \frac{\partial}{\partial x_i}(k u_i) = \frac{\partial}{\partial x_j}\left[\left(v + \frac{v_t}{\sigma_k}\right)\frac{\partial k}{\partial x_j}\right] + g_k + g_b - \varepsilon - y_m + S_K \quad (3.13)$$

$$\frac{\partial}{\partial t}(\varepsilon) + \frac{\partial}{\partial x_i}(\varepsilon u_i) = \frac{\partial}{\partial x_j}\left[\left(v + \frac{v_t}{\sigma_\varepsilon}\right)\frac{\partial \varepsilon}{\partial x_j}\right] + c_{1\varepsilon}\frac{\varepsilon}{k}(g_k + c_{3\varepsilon} g_b) - c_{2\varepsilon}\frac{\varepsilon^2}{k} + S_\varepsilon \quad (3.14)$$

They are then used to solve for the local eddy viscosity

$$v_t = c_u \frac{k^2}{\varepsilon} \quad (3.15)$$

In equations (3.13) and (3.14), g_k and g_b are the kinetic energy production terms due to the mean velocity gradient and buoyancy, and y_m is the contribution from the fluctuating dilatation in compressible turbulence to overall dissipation rate. The turbulent Prandtl numbers for k and ε are σ_k and σ_ε, respectively; $c_{1\varepsilon}$, $c_{2\varepsilon}$ and $c_{3\varepsilon}$ are constants; and S_K and S_ε are user-defined source terms.

While the standard $k-\varepsilon$ performs very well in a free shear layer (Menter, 1994), it lacks accuracy in flows involving adverse pressure gradients, separation, and strong curvature.

The main drawback in this model is the highly empirical dissipation rate. The model performance can be improved by modifying the dissipation rate transport equation. (Hanjalic et al., 1980).

3.2.2 $k - \varepsilon$ RNG Model

Renormalization group theory, a statistical approach, was used to create the $k - \varepsilon$ RNG model. It is founded on Kolmogorov's fundamental assumption of the universality of small scales in turbulence (Orszag et al., 1996). The eddy viscosity in the standard $k - \varepsilon$ model is estimated from a single turbulence length scale, therefore the calculated turbulent diffusion is only that which occurs at that scale, although in fact all scales of motion contribute to the turbulent diffusion. The RNG method, which is a mathematical strategy for deriving a turbulence model comparable to the $k - \varepsilon$ model, yields a modified form of the ε equation that seeks to account for varied scales of motion by changing the production term (Yakhot & Smith, 1992). The transport equations of k and ε in the $k - \varepsilon$ RNG model are

$$\frac{\partial}{\partial t}(k) + \frac{\partial}{\partial x_i}(k u_i) = \frac{\partial}{\partial x_j}\left[a_k \mu_{\text{eff}} \frac{\partial k}{\partial x_j}\right] + g_k + g_b - \varepsilon - y_m + S_K \ldots\ldots\ldots\ldots\ldots\ldots (3.16)$$

$$\frac{\partial}{\partial t}(\varepsilon) + \frac{\partial}{\partial x_i}(\varepsilon u_i) = \frac{\partial}{\partial x_j}\left[a_\varepsilon \mu_{\text{eff}} \frac{\partial \varepsilon}{\partial x_j}\right] + c_{1\varepsilon}\frac{\varepsilon}{k}(g_k + c_{3\varepsilon} g_b) - c_{2\varepsilon}\frac{\varepsilon^2}{k} - R_\varepsilon + S_\varepsilon \ldots\ldots (3.17)$$

where a_k and a_ε are the inverse effective Prandtl number for k and ε, respectively; and μ_{eff} is the effective viscosity.

It should be noted that the effective viscosity is calculated differently in near-wall regions to account for the effects of low Reynolds numbers. The turbulent viscosity of a high Reynolds number flow is estimated in the same way as for the standard $k - \varepsilon$ model. The most important difference between the RNG model and the standard model is an extra term in the ε equation that improves the responsiveness to quickly strained flow: R_ε is given by

$$R_\varepsilon = \frac{C_\mu \eta^3 (1 - \eta/\eta_o)}{1 + \beta \eta^3}\frac{\varepsilon^2}{k} \ldots\ldots\ldots\ldots\ldots\ldots\ldots\ldots\ldots\ldots (3.18)$$

$$\eta \equiv \frac{Sk}{\varepsilon} \ldots\ldots\ldots\ldots\ldots\ldots\ldots\ldots\ldots\ldots\ldots\ldots (3.19)$$

$$S = (2 S_{ij} S_{ij})^{1/2}$$

where $\eta_o = 4.38$ and $\beta = 0.012$

R_ε was not calculated using RNG theory and lacks a solid foundation (Pope, 2000). The $k - \varepsilon$ RNG model incorporates analytical formulations of the turbulent Prandtl numbers (ANSYS, 2020). These enhancements make $k - \varepsilon$ RNG more capable over a larger range of flows, but incorrect model tuning can cause near-wall effects to be poorly captured (ANSYS, 2020).

3.2.3 El Kasmi and Masson (2008)

Motivated by Chen and Kim (1987), El Kasmi and Masson (2008) presented a new method for simulating the flow around a wind turbine. In their model, a new term was added to the transport equation dissipation rate in the vicinity of the wind turbine. This term represents the energy transfer rate between scales of turbulence controlled by the production rate and the dissipation rate (El Kasmi & Masson, 2008).

The added term is

$$p_\varepsilon = c_{\varepsilon 4} \frac{{P_t}^2}{\rho k} \quad \text{(3.20)}$$

where P_t is the production of turbulent kinetic energy, and $c_{\varepsilon 4}$ is a new constant for the $k - \varepsilon$ model.

The new term was added in the region extending $0.25D$ upstream and downstream of the actuator disc, and within the actuator disc. This raises a question about the correct region to apply the new term, and the credibility of the method. One more issue with this method is the experimental constant $c_{\varepsilon 4}$. Prospathopoulos et al. (2011) showed that this constant is case specific and needs to be tuned. For their paper, El Kasmi and Masson (2008) used a value of 0.37 for $c_{\varepsilon 4}$, while the other constants where taken based on Crespo et al. (1985). The numerical results were in good agreement with the experimental results, however the authors were not explicit about the value of $c_{\varepsilon 4}$. Prospathopoulos et al. (2011) ran different cases based on different experiments, and the results for $c_{\varepsilon 4}$ varied from 3 or 4 for the first experiment, to as high as twenty for the second experiment. This indicates that the presented model of El Kasmi and Masson (2008) is not robust and needs some further development.

3.2.4 $k - \omega$ Model

Saffman (1970) formulated the $k - \omega$ model after which Spalding (1972), Wilcox (1988) and others further improved the $k - \omega$ model. The term ω (specific dissipation rate or turbulent frequency) is defined as the ratio of ε to k, therefore, ω is the rate of dissipation per unit turbulence kinetic energy. The formulation of the transport equation for ω has changed as the model evolved. The following formulation is based on Wilcox (1988).

The eddy viscosity is given by

$$\mu_t = \frac{\rho k}{\omega} \qquad (3.21)$$

The transport equation for the turbulent kinetic energy is

$$\rho \frac{\partial}{\partial t}(k) + \rho U_j \frac{\partial}{\partial x_i}(k) = \frac{\partial}{\partial x_j}\left[(\mu + \sigma^* \mu_t)\frac{\partial k}{\partial x_j}\right] + \tau_{ij}\frac{\partial U_i}{\partial x_j} - \beta^* \rho k \omega \qquad (3.22)$$

Specific dissipation rate

$$\rho \frac{\partial \omega}{\partial t} + \rho U_j \frac{\partial \omega}{\partial xj} = \frac{\partial}{\partial xj}\left[(\mu + \sigma \mu_t)\frac{\partial \omega}{\partial xj}\right] + \alpha \frac{\omega}{k}\tau_{ij}\frac{\partial U_i}{\partial x_j} - \beta \rho \omega^2 \qquad (3.23)$$

where σ^* and σ are coefficients that damp the turbulent viscosity, τ_{ij} is the favre-averaged specific Reynolds-stress tensor, and β^* and β are closure coefficients.

Both the $k - \varepsilon$ and $k - \omega$ models are eddy viscosity models and use a similar constitutive relation (gradient diffusion) to calculate the eddy viscosity which is based on a single turbulence length scale. The k equation is exactly the same for both models. It contains diffusion, production and dissipation terms on the RHS. The terms in the ε and ω equations are also the same, however, since $\omega = \varepsilon / k$, each term has an extra k in its denominator in the ω equation.

The $k - \omega$ model performs significantly better under an adverse pressure gradient condition than the $k - \varepsilon$ model and shows potential for predicting transition. It also allows a more accurate near wall treatment. The $k - \omega$ model does not employ damping functions and has straightforward boundary condition.

3.2.5 $k - \omega$ SST and Cao et al. (2018) Observations

The $k - \omega$ shear stress transport (SST) turbulence model, is a popular and reliable two-equation eddy-viscosity turbulence model. The model incorporates the $k - \omega$ and $k - \varepsilon$ turbulence models, with the $k - \omega$ being used in the inner region near the wall and the $k - \varepsilon$ being used in the free shear flow region. Menter (1994) developed the SST two-equation turbulence model to address the $k - \omega$ freestream sensitivity and improve the performance in adverse pressure gradients. The SST model is based on both physical experiments and simulations. The two calculated variables are generally interpreted as follows: k is the turbulence kinetic energy and ω is the rate of dissipation of eddies.

The SST model is based on the standard $k - \omega$ model, where the k-equation is the same, but the ω equation and the eddy viscosity model are modified as follows to account for the transport of the principal turbulent shear stress

$$\frac{\partial(\rho\omega)}{\partial t} + \frac{\partial(\rho u_j \omega)}{\partial x_j} = \frac{\gamma}{\upsilon_t} P - \beta\rho\omega^2 + \frac{\partial}{\partial x_j}\left[(\mu + \sigma\mu_T)\frac{\partial\omega}{\partial x_j}\right] + 2(1 - F_1)\frac{\rho\sigma_2}{\omega}\frac{\partial k}{\partial x_j}\frac{\partial\omega}{\partial x_j} \; \ldots\ldots (3.24)$$

$$\upsilon_t = \frac{a_1 k}{max(a_1\omega, \Omega F)} \; \ldots\ldots (3.25)$$

where γ is a tuning constant, and F_1 and F are blending functions.

Comparing equation (3.23) with equation (3.24), it can be seen that the main difference is the presence of the last term in the new equation. Combining the strengths of the $k - \varepsilon$ and $k - \omega$ models, the SST model gives accurate prediction of the onset and amount of flow separation under adverse pressure gradients. It is also capable of simulating boundary layers with reasonable accuracy.

Cao et al. (2018) suggested a modification for the $k - \omega$ SST model. The re-formulation contained two parts, a change in the model constants and a new source term to maintain turbulence level. The first part is based on Prospathopoulos et al. (2011) where all the constants remain the same as Menter (1994) prescribed them except for the following

$$\beta = 0.033,\ \beta^* = 0.025 \text{ and } \gamma = 0.37 \text{ for the inner region}$$

The second part is based on the free decay of the turbulence intensity. As pointed out by Cao et al. (2018), in the free-stream flow, the mean velocity gradient is zero so that the turbulence quantities decay. Therefore, the production terms and the diffusion terms can be neglected. To maintain the turbulence quantities defined at the inlet without unphysical decay, the new model has source terms added to the k and ω equations

$$\rho \frac{\partial}{\partial t}(k) + \rho U_j \frac{\partial}{\partial x_i}(k) = \frac{\partial}{\partial x_j}\left[(\mu + \sigma^* \mu_t)\frac{\partial k}{\partial x_j}\right] + \tau_{ij}\frac{\partial U_i}{\partial x_j} - \beta^* \rho k \omega + \beta^* \rho k_{amb} \omega_{amb} \ldots\ldots\ldots\ldots (3.26)$$

$$\frac{\partial(\rho\omega)}{\partial t} + \frac{\partial(\rho u_j \omega)}{\partial x_j} = \frac{\gamma}{\upsilon_t} P + \frac{\partial}{\partial x_j}\left[(\mu + \sigma \mu_T)\frac{\partial \omega}{\partial x_j}\right] + 2(1 - F_1)\frac{\rho \sigma_2}{\omega}\frac{\partial k}{\partial x_j}\frac{\partial \omega}{\partial x_j} - \beta \rho \omega^2 + \beta \rho {\omega_{amb}}^2 \ldots\ldots\ldots\ldots (3.27)$$

The subscript "amb" refers to ambient.

The destruction terms can be cancelled if the inflow values of k and ω are set equal to the ambient values, which means in the free-stream flow case, turbulence quantities will remain unchanged throughout the computational domain. This modification was inspired by the experimental and numerical work of Spalart and Rumsey (2007). Table 3.1 summarizes the different turbulence closure models used.

Table 3.1: Summary of turbulence closure models

Turbulence Model	Author(s)	Comments
Standard $k - \varepsilon$ model	Launder and Spalding (1974)	Eddy viscosity model
$k - \varepsilon$ RNG	Yakhot and Smith (1992)	Modified ε equation in attempt to account for the different scales of motion through changes to the production term
$k - \varepsilon$ model with extra source term for the dissipation transport equations	El Kasmi and Masson (2008)	El Kasmi and Masson (2008) claimed the existence of a region of non-equilibrium turbulence close to the turbine. So the added

		source term was applied only in the proximity of the disc
$k-\omega$ model	Wilcox (1993)	Superior performance for complex boundary layer flows
SST $k-\omega$ model	Menter (1994)	Best prediction of flow separation. Suitable for adverse pressure gradient applications
SST $k-\omega$ model with extra source terms for the turbulence kinetic energy and dissipation transport equations	Cao et al. (2018)	Cao et al. (2018) suggested that the free decay of turbulence intensity cannot be avoided with the current set of RANS equations. So, additional source terms are needed

3.3 Model Description

The simulations in this chapter investigate the ability of the proposed AD/RANS model to predict the velocity and turbulence quantities in the wake. The simulations are based on three experimental studies. The first experiment is a Nibe 630-kW wind turbine with a 40-m diameter located at a 45 m hub height (Taylor et al., 1985). The second experiment is a Danwin 180-kW wind turbine with a 23 m diameter located at a 31 m hub height (Magnusson and Smedman, 1999). The third experiment is a Sexbierum 310-kW wind turbine with a 30 m diameter located at 35 m hub height (Cleijne, 1993). For the Nibe experiment, the velocity deficit and turbulence intensity within the wake under a variety of operating conditions up to 7.5 rotor diameters downstream of the turbine, the spectral characteristics of the turbulence in the wake, the power losses experienced by the rotor when operating in the wake, and the dynamic loads imposed on a rotor when operating in the wake, were collected. The rates of fatigue damage and external stresses caused by running a turbine in the wake zone were also investigated. For the Danwin experiment, the velocity deficit and turbulence intensity were measured in the wake, as well as the thrust coefficient for different inflow conditions. Finally, horizontal and vertical profiles of the U, V, and W components of the velocity in the wake, turbulence intensities in three directions and turbulent kinetic energy in the wake, and shear stresses $\langle u'v' \rangle$, $\langle u'w' \rangle$, and $\langle v'w' \rangle$ in the wake were all included in the Sexbierum experiment analysis. The data contained in this research were chosen for their relevance to the present study as well as their availability in the literature. Table 3.2 summarizes the location and type of terrain for each experiment. The Nibe experiment studies an inland area with a flat terrain, the Danwind experiments studies a coastal area with a rougher terrain, and the Sexbierum experiment studies an inland area that is rather close to the shore, with a flat homogeneous terrain.

Table 3.2: Summary of experiments

Experiment	**Location**	**Terrain**	**Method**
Nibe (Taylor et al., 1985)	Northern Denmark	Level terrain	Field Study
Danwin (Magnusson and Smedman, 1999)	Gotland Island in Sweden	Flat coastal strip with some grazed grass and low herbs	Field Study
Sexbierum (Cleijne, 1993)	Northern part of the Netherlands	Flat homogeneous terrain, 4 km from the seashore	Field Study

These three experiments are chosen to study the effect of different terrain on the velocity deficit in the wake of a wind turbine. In a CFD study, the terrain is set by surface roughness value. In this study, the first case discussed is the wake of single and tandem turbines under constant inlet boundary conditions. The second case is the neutral ABL inlet condition of Panofsky and Dutton (1984) for the velocity, turbulence kinetic energy and dissipation.

The turbulent viscosity is given by

$$v_t(z) = Ku^* z \quad (3.28)$$

where z is the vertical height above the ground, K is the von Karman constant, and u^* is the friction velocity. The friction velocity is given by

$$u^* = \sqrt{\frac{\tau_0}{\rho}} \quad \text{(3.29)}$$

where τ_0 is the surface shear stress. A logarithmic velocity profile is adopted as follows

$$u_0(z) = \frac{u^*}{K} \ln\left(\frac{z}{z_0}\right) \quad \text{(3.30)}$$

where z_0 is the roughness length of the terrain.

Assuming equilibrium between production and dissipation, and a constant stress layer the equations for the dissipation and turbulence kinetic energy become

$$\varepsilon_0(z) = \frac{{u^*}^3}{Kz} \quad \text{(3.31)}$$

$$k_0(z) = \sqrt{\frac{v_{t0}\varepsilon_0}{C_\mu}} \quad \text{(3.32)}$$

where C_μ is a constant.

The geometry and the domain of the experiment were created in ANSYS SpaceClaim according to the specifications of El Kasmi and Masson (2008) for the Nibe experiment, Magnusson and Smedman (1999) for the Danwin experiment, and Cleijne (1993) for the Sexbierum experiment. The 3*D* domain (Figure 3.1) is cylindrical: the turbine is located 5*D* from the inlet, the outlet is located 20*D* from the turbine, and the outer edge of the domain is located 5*D* from the center of the turbine. The outer domain is far enough from the main flow, so that the effects of the walls velocity gradient can be neglected, also the simulations are trying to mimic a wind tunnel in external flow analysis. So the assumption of a slip wall (zero shear stress) is an acceptable one.

Meshing was performed with ANSYS Meshing using a structured hexahedral mesh. Cell sizes were set to 1 m on the surface of the disc. The grid was implemented on the disc with a maximum growth rate of 1.05. The mesh size for all 3*D* experiments was approximately 600,000 elements. A grid independence study was performed using the axial induction factor, which is a measure of the velocity at the rotor. Grid elements were reduced by half their original size until a change of less than 1% was obtained in the axial induction factor. An example of the mesh and a grid independence study can be found in Appendix A.

The actuator disc was implemented as a $2D$ interface in the domain, using the source term approach discussed earlier. The turbulence quantities and inlet velocity were calculated using the ABL equations of Panofsky and Dutton (1984) evaluated at the hub height of the turbine. An ABL simulation was performed in this research; the result shows similar velocity value on the perimeter of the rotor. So the assumption of a constant velocity inlet and turbulence kinetic energy based on Panofsky and Dutton (1988) ABL equations is valid.

All steady state CFD models were run in ANSYS FLUENT V20.0. The inlet is set to uniform velocity inlet, the outlet is an outflow (Patankar, 1980), and the walls are zero shear walls. Figure 3.1 gives a sketch of the computational domain, where the single and tandem turbines are studied within a similar domain.

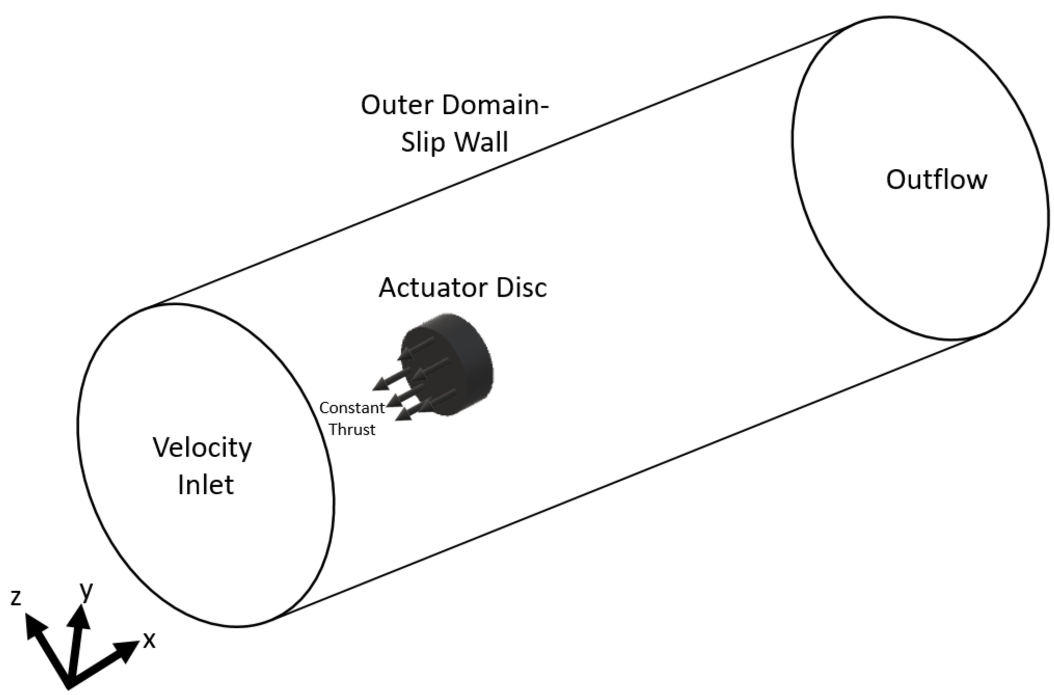

Figure 3.1: A sketch of the computational domain

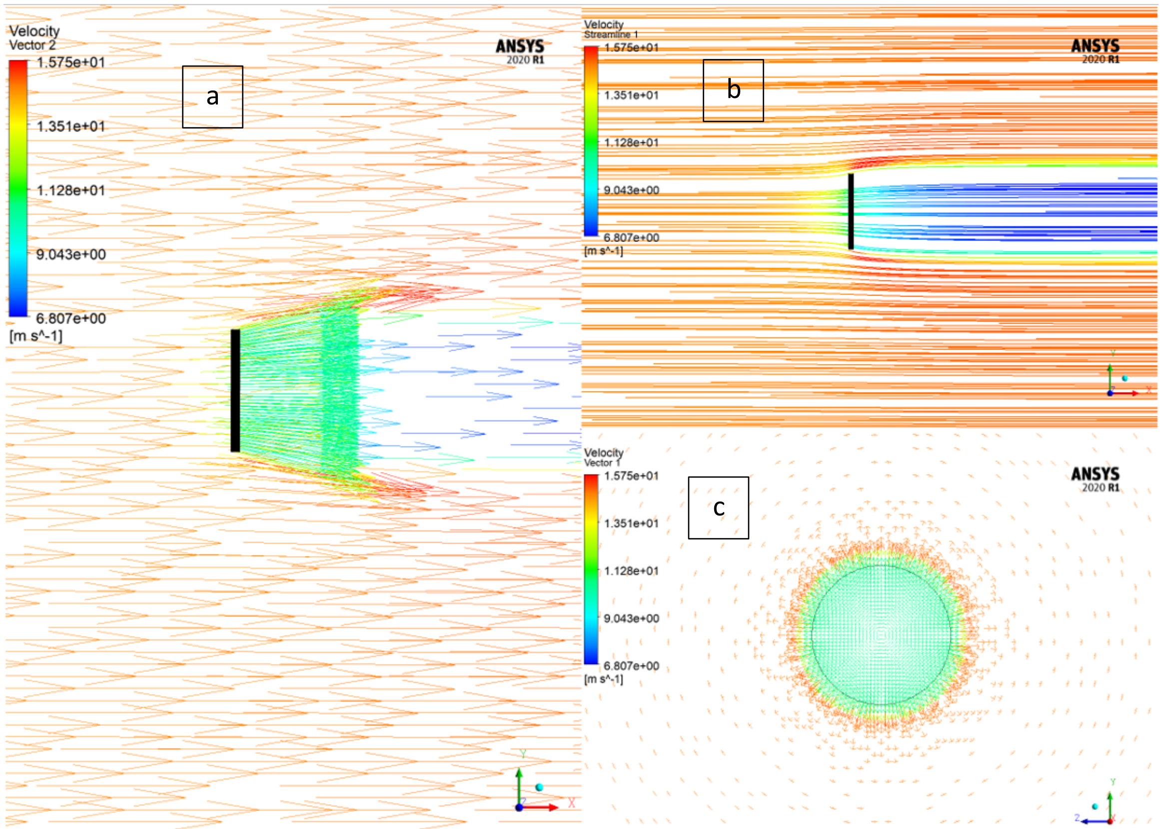

Figure 3.2. Velocity vectors and streamlines for flow over the actuator disc; a: velocity vectors on the cross-section of the domain; b: velocity streamlines on the cross-section of the domain; c: a: velocity vector on the lateral cross-section of the domain

The velocity vectors for the flow over an actuator disc are shown in Figure 3.2. The streamwise velocity vectors decrease on the inner area of the disc, and increase near the disc perimeter. The accelerated flow reflects the portion of the flow that has been deflected by the actuator disc. A source term is used to approximate a porous disc.

3.4 Results

The results of the simulations show good agreement between all the turbulence closure models for the velocity prediction. However, the prediction for turbulence quantities vary. The major enhancement in turbulence quantities is mainly associated with the model described by Cao et al. (2018). All models provided a fairly good agreement for the far wake velocity predictions, but, the turbulence intensity results from Cao et al. (2018) agrees better with the experimental results than the rest of the models.

This section will first introduce the wake similarity analysis, then the results for the standalone wind turbine, then two turbines in tandem, and finally the results under a neutral ABL conditions.

3.4.1 Wake Similarity

The velocity profile for a free shear layer can be expressed in a self-similar form. For an axisymmetric wake (Pope, 2000), as is the case of the constant inlet AD/RANS model, two parameters used to study the self-similarity are the maximum velocity deficit (ΔV_{max}) and the half-width ($r_{1/2}$). The half-width is, by definition, the distance from the wake centerline to the location where the velocity deficit has increased to one-half that at the centerline. For a self-similar wake the spread rate is constant with downstream distance:

$$S = \frac{V_o}{\Delta V_{max}} \frac{dr_{1/2}}{dx} \quad (3.33)$$

Previous analysis (Pope, 2000) shows the relation $\Delta U_{max} \sim x^{-2/3}$ and $r_{1/2} \sim x^{1/3}$. The wakes generated from different blunt bodies exhibit different spread rates. The spread rates for a flat plate, circular cylinder and airfoil are 0.073, 0.083 and 0.103, respectively (Pope, 2000). Figure 3.3 shows the velocity deficit at different downstream locations. Figure 3.4 shows the spatial development of the half-width which approaches the asymptotic dependence on $x^{1/3}$. For $x/D > 10$, the corresponding relations are

$$\frac{\Delta V_{max}}{V_o} = 0.542\left(\frac{x}{D}\right)^{-0.364} \quad (3.34)$$

$$\frac{r_{1/2}}{R} = 0.685\left(\frac{x}{D}\right)^{0.193} \quad (3.35)$$

The average spread rate for the far wake region is approximately 0.065, which is lower than the values for other blunt bodies.

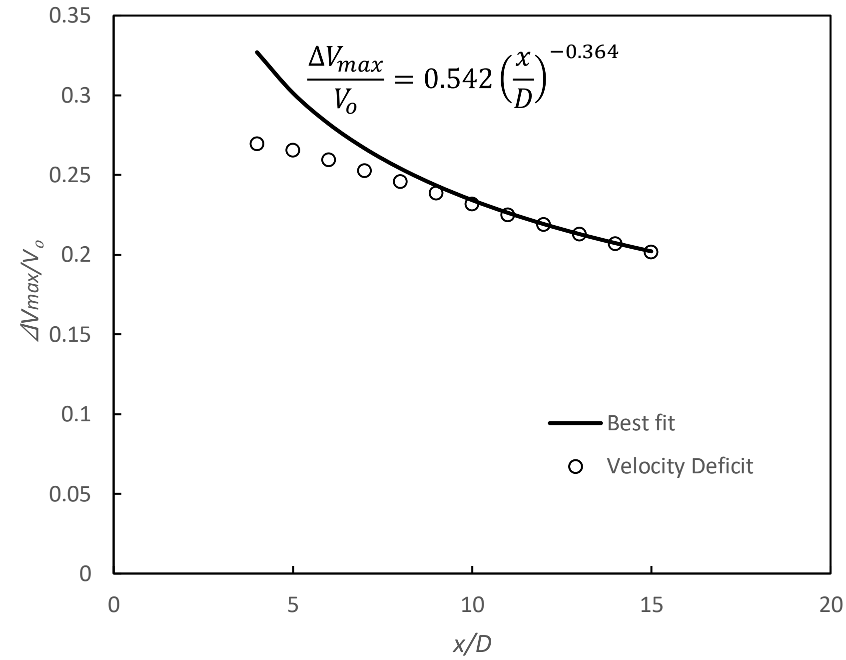

Figure 3.3. Velocity deficit of self-similar wake profiles

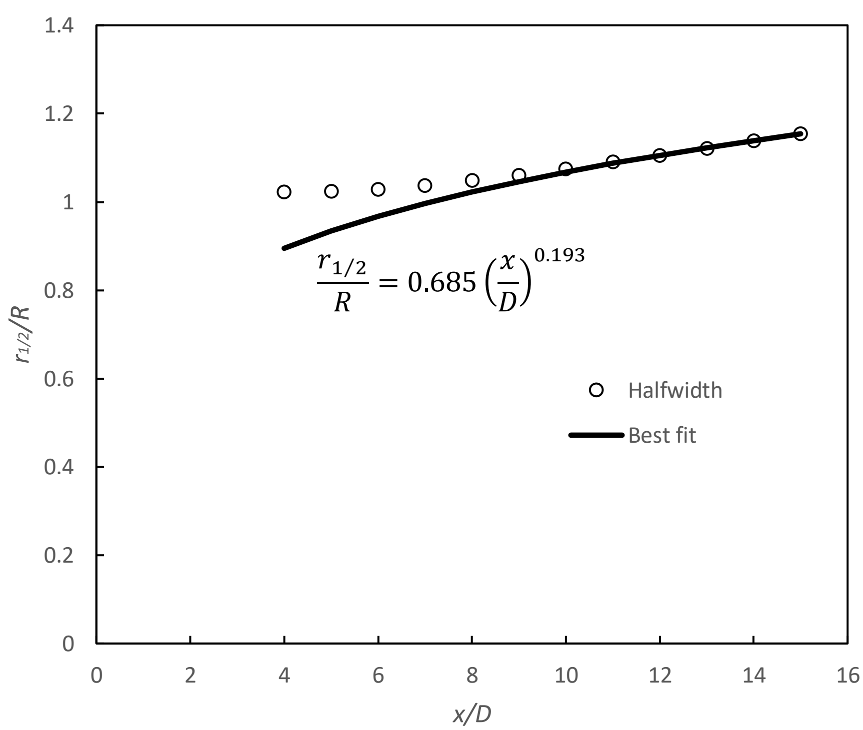

Figure 3.4. Half-width of self-similar wake profiles

Figure 3.5 shows the turbulence kinetic energy profile at the centerline of the rotor for different locations in the wake. For the far wake region, the rate of recovery of turbulence kinetic energy is observed to be

$$k = 1.388(\frac{x}{D})^{-0.143} \quad (3.36)$$

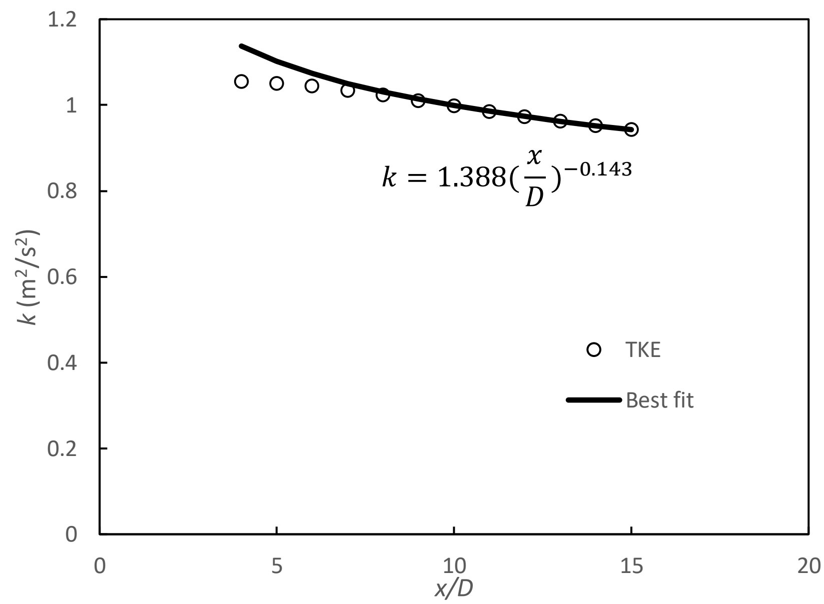

Figure 3.5. Turbulence kinetic energy of self-similar wake profiles

Based on these figures, a self-similar wake is achieved at around 10*D* downstream, and the best fit curves are those of the self-similar region.

3.4.2 Uniform Inlet Flow

3.4.2.1 Standalone Wind Turbine

Figures 3.6, 3.7 and 3.8 show the velocity profile in the wake of the Nibe wind turbine, for different inlet conditions. The agreement appears to happen at the beginning of the far wake region. The definition of the far wake region is ambiguous. However, in most cases, the far wake will start around 5*D* downstream (Sanderse, 2009). The reason behind the disagreement in the near wake region is the effect of the blade geometry. This problem in the near wake was stipulated and accepted based on the reasoning of rotor geometry effect (Van Kuik et al., 2008). For velocity deficit measurements, the different turbulence closure models behaved similarly, so the six models were represented by a single curve to avoid confusion. The significance of using different turbulence closure models will appear in the turbulence intensity results.

Turbulence intensity is shown in figures 3.9 and 3.10 for the centerline decay and a half rotor decay at 2.5D respectively. The figures show that the turbulence closure model used (Cao et al., 2018) shows a better agreement than El Kasmi and Masson (2008), however the general profile of the graphs show that the El Kasmi and Masson (2008) method is able to approximately capture the peak in TI. So, the El Kasmi and Masson method could be useful, but the used parameters need to be adjusted.

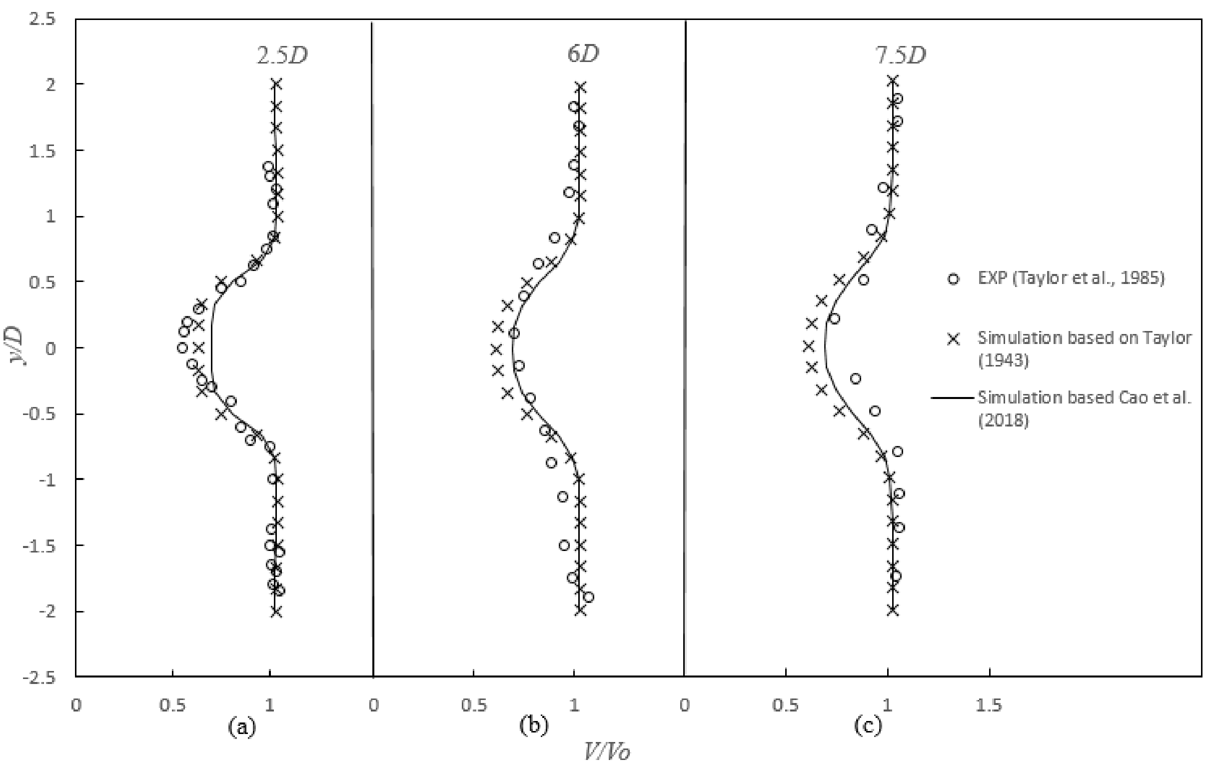

Figure 3.6. Nibe experiment: Wake velocity profile for $V_o = 11.52\ ^{\mathrm{m}}/_{\mathrm{s}}$, $C_T = 0.67$ and $TI =$ 10.5% at: (a): $x/D = 2.5$, (b): $x/D = 6$, (c): $x/D = 7.5$.

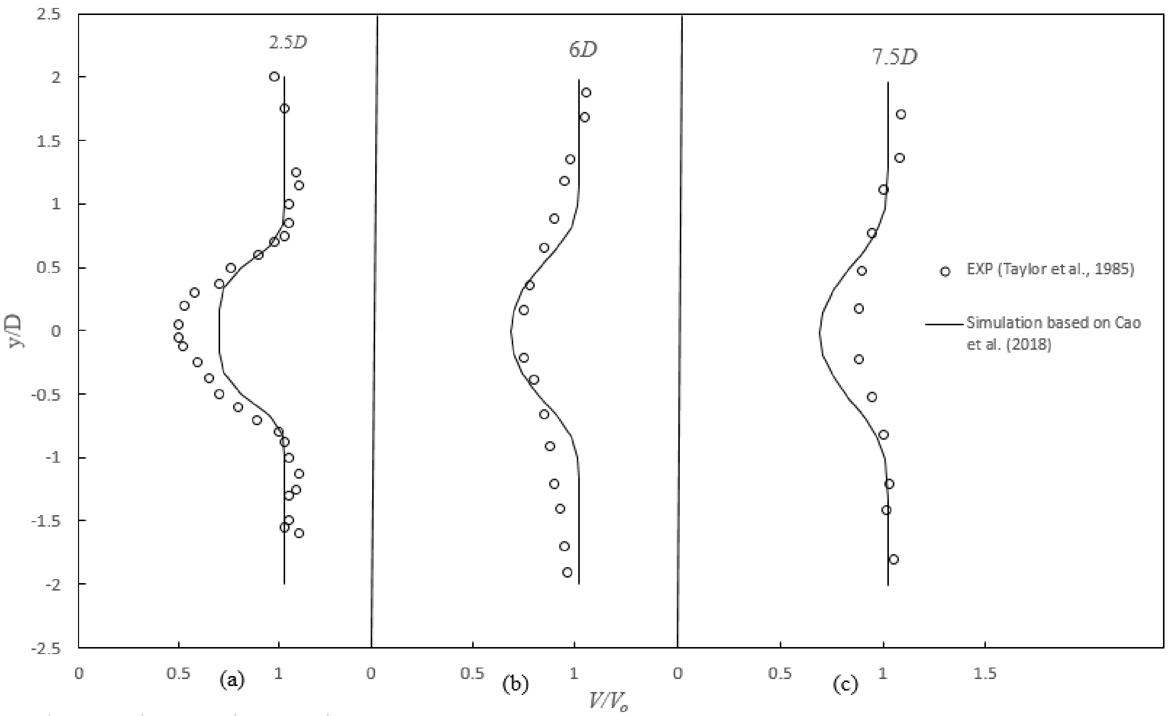

Figure 3.7. Nibe experiment: Wake velocity profile for $V_o = 9.56\ ^{\mathrm{m}}/_{\mathrm{s}}$, $C_T = 0.77$ and $TI = 11\%$ at: (a): $x/D = 2.5$, (b): $x/D = 6$, (c): $x/D = 7.5$

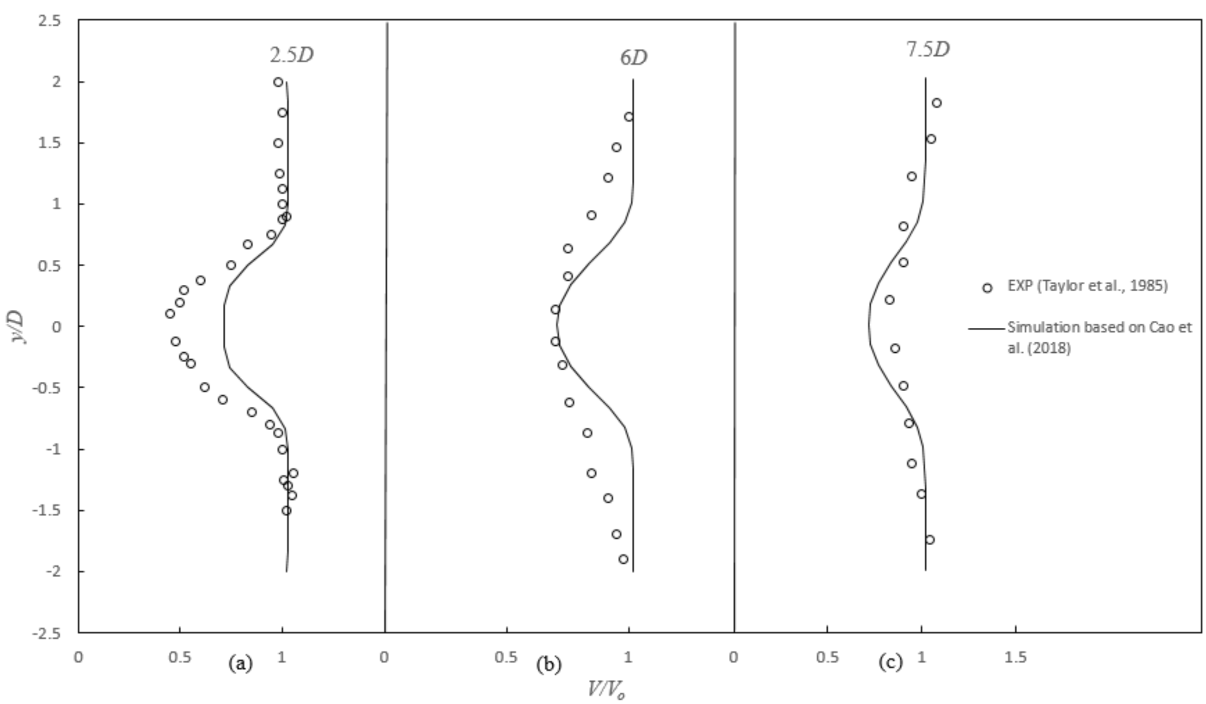

Figure 3.8. Nibe experiment: Wake velocity profile for $V_o = 8.5\ ^{\mathrm{m}}/_{\mathrm{s}}$, $C_T = 0.82$ and $TI = 11\%$ at: (a): $x/D = 2.5$, (b): $x/D = 6$, (c): $x/D = 7.5$

Figure 3.6 shows that the resistance coefficient (Taylor, 1943), explained in the previous chapter, indeed overestimates the velocity deficit in the wake. The resistance coefficient was introduced by Taylor (1943) for the experimental actuator disc model, however numerically as shown in figure 3.6, it gives erroneous results. However, the resistance coefficient in fact underestimates the maximum velocity deficit in the wake, but it captures the spread rate more accurately.

Figure 3.7 shows that the maximum velocity deficit is underestimated at 7.5*D*, while the results are better for 6*D*. However the spread rate at 7.5*D* agrees better with experimental data than that at 6*D*. Again after 2.5*D* the velocity deficit is far from the experimental data. For figure 3.8, a similar result as figure 3.7 is achieved.

Figure 3.6, 3.7 and 3.8 shows that for different thrust coefficient and inlet conditions, similar results are obtained for different downstream locations.

Figure 3.9 shows the turbulence intensity at the centerline of the domain downstream of the turbine. All turbulence closure models show good agreement with the experimental data, except for the El Kasmi and Masson (2008) model. The idea of adding an extra source term to the dissipation rate equation to transfer energy from large scales to small scales was not thoroughly justified. The inaccurate results shown in their paper based on the $k - \varepsilon$ model, may have arisen from the abrupt change of constants, following Crespo et al. (1985) analysis.

Figure 3.10 shows the turbulence intensity profile for one half of the rotor at 2.5*D* from the rotor. A better agreement is seen for the Cao et al. (2018) model than El Kasmi and Masson (2008). The peak turbulence intensity at 0.4*D* from the center of the rotor is underpredicted by the AD/RANS model. This relates to the nature of the model used. The constant value of the source term over the whole disc resulted in a uniform value of the TI for most of the wake. Figure 3.10 is the results of TI in the near wake region, so the turbulence quantities from the modeled experiment were expected to vary from the actual experiment.

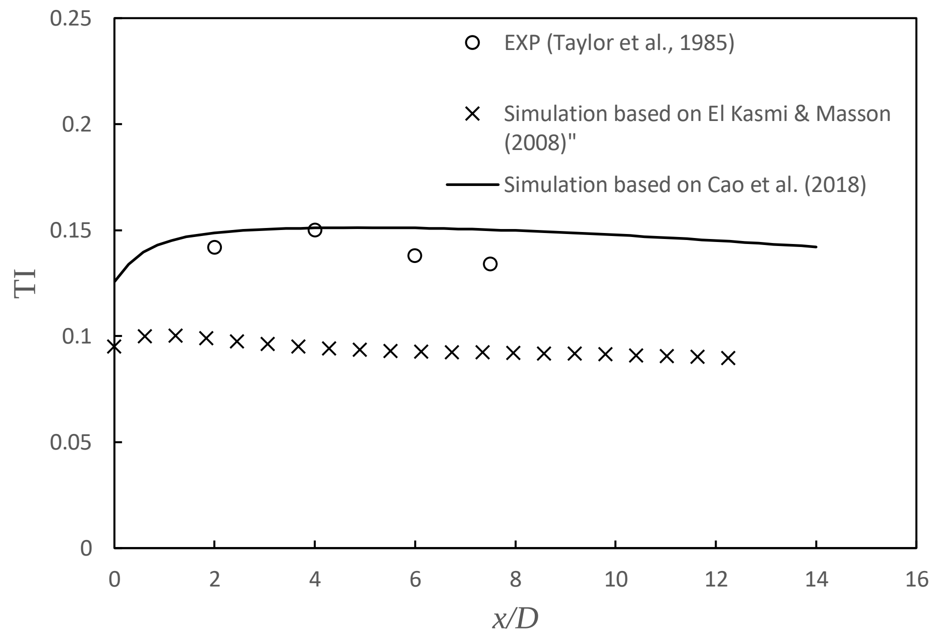

Figure 3.9. Nibe experiment: Decay of wake axial turbulence intensity decay for $V_o = 8.5\ ^{\mathrm{m}}/_{\mathrm{s}}, C_T = 0.82$ and $TI = 11\%$

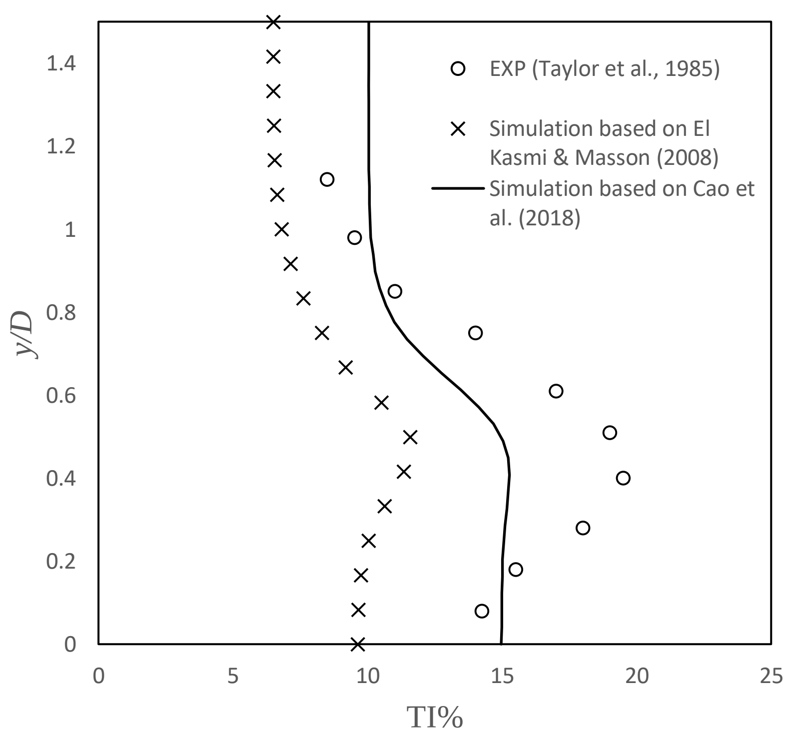

Figure 3.10. Nibe experiment: Wake distribution of turbulence intensity at $x = 2.5D$ for $V_o = 8.5\ ^{\mathrm{m}}/_{\mathrm{s}}, C_T = 0.82$ and $TI = 11\%$

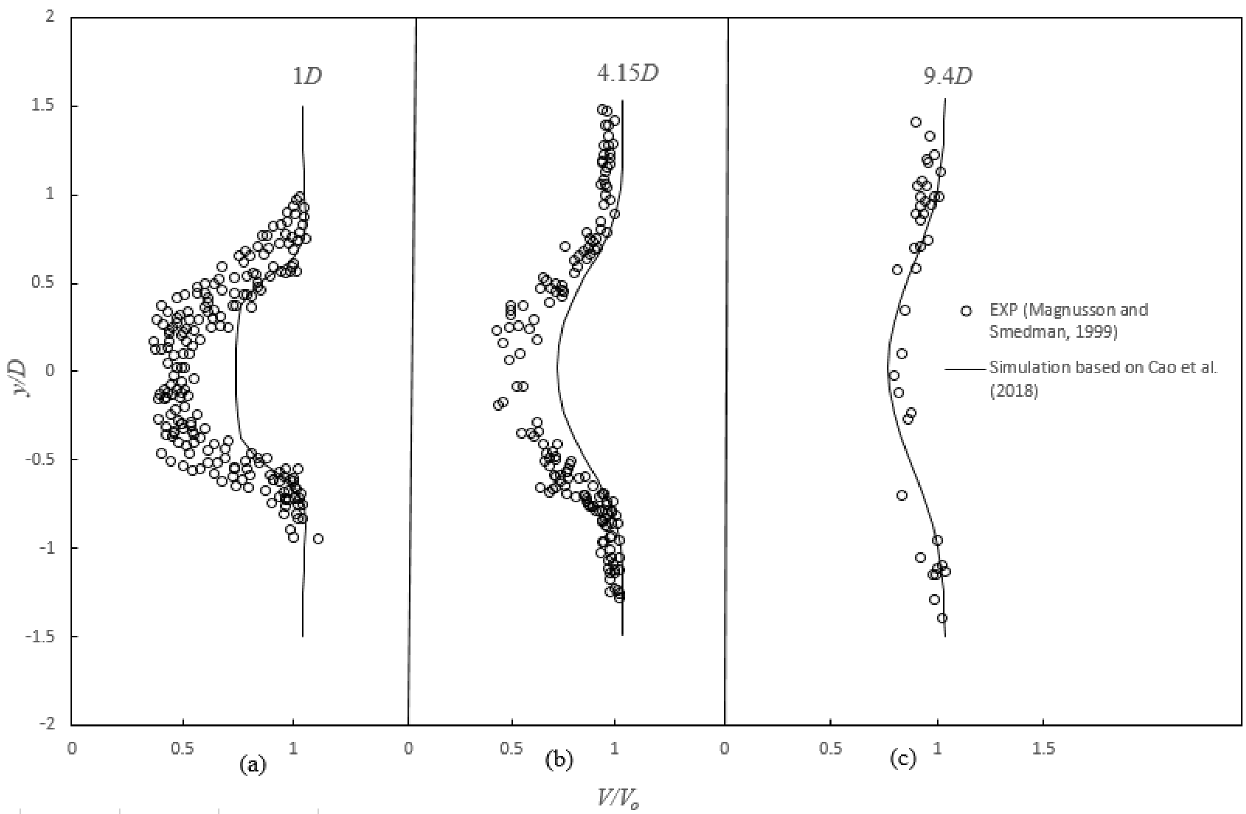

Figure 3.11. Danwin experiment: Wake velocity profile for several downstream locations for $V_o = 8\ ^{\mathrm{m}}/_{\mathrm{s}}$, $C_T = 0.82$ and $TI = 7\%$ at: (a): $x/D = 1$, (b): $x/D = 4.15$, (c): $x/D = 9.4$

The Danwind and Sexbierum experiments have a larger experimental data set than the Nibe experiments. Figure 3.11 shows a promising result in predicting the velocity deficit in the far wake region. At 9.4*D* downstream of the rotor, the result of the simulation match the experimental data more closely than for the Nibe experiment. At 1*D*, which is close to the rotor, the results do not agree with the experimental data. Figure 3.12 shows that the spread was not captured exactly in the wake.

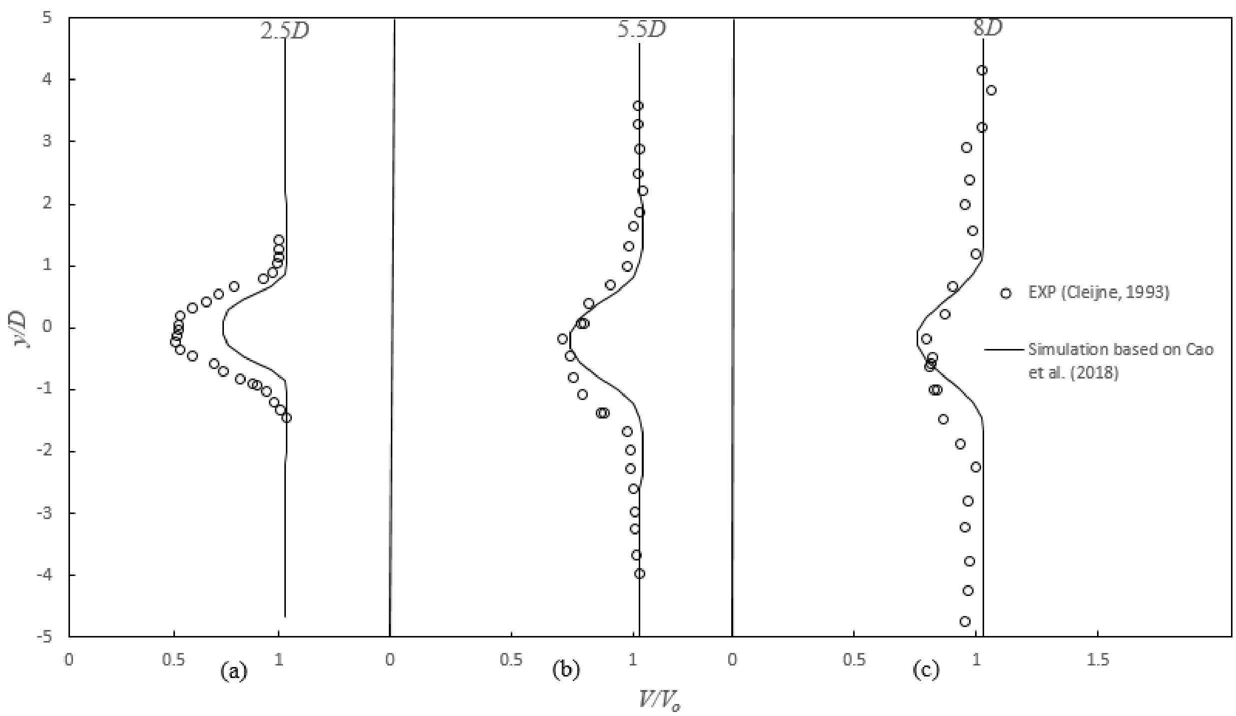

Figure 3.12. Sexbierum experiment: Wake velocity profile for $V_o = 8.5\ ^{\mathrm{m}}/_{\mathrm{s}}$, $C_T = 0.75$ and $IT = 10\%$ at: (a): $x/D = 2.5$, (b): $x/D = 5.5$, (c): $x/D = 8$

To further assess the capabilities of the AD/RANS model to determine the turbulence quantities in the wind turbine wake, the Sexbierum experiment (Cleijne, 1993) was modelled under different flow conditions with different turbulence models. Figures 3.13, 3.14 and 3.15 show the results. The different turbulence models varied in agreement with the experimental data. The $k - \varepsilon$ and $k - \varepsilon$ RNG models, were the least accurate, and they behaved similarly as expected. Next was the $k - \omega$ and then the $k - \omega$ SST models. Here, the issue of free turbulence decay is clearly shown as described by Cao et al. (2018). The source terms by Cao et al. (2018), gave more accurate results than the standard turbulence closure models. Also, as stated before, the turbulence quantities agree better with the experimental data in the far wake. Figure 3.13, which is closer to the rotor, shows a mismatch between the experimental data and the simulations. However, as the distance downstream of the rotor increases, the turbulence quantities begin to approach the experimental data as shown in figures 3.14 and 3.15. In all three figures, the turbulence closure model suggested by Cao et. al. (2018), proves to be the most accurate. This identifies that the free turbulence decay, that is an artefact of this kind of simulations, is affecting the accuracy of the turbulence modelling. However, all three figures show that the $k - \varepsilon$ and $k - \omega$ models could capture the peak of turbulence intensity on either sides of the rotor, better than Cao et al. (2018). Figures, 3.14 and 3.15 shows non symmetry in the experimental data, which is not captured by the AD/RANS model.

Figure 3.16, shows a contour of the turbulence kinetic energy free decay in the domain; the location of the rotor is specified but it is not present in this simulation. The issue identified by Cao et al. (2018) is clearly shown, i.e. the inlet value which is defined according to the values at the rotor, is decaying. In the actual scenario, the rotor will have a similar turbulence quantities as the inflow, which makes the free turbulence decay affect the accuracy of the simulations results, in consistence with Cao et al. (2018) suggestions.

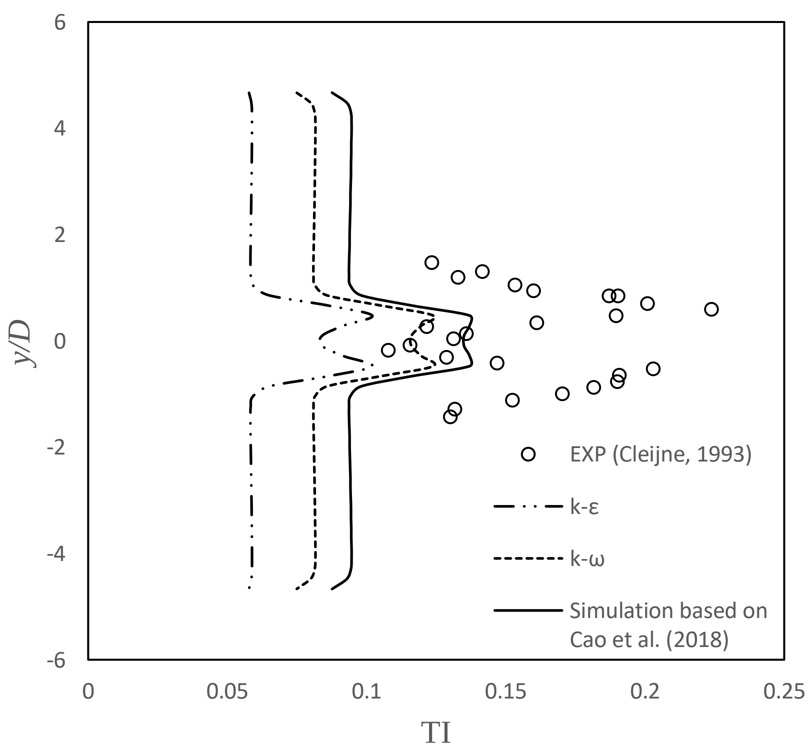

Figure 3.13. Sexbierum experiment: Wake turbulence intensity at $x = 2.5D$ for $V_o = 8.5\ ^{\mathrm{m}}/_{\mathrm{s}}$, $C_T = 0.75$ and $TI = 10\%$

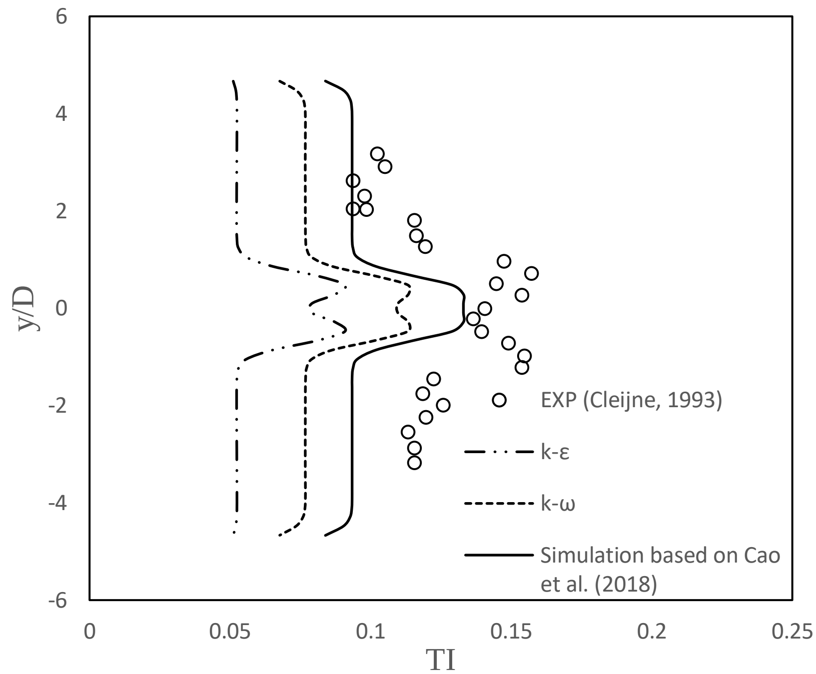

Figure 3.14. Sexbierum experiment: Wake turbulence intensity at $x = 5.5D$ for $V_o = 8.5\ ^{\mathrm{m}}/_{\mathrm{s}}$, $C_T = 0.75$ and $TI = 10\%$

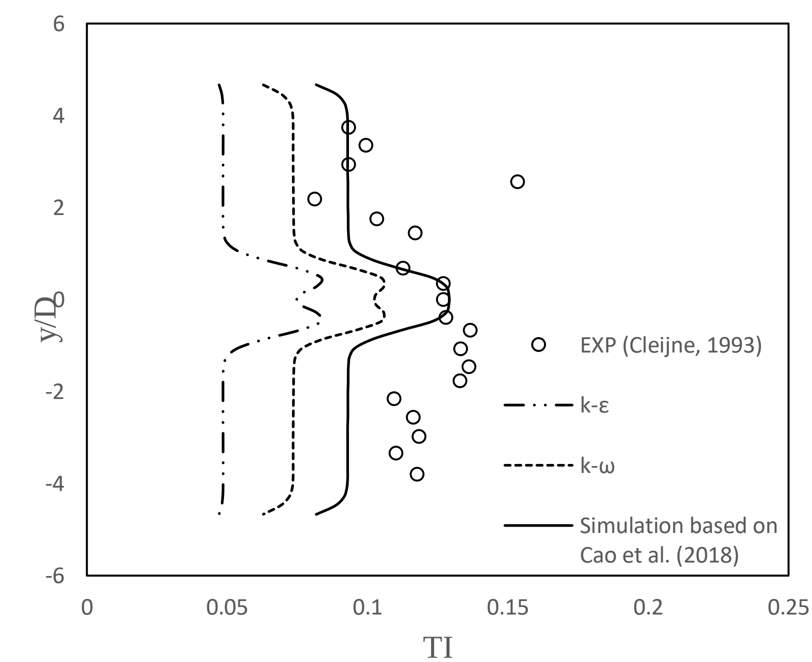

Figure 3.15. Sexbierum experiment: Wake turbulence intensity at $x = 8D$ for $V_o = 8.5\ ^{\mathrm{m}}/_{\mathrm{s}}$, $C_T = 0.75$ and $TI = 10\%$

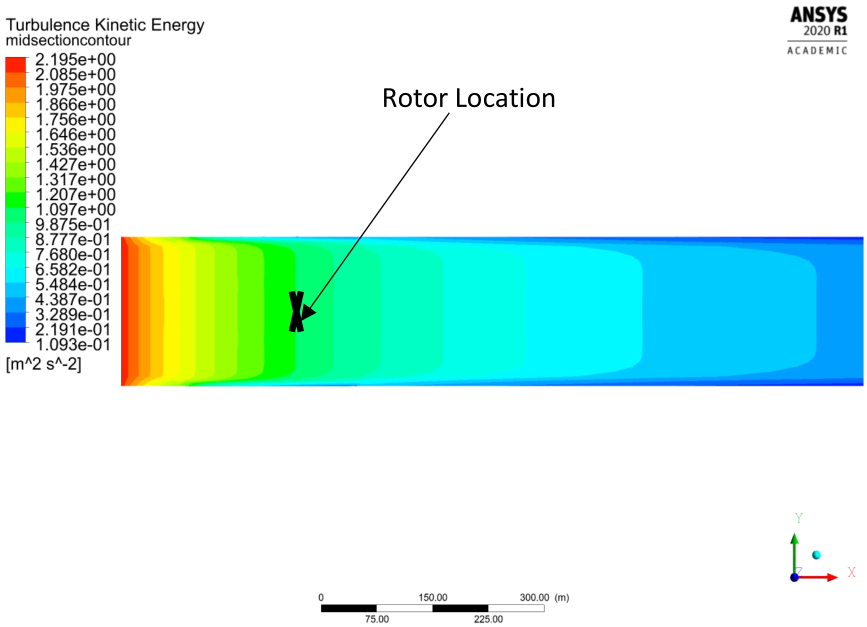

Figure 3.16. Contour of the decay of turbulence kinetic energy

The results above show that the AD/RANS model can predict the velocity deficit in the wake with good accuracy. Turbulence intensity on the other hand is not as accurate as the velocity deficit.

3.4.2.2 Two Wind Turbines in Tandem

To test the effect of spacing between two turbines in tandem, two in-line Nibe turbines were studied for a 7*D* spacing. Next, two Sexbeirum wind turbines were studied for several spacing distances.

Figure 3.17 is a sketch of the Sexbeirum experiment, where *s* is the distance between the two rotors. Three different locations in the wake of the second turbine were considered.

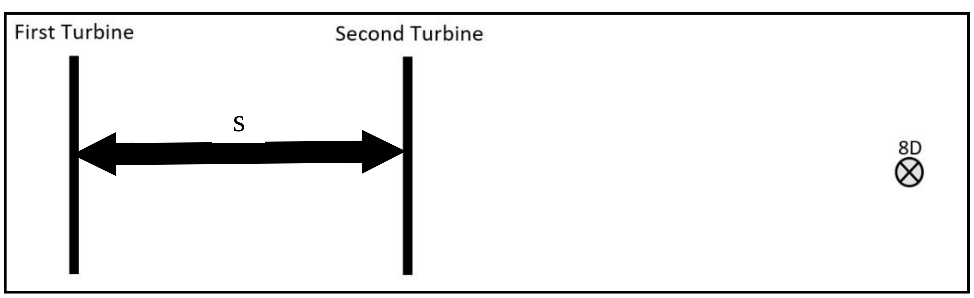

Figure 3.17. Sketch of the two turbines in tandem and the wake measurement locations

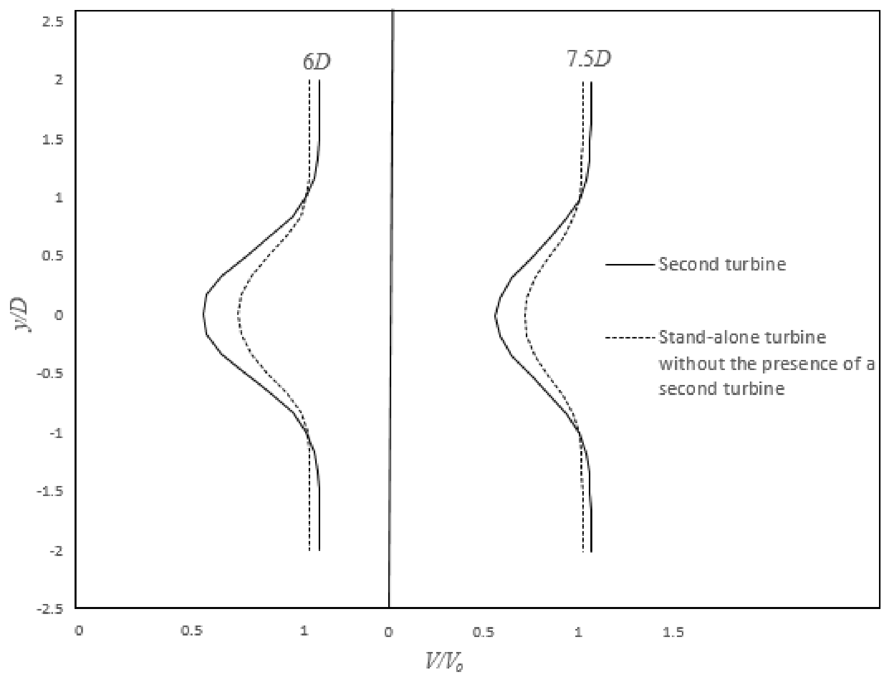

Figure 3.18. Nibe experiment for two turbines in tandem: Wake profile of velocity for $V_o = 8.5\ ^{\mathrm{m}}/_{\mathrm{s}}$, $C_T = 0.82$ and $TI = 11\%$ at: $x/D = 6$, $x/D = 7.5$

Figure 3.18 show the velocity profile at two different locations downstream of the second wind turbine located 7D from the first wind turbine. The two locations downstream were chosen to show the results in the beginning of the self-similar region. The prediction for the stand-alone turbine is also included. The results show that the velocity deficit is greater for the second turbine than the first turbine. Figure 3.18 also shows a higher spread rate for the second wind turbine. This implies that for a stand-alone wind turbine the recovery of momentum is faster than for the second turbine.

Figure 3.19 shows a contour plot of the velocity magnitude. The velocity is lower in the wake of the second turbine than the first turbine. Hence, placing the second turbine in the wake of the first turbine leads to a decreased power output. Note that the accelerated flow decreased earlier as shown by the red contours outside the wake region of the rotors. Figure 3.19 also indicates that as the distance between the turbines increase, the velocity deficit in the second turbine decreases. This is evident in the decreased intensity of the dark blue region behind the second turbine as the separation distance increases.

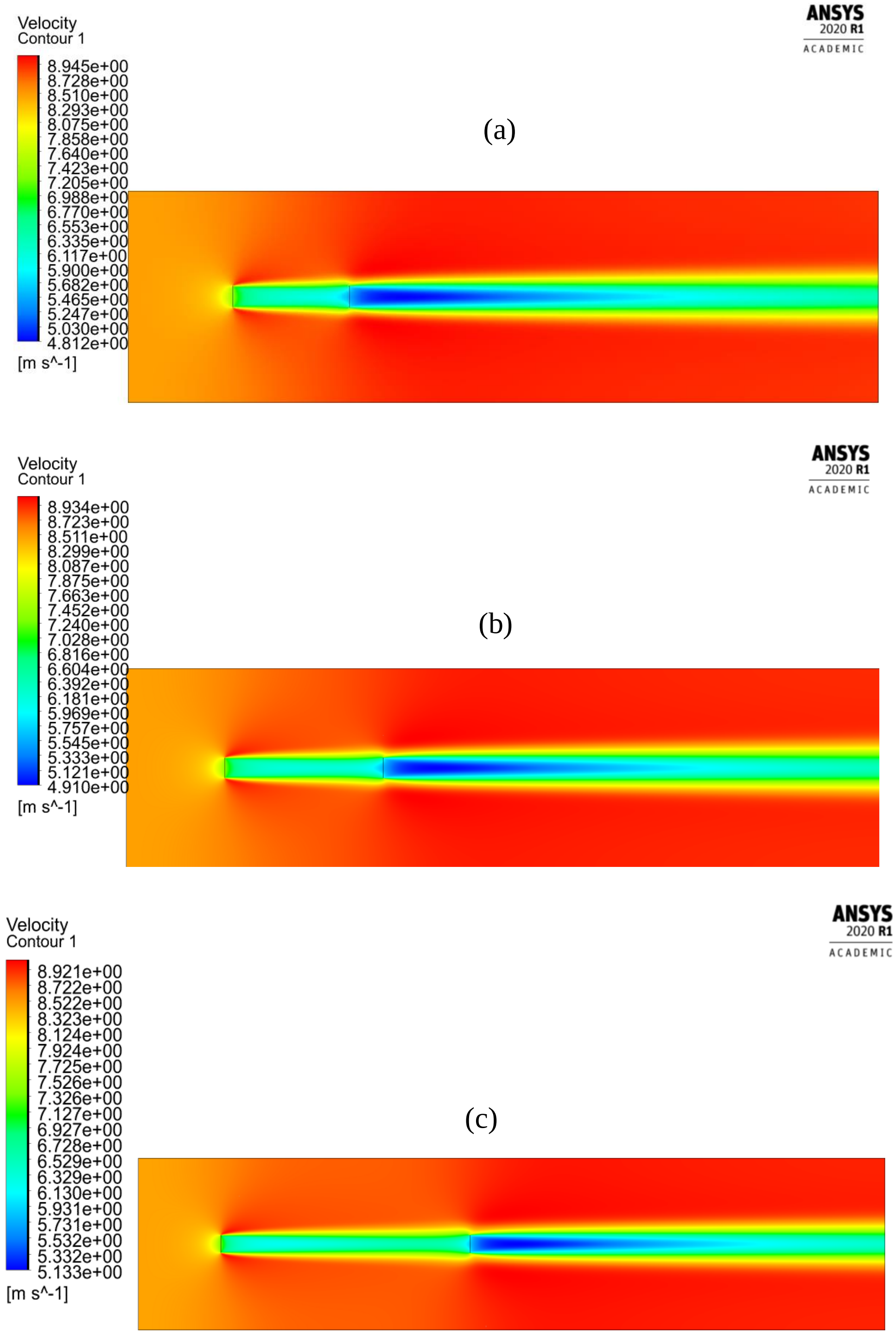

Figure 3.19. Sexbierum experiment for two turbines in tandem: Velocity contour for three different spacing s: (a): $s/D = 5.5$, (b): $s/D = 8$, (c): $s/D = 15$

Figure 3.20 shows the velocity deficit measurements $8D$ downstream of the second wind turbine for three different distances (s) between the first and the second wind turbine for the Sexbierum experiment. The wake profile 8*D* downstream of single turbine is included for comparison. When the separation distance between the two wind turbines is 5.5*D*, the velocity deficit is maximum of the three spacing distances considered. The Sexberium study shows that placing a wind turbine in the wake of another turbine will increase the velocity deficit, with only a 5.5% enhancement when the separation distance is increased from 5.5*D* to 15*D*. While the difference in velocity is minor, it is worth noting that a wind turbine's power output is a function of velocity to the third power. Meyers & Meneveau (2011) have shown that wind turbines should at least be 15*D* apart for them to operate efficiently, different to the 7*D* that was believed before (Meyers & Meneveau, 2011).

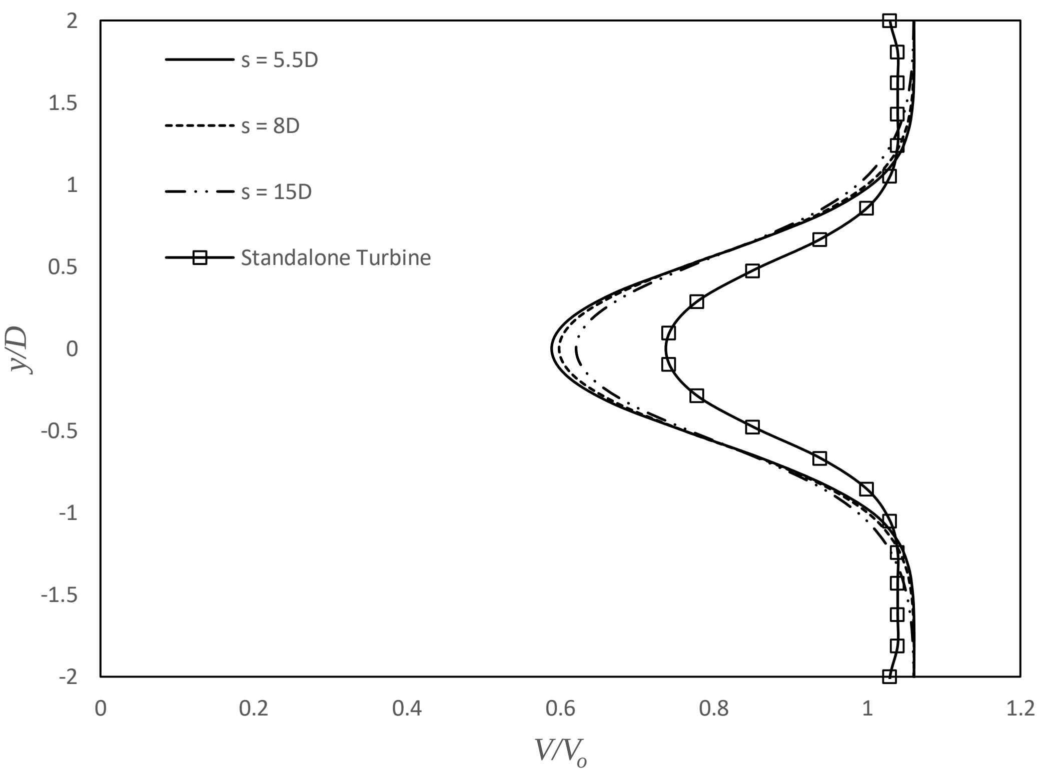

Figure 3.20. Sexbierum experiment for two turbines in tandem: Wake velocity profile for $V_o = 8.5\ {}^{\mathrm{m}}/_{\mathrm{s}}$, $C_T = 0.75$ and $TI = 10\%$ at $x/D = 8$ for three different turbine spacings s: $s/D = 5.5, 8$ and 15

Figure 3.21 shows contours of turbulence kinetic energy of two turbines in tandem for three different separation distances. This figure shows a distinct characteristic of the AD model. The rotor edge effects on turbulence kinetic energy are captured, however, the variation over the extent of the AD is minimal.

As the separation distance increases, the turbulence kinetic energy created by the second turbine decreases. Note the change in the maximum value of the turbulence kinetic energy in the three plots shown in figure 3.21.

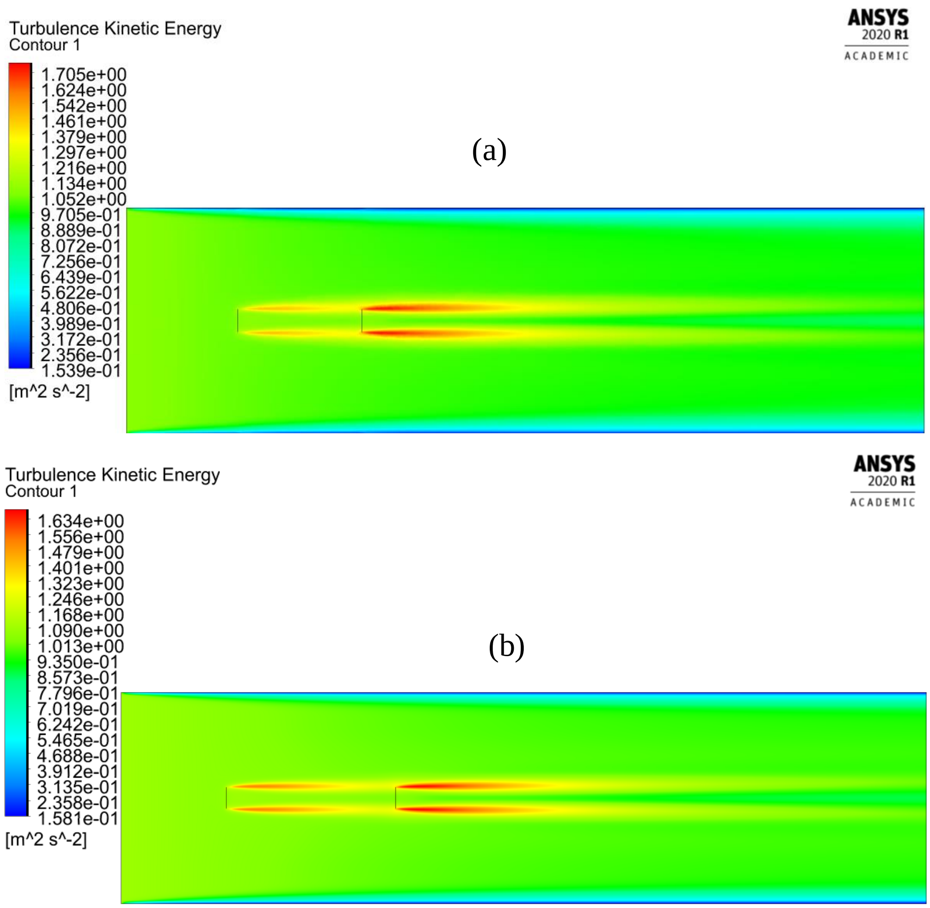

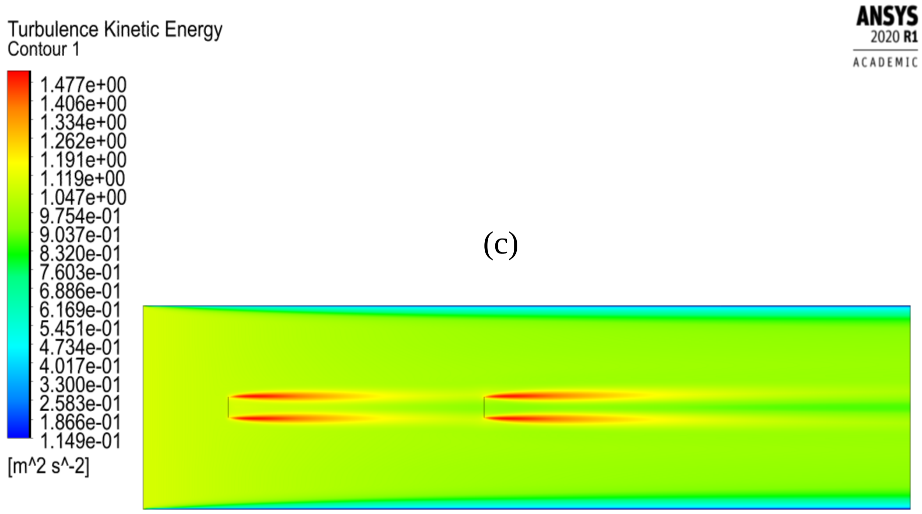

Figure 3.21. Sexbierum experiment for two turbines in tandem: contours of turbulence kinetic energy for spacings s: (a): $s/D = 5.5$, (b): $s/D = 8$, (c): $s/D = 15$

The turbulence kinetic energy at the rotor edge is further shown in figure 3.22 for the three different separation distances at a section 8*D* downstream of the second rotor. The maximum turbulence kinetic energy is shown to decrease approximately 8% as the separation distance increases from 5.5*D* to 15*D*. The profile as shown is dominated by the edge effects. This is also clearly reflected in figure 3.21. The decrease in turbulence kinetic energy with the increase in separation distance explains the importance of wind turbine separation distance on the life time of the turbines. The most common reason for early decommissioning of wind turbines is the fatigue arising from the poor placement of wind turbines in a wind farm. Most modern wind turbines are designed for 25 years of useful life, however some of them are often decommissioned as early as 7 years. This is mainly tied to the uneven cyclic loads arising from the turbulence field. Note that figure 3.22 shows the turbulence kinetic energy which is not to be confused with prior figures showing turbulence intensity.

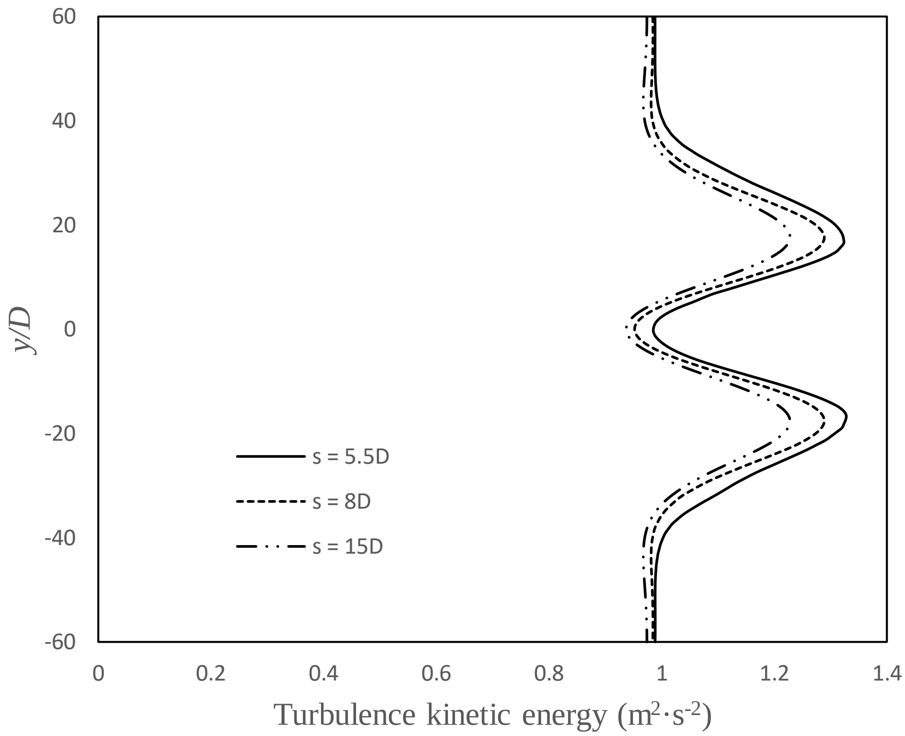

Figure 3.22. Sexbierum experiment for two turbines in tandem: Wake profile of turbulence kinetic energy for $V_o = 8.5\ ^{\mathrm{m}}/_{\mathrm{s}}$, $C_T = 0.75$ and $TI = 10\%$ at $x/D = 8$ for spacings of $s/D = 5.5, 8$ and 15

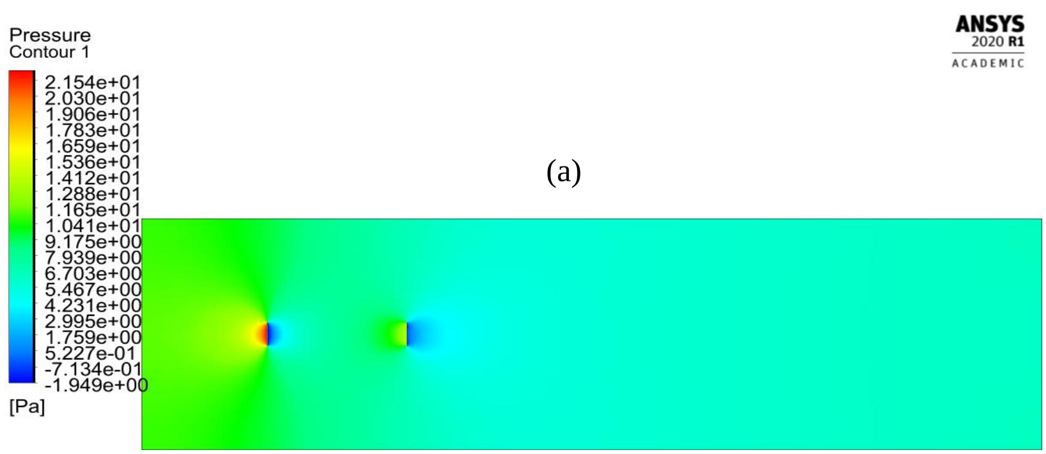

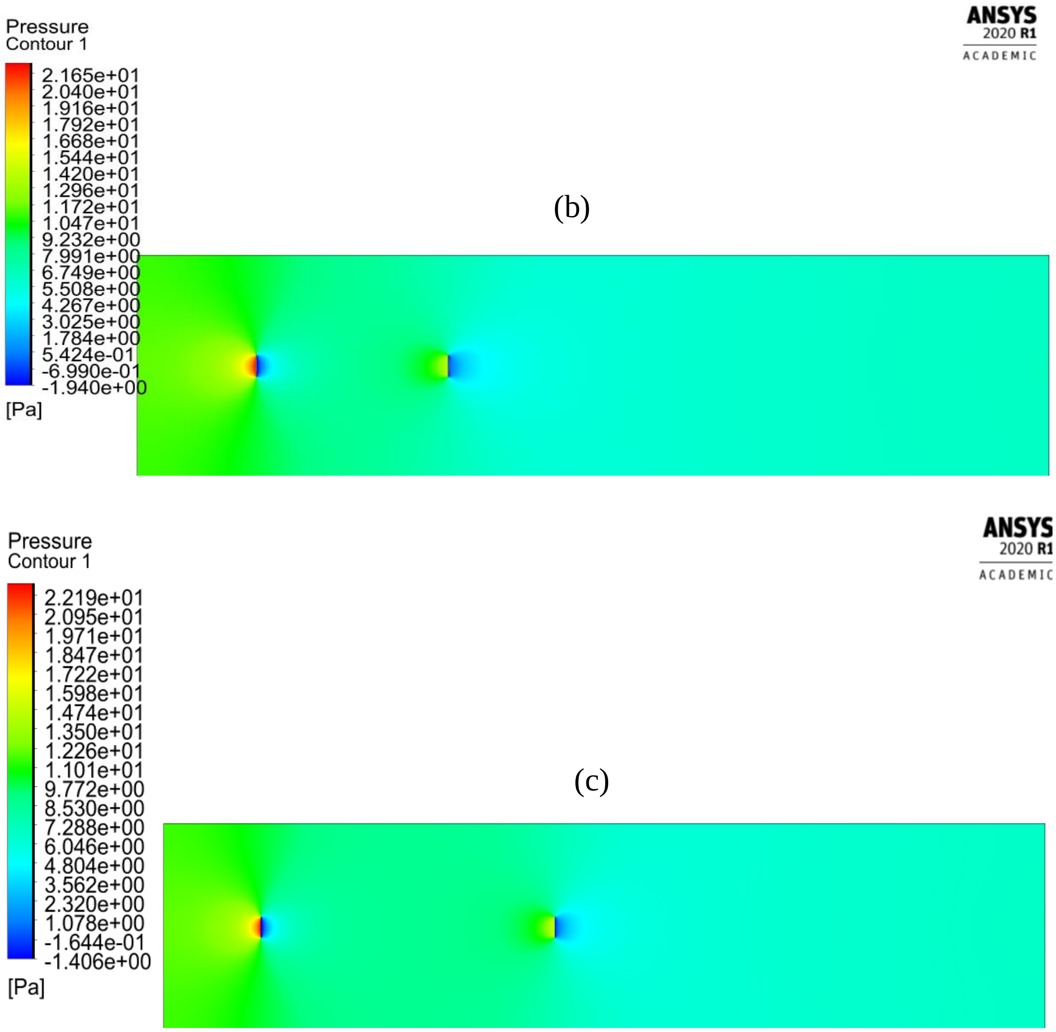

Figure 3.23. Sexbierum experiment for two turbines in tandem: Pressure contours for spacings s: (a): $s/D = 5.5$, (b): $s/D = 8$, (c): $s/D = 15$

Figure 3.23 shows the pressure contours of two turbines in tandem for three different separation distances. Pressure differences at the disc are the direct result of the AD model. The source term added is perceived as a pressure difference. Matching this pressure difference to the experimental data is crucial for accurate results. As seen in the figure, the pressure difference in the second turbine is always lower than that of the first turbine. This is due to the decrease in velocity in the wake which is directly related to the pressure value. As the spacing increases between the turbines, the velocity at the second turbine begins to recover, and the pressure values become closer to those of the first turbine.

3.4.3 Atmospheric Boundary Layer

The Sexbierum experiment was used to study the flow in a neutral atmospheric boundary layer. The formulation used for modelling the ABL followed the Panofsky and Dutton (1984) formulation. The domain was 3D, where the inlet implements user defined functions for the velocity, turbulence kinetic energy and dissipation, the outlet is an outflow, the top is a slip wall, and the bottom is a non-slip wall, and the side walls are zero shear stress walls. For this simulation, a standard $k - \varepsilon$ model was used with a standard wall function. To maintain a horizontally homogeneous flow, the roughness length was used to apply its equivalent sand grain roughness. Figure 3.24 shows a sketch of the domain.

Figure 3.25 shows the velocity values at three different locations downstream of the rotor compared to a profile taken 2*D* upstream of the rotor. There is a velocity deficit at all three locations, which is asymmetrical between the top and bottom sides of the rotor, this is due to the effect of surface roughness. For a rough surface, the blades above the hub experiences higher velocity than blades below the hub (Kabir & Ng, 2019). The top region appears to have regained more velocity than the lower half due to increased turbulence mixing with the undisturbed wind stream above the rotor, as demonstrated by the higher turbulence kinetic energy values in figure 3.26. Near the ground, the velocity for all three distances is greater than the upstream profile due to the accelerated flow around the AD.

As expected, the velocity deficit after 2.5*D* of the rotor is the highest, however from previous results, the ADM is proven to have inaccurate results for the near wake region. The curve labelled ABL is the velocity without the rotor. Figure 3.25 shows that after 8*D*, the flow has regained up to 78% of the undistributed wind speed.

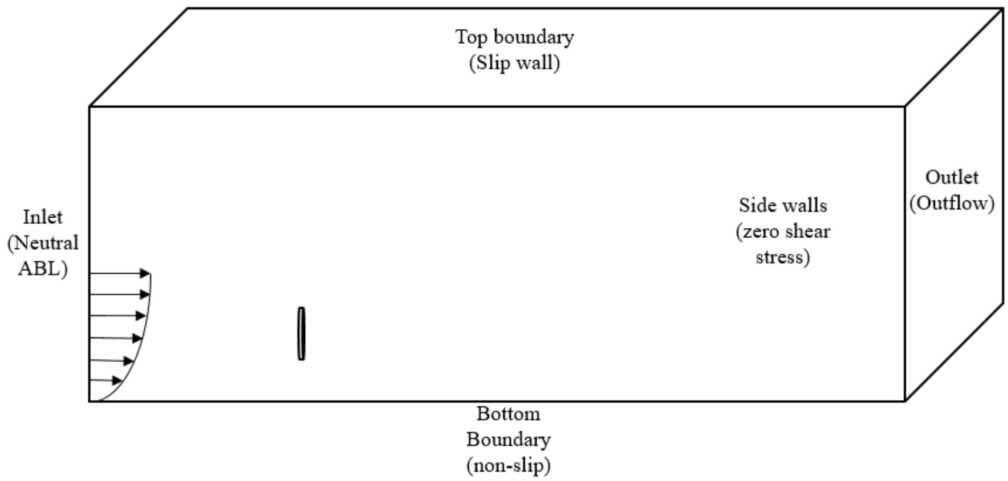

Figure 3.24. 3D view of the domains set up for ABL analysis

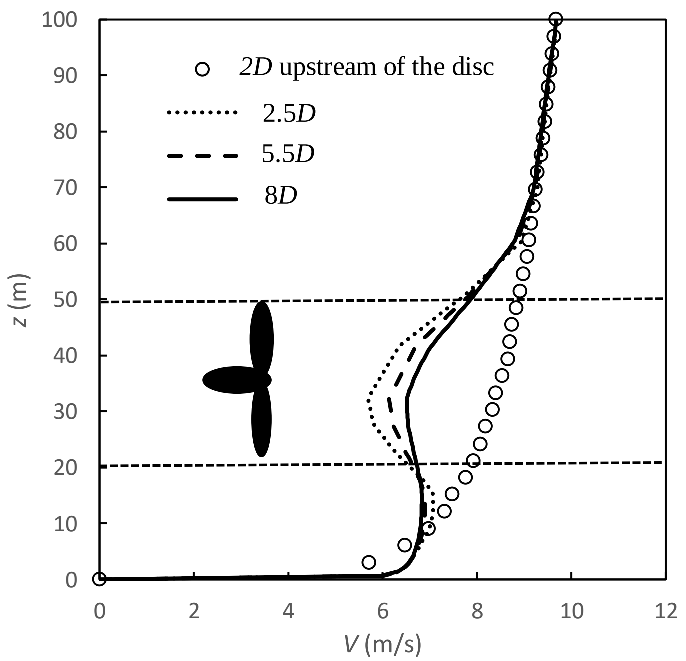

Figure 3.25. Sexbierum experiment: velocity profiles at three different locations downstream of the turbine comparted to a neutral ABL profile

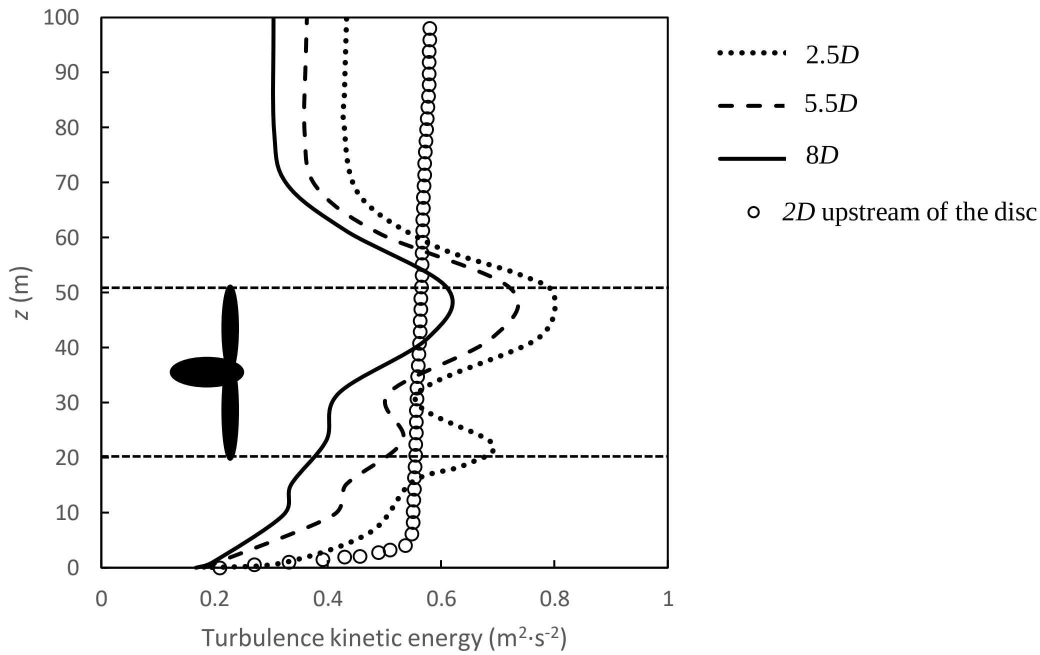

Figure 3.26. Sexbierum experiment: Turbulence kinetic energy profiles at three different locations downstream of the turbine comparted to a neutral ABL profile

Figure 3.26 shows the turbulence kinetic energy profiles for three wake different locations downstream of the rotor compared to a profile 2*D* upstream of the rotor. The elevated level of turbulence kinetic energy in the top half of the rotor is the most notable aspect of this figure. This is due to the turbulent mixing of the undisturbed flow above the wake zone with the wake region. The turbulence above represents a zone of large eddies, which mixes with the low momentum wake flow, boosting wake momentum and power production in any turbines located downstream. This is consistent with the findings of Wu et al. (2018), who found that increasing turbulence in the inflow stream increases power production and improves momentum regeneration for a specific wind farm. These results can also be related to the results of Breton et al. (2017). In their paper, the turbulence level was higher on the upper portion of the rotor under neutral ABL conditions. Although more turbulence may improve power output, it also raises the fatigue strains on the rotors.

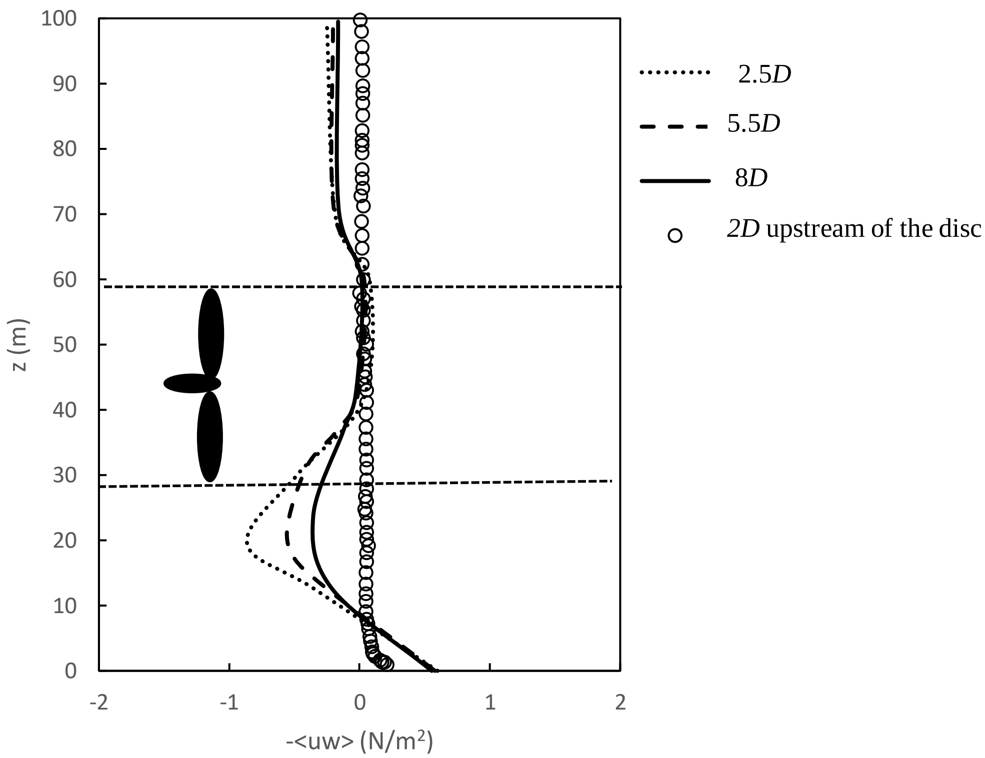

Figure 3.27. Sexbierum experiment: Reynolds stresses at three different locations downstream of the turbine comparted to a neutral ABL profile

Figure 3.27 shows the Reynolds shear stress $-< uw >$. The general trend of the graph agrees with the experimental data found in the literature (Hu et al., 2016). Figure 3.27 shows a strong negative shear on the lower side of the rotor, as well as a moderate shear on the upper half, near the rotor blades. The highest values appear to be on either end of the rotor, because of the relative velocity between the edge and the air, resulting in a strong shear. As the distance downstream increase, the relative velocity decreases, as well as the shear stress. Figure 3.27 shows a stronger shear stress on the lower portion of the rotor than the upper portion for the near wake region.

The ABL simulation introduces the effects of surface roughness and terrain on the analysis of the wind turbines wake, which is directly related to the turbulence level. The constant inlet analysis is valuable when comparing CFD results with wind tunnel data, however when modelling a real wind farm, a full ABL study with different stability functions should be implemented.

Chapter 4. Conclusion

Renewable energy generation is becoming increasingly important in meeting current and future energy demands as worries about resource availability, energy prices, environmental implications, and global population growth grow. Wind energy is believed to be one of the most cost-effective sources of renewable energy. Rotor diameters rise as wind turbines reach higher in the atmosphere, and wind farms extend above 20 kilometers in length. Advanced computational modelling is becoming increasingly important in analyzing the performance of a wind farm.

4.1 Summary

Wind turbine aerodynamic study has its origins in helicopter and propeller aerodynamics, and has progressed empirically until recently, when it was essentially passed off to advanced CFD analysis. Many studies over the last decade have laid the groundwork for understanding single turbine and total wind farm aerodynamics. From RANS to LES and modelling actuator discs to fully resolved rotating turbine blades, a variety of CFD approaches have been used.

The present study investigated the AD/RANS model to gain an understanding of the wake characteristics of a wind turbine. This thesis work proposed that the wake structure and interaction can be captured to a certain level using a simple computational model to save computational time and effort. At first, a parametric study was performed on three different standalone wind turbines under different inflow conditions with different turbulence closure models. It was found that the turbulence closure model has a noticeable effect on the results of the turbulence quantities, and the model by Cao et al. (2018) proved to give the best results.

Then two turbines were chosen to compare their interaction in terms of the wake effect on the turbine located downstream. For this analysis, the model proposed by Cao. et al. (2018) was used. The results show that as the distance between the turbines increases, the wake deficit will decrease, which translates to better performance of the subsequent turbines downstream.

Finally, an ABL analysis was performed using the Panofsky and Dutton (1982) neutral atmospheric boundary layer profile for the inlet conditions.

4.2 Key Results

The key results for the AD/RANS model are as follows:

1. When representing a wind turbine rotor using an actuator disc, defining the disc as an interface in the domain, rather than a 3D disc, will remove the uncertainty related to the disc thickness.
2. The coefficient proposed by Taylor (1963) proves to be significant for experimental analysis of the actuator disc model, however, for numerical analysis, the global thrust coefficient should be used.
3. The similarity analysis of the wake shows a spread rate of 0.065 and a centerline decay rate of $0.542(\frac{x}{D})^{-0.364}$, with a self-similar region beginning around 10*D* downstream of the rotor.
4. The AD/RANS model was shown to not well predict the wake characteristic of a wind turbine, where the spread and decay did not match the experimental data
5. The AD/RANS model will often under predict the turbulence intensity in the wake
6. The AD/RANS model is able to predict the edge effects to some level, however it fails to represent the hub effects on turbulence
7. The ABL study suggests that momentum is gained from above in the wake.
8. The present ABL simulation failed to bring strong turbulent diffusion from above. The AD/RANS model needs to be tested in more realistic atmospheric boundary layers.
9. Increasing the spacing between wind turbines up to 15*D* will only decrease the velocity deficit by 5%.

4.3 Suggestions for Future Work

This research is one approach to a long-standing challenge of understanding wind turbine wake interaction in order to optimize turbine spacing for maximum power output and minimal wear damage. It also raises questions that need to be investigated further. The ability to enhance and expand models would be greatly aided by removing the limitation of desktop computer capabilities.

Models such as the actuator line model, could be utilized in a future work to better understand the wake interaction and to assess the actuator methods in comparison to fully resolved methods and experimental data.

The current thesis work was restricted to the neutral ABL condition. The diurnal cycle, in reality, is made up of constantly changing convective and steady ABL conditions. Incorporating some of these conditions into the simulations would be beneficial. These conditions should ideally be included in a complete wind farm simulation with a LES framework.

References

ANSYS (2020). ANSYS Fluent Theory Guide; Ansys. Inc.: Canonsburg, PA, USA.

Apata, O., & Oyedokun, D. (2020). An overview of control techniques for wind turbine systems. Scientific African, 10, 2–3. https://doi.org/10.1016/j.sciaf.2020.e00566

Bazilevs, Y., Hsu, M. C., Akkerman, I., Wright, S., Takizawa, K., Henicke, B., Spielman, T., & Tezduyar, T. E. (2010). 3D simulation of wind turbine rotors at full scale. Part I: Geometry modeling and aerodynamics. International Journal for Numerical Methods in Fluids, 65(1–3), 207–235. https://doi.org/10.1002/fld.2400

Betz, A. (1920). Das Maximum Der Theoretisch Möglichen Ausnützung Des Windes Durch Windmotoren. Zeitschrift Für Das Gesamte Turbinewessen, 26, 307–309.

Breton, S.-P., Sumner, J., Sørensen, J. N., Hansen, K. S., Sarmast, S., & Ivanell, S. (2017). A survey of modelling methods for high-fidelity wind farm simulations using large eddy simulation. Philosophical Transactions of the Royal Society A: Mathematical, Physical and Engineering Sciences, 375(2091): p. 20160097. https://doi.org/10.1098/rsta.2016.0097

Burton, T., Jenkins, N., Sharpe, D., & Bossanyi, E. (2011). Wind Energy Handbook. Wiley: Hoboken, New Jersey, USA.

Calaf, M., Meneveau, C., & Meyers, J. (2010). Large eddy simulation study of fully developed wind-turbine array boundary layers. Physics of Fluids, 22(1), p. 015110. https://doi.org/10.1063/1.3291077

Cao, J., Zhu, W., Shen, W., Sørensen, J., & Wang, T. (2018). Development of a CFD-Based Wind Turbine Rotor Optimization Tool in Considering Wake Effects. Applied Sciences, 8(7), 1056. Http://dx.doi.org/10.3390/App8071056

Chen, Y.S., & Kim, S.W. (1987). Computation of Turbulent Flow Using an Extended Turbulence Closure Model. NASA Contractor Report. NASA CR-179204.

Christiansen, M. B., & Hasager, C. B. (2006). Using airborne and satellite SAR for wake mapping offshore. Wind Energy, 9(5), 437–455. https://doi.org/10.1002/we.196

Cleijne, J.W. (1993). Results of the Sexbierum Wind Farm; Single Wake Measurements, TNO Report 93082, TNO Institute of Environmental and Energy Technology, The Netherlands.

Crespo, A., Manuel, F., Moreno, D., Fraga, E., & Hernandez, J. (1985). Numerical analysis of wind turbine wakes. In Workshop on Wind Energy Applications, 15-25, Delphi, Greece.

Dvorak, P. (2014). Vertical-axis wind turbines: what makes them better? - Windpower Engineering. Windpower Engineering & Development. Retrieved July 15, 2021, from https://www.windpowerengineering.com/vertical-axis-wind-turbines/

Eggleston, D.M. & Stoddard, F.S. (1987). Wind Turbine Engineering Design, Van Nostrand Rheinhold, New York.

El Kasmi, A., & Masson, C. (2008). An extended model for turbulent flow through horizontal-axis wind turbines. Journal of Wind Engineering and Industrial Aerodynamics, 96(1), 103–122. https://doi.org/10.1016/j.jweia.2007.03.007

Emeis, S. (2010). Meteorlogical Explanation of Wake Clouds at Horns Rev Wind Farm. Deutsches Widenergi Institut Magazin, 37, 52-55.

Engineering ToolBox, (2004). Drag Coefficient. [online] Available at: https://www.engineeringtoolbox.com/drag-coefficient-d_627.html [Accessed 12th February 2022].

Euler, L. (1752). Histoire De L'académie Royale Des Sciences et Des Belles Lettres De Berlin: Akademie Der Wissenschaften Der Ddr. Histoire De L'académie Royale Des Sciences et Des Belles Lettres De Berlin. 8, 185-232. Https://Archive.Org/Details/Histoiredelacad03unkngoog/Page/N215/Mode/2up.

Fleischer, C. (2021). The History of Wind Energy: Eagle: Blog. Https://Www.Autodesk.Com/Products/Eagle/Blog/Wind-Energy/.

Frandsen, S., Barthelmie, R., Pryor, S., Rathmann, O., Larsen, S., Højstrup, J., & Thøgersen, M. (2006). Analytical modelling of wind speed deficit in large offshore wind farms. Wind Energy, 9(1–2), 39–53. https://doi.org/10.1002/we.189

From oil crisis to energy revolution – how nations once before planned to kick the oil habit. (2019). Rapid Transition Alliance. https://www.rapidtransition.org/stories/from-oil-crisis-to-energy-revolution-how-nations-once-before-planned-to-kick-the-oil-habit/

Froude, W. (1878). On the Elementary Relation between Pitch, Slip and Propulsive Efficiency. Transactions of the Royal Institution of Naval Architects, 19(47): 47–57.

Froude, W. (1889). On the Part Played in Propulsion by Difference in Pressure. Transaction of the Institute of Naval Architects; 30, 390–423.

Gardiner, G. (2011). HAWTS vs. VAWTS. Composites World. https://www.compositesworld.com/articles/hawts-vs-vawts.

Glauert, H. (1926). The Analysis of Experimental Results in the Windmill Brake and Vortex Ring States of an Airscrew. London: Aeronautical Research Committee, 1026.

Glauert, H. (1935). Airplane Propellers. In W. F. Durand, Editor, Aerodynamic Theory, 4, 169–360. Berlin: Julius Springer.

Government of Canada. (2021). Canada Energy Regulator. https://www.cer-rec.gc.ca/en/index.html

Hahm, T., & Wußow, S. (2013). Turbulent Wakes in Wind Farm Configuration. Paper presented at the European Wind Energy Conference & Exhibition (EWEC 2006), Athens, Greece. WindEurope Publications.
https://www.proceedings.com/16319.html

Hanjalic, K., Launder, B. E., & Schiestel, R. (1980). Multiple-Time-Scale Concepts in Turbulent Transport Modeling. In Von Karman Institution for Fluid Dynamics Measurements and Predictions of Complex Turbulent Flows, 1, 35-49.

Hansen, M. O. L. (2008). Aerodynamics of Wind Turbines. London.
https://orbit.dtu.dk/en/publications/aerodynamics-of-wind-turbines-second-edition

Harrison, M., Batten, W., Myers, L., & Bahaj, A. (2010). Comparison between CFD simulations and experiments for predicting the far wake of horizontal axis tidal turbines. IET Renewable Power Generation, 4(6), 613-627. https://doi.org/10.1049/iet-rpg.2009.0193

Helvig, S. D. J., Vinnes, M. K., Segalini, A., Worth, N. A., & Hearst, R. J. (2021). A comparison of lab-scale free rotating wind turbines and actuator disks. Journal of Wind Engineering and Industrial Aerodynamics, 209, Article 104485. https://doi.org/10.1016/j.jweia.2020.104485

Hu, J., Yang, Q., & Zhang, J. (2016). Study on the Wake of a Miniature Wind Turbine Using the Reynolds Stress Model. Energies, 9(10), 784-802. http://dx.doi.org/10.3390/en9100784

Johnson, B., Francis, J., Howe, J., & Whitty, J. (2014). Computational Actuator Disc Models for Wind and Tidal Applications. Journal of Renewable Energy, 2014, 1–10.
https://doi.org/10.1155/2014/172461

Joukowsky, N., (1920). Windmill of the NEJ Type. Transactions of the Central Institute for Aero hydrodynamics of Moscow.

Kabir, I. F., & Ng, E. (2019). Effect of different atmospheric boundary layers on the wake characteristics of NREL phase VI wind turbine. Renewable Energy, 130, 1185–1197.
https://doi.org/10.1016/j.renene.2018.08.083

Kalvig, S., Manger, E., & Hjertager, B. (2014). Comparing different CFD wind turbine modelling approaches with wind tunnel measurements. Journal of Physics: Conference Series, 555, 012056. https://doi.org/10.1088/1742-6596/555/1/012056

Lanchester. (1915). A Contribution to the Theory of Propulsion and the Screw Propeller. Transaction of the Institution of Naval Architects, 27, 509-510.

Launder, B. E., & Spalding, D. B. (1974). The numerical computation of turbulent flows. Computer Methods in Applied Mechanics and Engineering, 3(2), 269–289. Elsevier BV. https://doi.org/10.1016/0045-7825(74)90029-2

Leishman, J. G. (2006). Principles of Helicopter Aerodynamics. New York: Cambridge University Press.

Magnusson, M., & Smedman, A. S. (1999). Air flow behind wind turbines. Journal of Wind Engineering and Industrial Aerodynamics, 80(1–2), 169–189. https://doi.org/10.1016/s0167-6105 (98)00126-3

Maine Government. (2000). Facts about wind energy and noise. Retrieved July 6, 2022, from https://www.maine.gov/dacf/lupc/projects/windpower/redington/Documents/Section05_Sound/AWEA_Turbine_Noise_FAQ.pdf

Marmidis, G., Lazarou, S., & Pyrgioti, E. (2008). Optimal placement of wind turbines in a wind park using Monte Carlo simulation. Renewable Energy, 33(7), 1455-1460.

Mason-Jones, A., O'Doherty, T., O'Doherty, D. M., & Evans, P. S. (2008). Characterisation of a HATT using CFD and ADCP site data. World Renewable Energy Congress, Glasgow, UK.

McGowan, J. G., & Connors, S. R. (2000). Wind Power: A Turn of the Century Review. Annual Review of Energy and the Environment, 25(1), 147–197. https://doi.org/10.1146/annurev.energy.25.1.147

Medici, D. (2005). Experimental studies of wind turbine wakes : power optimization and meandering (PhD dissertation), KTH. http://urn.kb.se/resolve?urn=urn:nbn:se:kth:diva-598

Menter, F. R. (1994). Two-equation eddy-viscosity turbulence models for engineering applications. AIAA Journal, 32(8), 1598–1605. https://doi.org/10.2514/3.12149

Meyers, J., & Meneveau, C. (2011). Optimal turbine spacing in fully developed wind farm boundary layers. Wind Energy, 15(2), 305–317. https://doi.org/10.1002/we.469

Mikkelsen, R. F. (2004). Actuator Disc Methods Applied to Wind Turbines (PhD dissertation). Technical University of Denmark. https://orbit.dtu.dk/en/publications/actuator-disc-methods-applied-to-wind-turbines

Musgrove, P. (2010). Wind Power. Cambridge: Cambridge University Press.

Orszag, S. A., Staroselsky, I., Flannery, W. S., & Zhang, Y. (1996). Modeling of Turbulent Transport Equations. Simulation and Modeling of Turbulent Flows. Oxford University Press, Oxford, UK, 155–184. https://doi.org/10.1093/oso/9780195106435.003.0009

Patankar, S. V. (1980). Numerical Heat Transfer and Fluid Flow. Hemisphere Publication Corporation, Washington.

Panofsky, H., & Dutton, J., (1984). Atmospheric Turbulence, 19. Wiley, New Jersey, USA.

Pope, S. B. (2000). Turbulent flows. Cambridge University Press, Cambridge, England.

Porté-Agel, F., Wu, Y. T., Lu, H., & Conzemius, R. J. (2011). Large-eddy simulation of atmospheric boundary layer flow through wind turbines and wind farms. Journal of Wind Engineering and Industrial Aerodynamics, 99(4), 154–168. https://doi.org/10.1016/j.jweia.2011.01.011

Prospathopoulos, J. M., Politis, E. S., Rados, K. G., & Chaviaropoulos, P. K. (2010). Evaluation of the effects of turbulence model enhancements on wind turbine wake predictions. Wind Energy, 14(2), 285–300. https://doi.org/10.1002/we.419

Putnam, G.C. (1948). Power from the Wind. Van Nostrand Rheinhold, New York.

Rankine, W. J. M. (1865). On The Mechanical Principles of the Action of Propellers. Transaction of the Institution of Naval Architects, 6, 13–39.

Saffman, P. G. (1970). A model for inhomogeneous turbulent flow. Proceedings of the Royal Society of London. A. Mathematical and Physical Sciences, 317(1530), 417–433. https://doi.org/10.1098/rspa.1970.0125

Sanderse, B. (2009). Aerodynamics of Wind Turbine Wakes-literature Review. TNO Publications, The Hague, Netherlands.

Schaffarczyk, A. P. (2014). Introduction to Wind Turbine Aerodynamics. Springer Publishing, New York, USA.

Sforza, P. M., Sheerin, P., & Smorto, M. (1981). Three-Dimensional Wakes of Simulated Wind Turbines. AIAA Journal, 19(9), 1101–1107. https://doi.org/10.2514/3.60049

Sørensen, J.N. (2012). Aerodynamic Analysis of Wind Turbines. Comprehensive Renewable Energy, 2, 225–241. https://doi.org/10.1016/b978-0-08-087872-0.00209-2

Spalart, P. R., & Rumsey, C. L. (2007). Effective Inflow Conditions for Turbulence Models in Aerodynamic Calculations. AIAA Journal, 45(10), 2544–2553. https://doi.org/10.2514/1.29373

Spalding, D. B. (1972). A novel finite difference formulation for differential expressions involving both first and second derivatives. International Journal for Numerical Methods in Engineering, 4(4), 551-559.

Spera, D. A. (1994). Wind Turbine Technology: Fundamental Concepts in Wind Turbine Engineering, Second Edition [E-book], 47-72. ASME Press (American Society of Mechanical Engineers), New York, USA.

Sumner, J., Espana, G., Masson, C., & Aubrun, S. (2013). Evaluation of RANS/actuator disk modelling of wind turbine wake flow using wind tunnel measurements. International Journal of Engineering Systems Modelling and Simulation 47, 5(1-3), 147-158.

Tachos, N. S., Filios, A. E., & Margaris, D. P. (2010). A comparative numerical study of four turbulence models for the prediction of horizontal axis wind turbine flow. Proceedings of the Institution of Mechanical Engineers, Part C: Journal of Mechanical Engineering Science, 224(9), 1973–1979. https://doi.org/10.1243/09544062jmes1901

Taylor, G.I. (1963). The Scientific Papers of Sir Geoffrey Ingram Taylor, Ed. G.K. Batchelor. Cambridge University Press, Cambridge, UK.

Taylor, G. J., Milborrow, D. J., McIntosh, D. N., & Swift-Hook, D. T. (1985). Wake measurements on the Nibe windmills. In Proceedings of Seventh BWEA Wind Energy Conference, Oxford, 67-73, Mechanical Engineering Publications.

Tossas, L. A. M., & Leonardi, S. (2013). Wind Turbine Modeling for Computational Fluid Dynamics: December 2010 - December 2012. U.S. Department of Energy Office of Scientific and Technical Information. https://doi.org/10.2172/1089598

Van Kuik, G., Ummels, B., & Hendriks, R. (2008). Perspectives on Wind Energy. Sustainable Energy Technologies, Springer, Dordrecht, 75–97. https://doi.org/10.1007/978-1-4020-6724-2_4

Vermeer, L. J., Sørensen, J. N., & Crespo, A. (2003). Wind turbine wake aerodynamics. Progress in Aerospace Sciences, 39(6-7), 467-510.

Whelan, J., Thomson, M., Graham, J., Peiro, J. (2007). Modelling of free surface proximity and wave induced velocities around a horizontal axis tidal stream turbine. Paper presented at 7th European Wave and Tidal Energy Conference (EWTEC 2007), Porto, Portugal.

Wilcox, D. C. (1988). Multiscale model for turbulent flows. AIAA Journal, 26(11), 1311-1320.

Wu, Y., Lin, C., & Chang, T. (2020). Effects of inflow turbulence intensity and turbine arrangements on the power generation efficiency of large wind farms. In Wind Energy, Wiley, 23(7), 1640–1655. https://doi.org/10.1002/we.2507

Yakhot, V., & Smith, L. M. (1992). The Renormalization Group, the ε-Expansion and Derivation of Turbulence Models. Journal of Scientific Computing, Springer Science and Business Media LLC, 7(1), 35-61. https://doi.org/10.1007/BF01060210

Appendix A – Meshes and Description of the Simulations Setup

The domain mesh and grid independence studies are shown below. The mesh for the 2D domain is shown in Figure A.1, while the mesh for the 3D domain is shown in Figure A.2. The grid independence study for both types of experiments according to the axial induction factor is shown in Tables A.1 and A.2. With around 70,000 components, the 2D simulations become grid independent, and the average simulation time is roughly 5 min. At roughly 600,000 elements, the 3D simulations become grid independent, and the average simulation duration varies depending on the turbulence closure mode. A simulation with the Cao et al. (2018) model runs for almost 8 h. Finally, the ABL simulations proved to be the most difficult to converge. In terms of the UDF used to determine the inlet velocity, turbulence kinetic energy, and dissipation, this simulation is delicate. This experiment lasted a full 24 h, and it used all of the desktop's RAM while the four cores worked in parallel. Nearly 2 million elements were used. Figure A.3 shows the mesh for the ABL simulation.

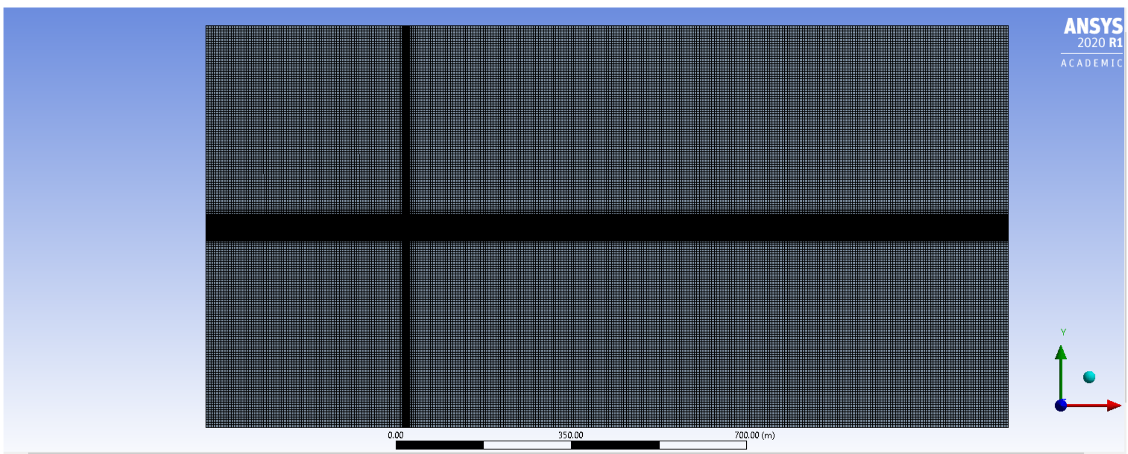

Figure A.1. The 2D mesh used for the preliminary study

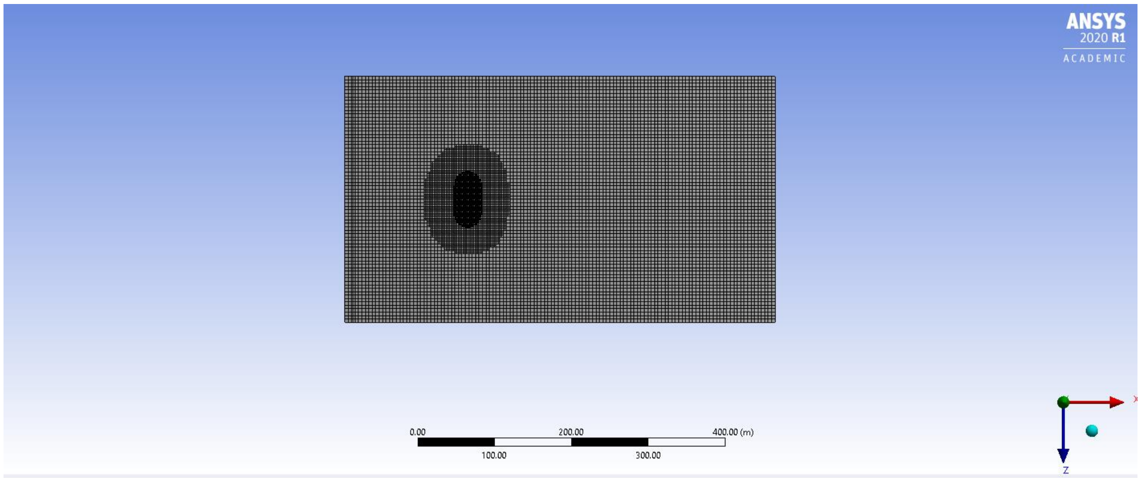

Figure A.2. The 3D mesh used for the results section

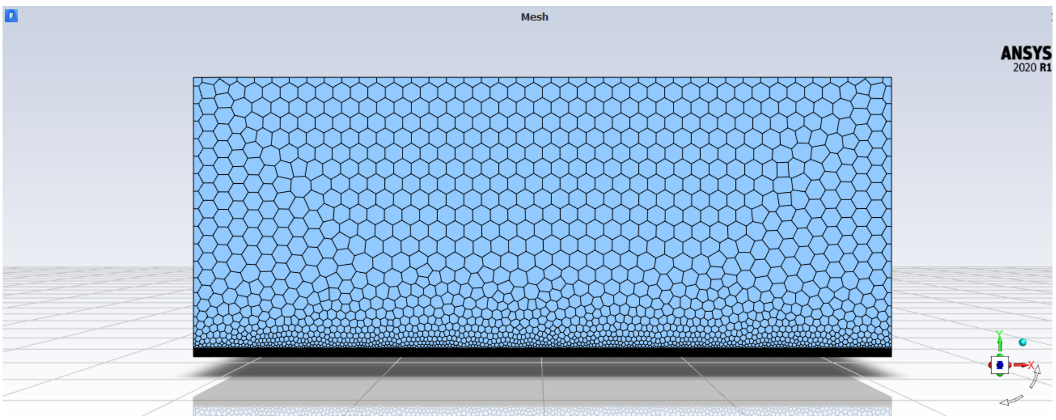

Figure A.3. The mesh used for the ABL simulation

Table A.1. Grid independence study (2D)

Number of Elements	Number of actuating points	Axial induction factor at $\boldsymbol{x/D} = 0$ (at the rotor)
3,284	**10**	**0.171**
12,620	**20**	**0.159**
50,280	**40**	**0.153**
68,980	**40**	**0.150**
105,280	**40**	**0.150**
200,720	**80**	**0.150**

Table A.2. Grid independence study (3D)

Number of Elements	Number of actuating points	Axial induction factor at $\boldsymbol{x/D}$ = 0 (at the rotor)
171,952	**~1250**	**0.162**
371,663	**~1250**	**0.162**
557,184	**~1250**	**0.161**
842,646	**~1250**	**0.161**

Appendix B – Permissions to Use

Permission for figure 1.1

ahmad beqai
Hello, I was seeking copyright permission to reproduce the "Photograph of the wake expansion of Horns Rev wind farm" in my master's thesis. Please find attached

press@vattenfall.com
to me

Hello,
Thanks for your request. Yes, you can use the photo of the Horns Rev offshore wind farm.

Please state "Vattenfall" in a photo byline.

Best regards from Stockholm

/Markus

Med vänliga hälsningar

Markus Fischer
Pressekreterare / Press Officer

Communications
Media Relations Nordics / EU

M +46 70 3779644
markus.fischer@vattenfall.com

VATTENFALL

Adress: Evenemangsgatan 13, 16992 Solna

https://www.fossilfreedom.com

Permission for figures 2.1, 2.2, 2.4, 2.5 and 2.6

CCC | Marketplace™

Order Date	13-Jun-2022	Type of Use	Republish in a thesis/dissertation
Order License ID	1233629-1	Publisher	Routledge
ISBN-13	9781844074389	Portion	Chart/graph/table/figure

LICENSED CONTENT

Publication Title	Aerodynamics of Wind Turbines, 2nd edition	Country	United Kingdom of Great Britain and Northern Ireland
Author/Editor	Hansen, Martin O. L.	Rightsholder	Taylor & Francis Informa UK Ltd - Books
Date	12/20/2007	Publication Type	Book
Language	English	URL	http://www.tandfebooks.com/isbn/97818...

REQUEST DETAILS

Portion Type	Chart/graph/table/figure	Distribution	Worldwide
Number of charts / graphs / tables / figures requested	5	Translation	Original language of publication
		Copies for the disabled?	No
Format (select all that apply)	Electronic	Minor editing privileges?	No
Who will republish the content?	Academic institution	Incidental promotional use?	No
Duration of Use	Life of current edition	Currency	CAD
Lifetime Unit Quantity	Up to 499		
Rights Requested	Main product		

NEW WORK DETAILS

Title	COMPUTATIONAL MODELLING OF WIND TURBINE WAKES USING AN ACTUATOR DISC COUPLED WITH REYNOLDS AVERAGED NAVIER-STOKES MODELS	Institution name	University of Saskatchewan
		Expected presentation date	2022-06-28
Instructor name	Donald Bergstrom		

ADDITIONAL DETAILS

Order reference number	N/A	The requesting person / organization to appear on the license	University of Saskatchewan

REUSE CONTENT DETAILS

Title, description or numeric reference of the portion(s)	1-D Momentum Theory for an Ideal Wind Turbine	Title of the article/chapter the portion is from	1-D Momentum Theory for an Ideal Wind Turbine
Editor of portion(s)	N/A	Author of portion(s)	Hansen, Martin O. L.
Volume of serial or monograph	N/A	Issue, if republishing an article from a serial	N/A
Page or page range of portion	27-40	Publication date of portion	2007-12-19

Permission for figure 2.8

CCC | Marketplace™

Order Date	13-Jun-2022	Type of Use	Republish in a thesis/dissertation
Order License ID	1233785-1	Publisher	ELSEVIER BV
ISSN	0167-6105	Portion	Chart/graph/table/figure

LICENSED CONTENT

Publication Title	Journal of wind engineering and industrial aerodynamics	Rightsholder	Elsevier Science & Technology Journals
Article Title	Large-eddy simulation of atmospheric boundary layer flow through wind turbines and wind farms	Publication Type	Journal
		Start Page	154
		End Page	168
Author/Editor	INTERNATIONAL ASSOCIATION FOR WIND ENGINEERING.	Issue	4
		Volume	99
Date	01/01/1975		
Language	Dutch		
Country	Netherlands		

REQUEST DETAILS

Portion Type	Chart/graph/table/figure	Distribution	Worldwide
Number of charts / graphs / tables / figures requested	2	Translation	Original language of publication
		Copies for the disabled?	No
Format (select all that apply)	Electronic	Minor editing privileges?	No
Who will republish the content?	Academic institution	Incidental promotional use?	No
Duration of Use	Life of current edition	Currency	CAD
Lifetime Unit Quantity	Up to 499		
Rights Requested	Main product		

NEW WORK DETAILS

Title	COMPUTATIONAL MODELLING OF WIND TURBINE WAKES USING AN ACTUATOR DISC COUPLED WITH REYNOLDS AVERAGED NAVIER-STOKES MODELS	Institution name	University of Saskatchewan
		Expected presentation date	2022-06-28
Instructor name	Donald Bergstrom		

ADDITIONAL DETAILS

Order reference number	N/A	The requesting person / organization to appear on the license	University of Saskatchewan

REUSE CONTENT DETAILS

Title, description or numeric reference of the portion(s)	Large-eddy simulation of atmospheric boundary layer flow through wind turbines and wind farms	Title of the article/chapter the portion is from	Large-eddy simulation of atmospheric boundary layer flow through wind turbines and wind farms
Editor of portion(s)	Porté-Agel, Fernando; Wu, Yu-Ting; Lu, Hao; Conzemius, Robert J.	Author of portion(s)	Porté-Agel, Fernando; Wu, Yu-Ting; Lu, Hao; Conzemius, Robert J.
Volume of serial or monograph	99	Issue, if republishing an article from a serial	4
Page or page range of portion	154-168	Publication date of portion	2011-03-31

Permission for figures 2.9 and 2.10

BA Beqai, Ahmad
To: permissions@wiley.com

Mon 2022-06-13 1:47 PM

Hello,

I am seeking permission to use 2 figures from the journal paper "Effects of inflow turbulence intensity and turbine arrangements on the power generation efficiency of large wind farms".

I have tried using the Marketplace website, but it prompts me to contact the publisher directly.

Name: Ahmad Beqai
Use: Thesis
Institution: University of Saskatchewan
Instructor: Donald Bergstrom

Regards,
Ahmad Beqai

WP Wiley Global Permissions <permissions@wiley.com>
To: Beqai, Ahmad

Wed 2022-06-15 4:52 AM

CAUTION: External to USask. Verify sender and use caution with links and attachments. Forward suspicious emails to phishing@usask.ca

Dear Ahmad,

Thank you for your email.

Permission is granted for you to use the material requested for your thesis/dissertation subject to the usual acknowledgements (author, title of material, title of book/journal, we as publisher) and on the understanding that you will reapply for permission if you wish to distribute or publish your thesis/dissertation commercially.

You should also duplicate the copyright notice that appears in the Wiley publication in your use of the Material. Permission is granted solely for use in conjunction with the thesis, and the material may not be posted online separately.

Any third-party material is expressly excluded from this permission. If any material appears within the article with credit to another source, authorisation from that source must be obtained.

Should you require any further information, please do not hesitate to contact me.

Kind regards

Mary O'Connell
Sales Co-Ordinator, GSP

Chichester, United Kingdom

WILEY